Naval Research Laboratory

Washington, DC 20375-5320

NRL/FR/7121--06-10,123

Ship-Induced Noise Predictions in the Atlantic and the Pacific: A Comparison of Two Noise Models

RICHARD HEITMEYER
STEPHEN C. WALES
LISA A. PFLUG
THOMAS J. HAYWARD

Acoustic Signal Processing Branch
Acoustic Division

IMAN W. SCHURMAN

Applied Physics Laboratory
Johns Hopkins University
Laurel, Maryland

May 30, 2006

REPORT DOCUMENTATION PAGE

Form Approved
OMB No. 0704-0188

1. REPORT DATE *(DD-MM-YYYY)*	**2. REPORT TYPE**	**3. DATES COVERED** *(From - To)*
30-05-2006	Formal	

4. TITLE AND SUBTITLE

Ship-Induced Noise Predictions in the Atlantic and the Pacific: A Comparison of Two Noise Models

5a. CONTRACT NUMBER

5b. GRANT NUMBER

5c. PROGRAM ELEMENT NUMBER
62747N

6. AUTHOR(S)

Richard Heitmeyer, Stephen C. Wales, Lisa A. Pflug, Thomas J. Hayward, and Iman Schurman*

5d. PROJECT NUMBER
UW-747-016

5e. TASK NUMBER

5f. WORK UNIT NUMBER
6053

7. PERFORMING ORGANIZATION NAME(S) AND ADDRESS(ES)

Naval Research Laboratory
Washington, DC 20375-5320

8. PERFORMING ORGANIZATION REPORT NUMBER

NRL/FR/7121--06-10,123

9. SPONSORING / MONITORING AGENCY NAME(S) AND ADDRESS(ES)

Office of Naval Research
875 N. Randolph Street
Arlington, VA 22203-1995

10. SPONSOR / MONITOR'S ACRONYM(S)
ONR

11. SPONSOR / MONITOR'S REPORT NUMBER(S)

12. DISTRIBUTION / AVAILABILITY STATEMENT

Approved for public release; distribution is unlimited.

13. SUPPLEMENTARY NOTES

*Applied Physics Laboratory, Johns Hopkins University, Laurel, MD

14. ABSTRACT

This report describes differences in the ship-induced, bearing-elevation, noise directionality obtained from different noise models and interprets those differences in terms of the propagation and the environmental components of those models. The two noise models, RANDI and APL, both compute the noise as the incoherent sum of the individual ship contributions; they differ in both their propagation models (ANM and FEPE) and in their environmental models. The directionalities are computed for both the Sargasso Sea and the Gulf of Alaska. The Sargasso Sea results differ significantly with the APL directionality, showing lower levels and a much deeper noise notch. In the Gulf of Alaska, the directionalities are much more similar, with both exhibiting deeper noise notches than in the Sargasso Sea. The disparity in the Sargasso Sea noise notch results primarily because, for the ANM model, the set of modes excited by sources near the continental shelf is disjoint from the modes observed by the array. For the Gulf of Alaska, this "mode-set-disjunction" does not occur, and hence, the ANM more realistically estimates the downslope propagating contributions.

15. SUBJECT TERMS
Ambient noise Ambient noise model Shipping noise Acoustic propagation model
Acoustic environmental effects

16. SECURITY CLASSIFICATION OF:			**17. LIMITATION OF ABSTRACT**	**18. NUMBER OF PAGES**	**19a. NAME OF RESPONSIBLE PERSON**
a. REPORT	**b. ABSTRACT**	**c. THIS PAGE**			Richard Heitmeyer
Unclassified	Unclassified	Unclassified	Unlimited	35	**19b. TELEPHONE NUMBER** *(include area code)* 202-404-1850

Standard Form 298 (Rev. 8-98)
Prescribed by ANSI Std. Z39.18

CONTENTS

FIGURES

TABLES

SHIP-INDUCED NOISE PREDICTIONS IN THE ATLANTIC AND THE PACIFIC: A COMPARISON OF TWO NOISE MODELS

1. INTRODUCTION

This report describes the bearing-elevation noise directionality obtained from two different ship-induced noise models and interprets the differences in those directionalities in terms of the propagation and the environmental components of those models. The two noise models are the Research Ambient Noise Directionality (RANDI) model [1,2,] resident at the Naval Research Laboratory (NRL), and an adiabatic-normal-mode (ANM) variant of the Applied Physics Laboratory (APL) noise model, referred to here as ANM-APL, resident at the Johns Hopkins University Applied Physics Laboratory. ANM-APL is based on the environmental gridding approach described in Perkins et al. [3]. Both noise models determine the noise directionality from the contributions of the individual ships in a shipping realization. The shipping realization is determined from the HITS shipping density database [4] under the assumption that the ship positions are distributed as a Poisson process. The contribution of each ship is obtained by constructing the acoustic environment along a great circle track from the ship position to the site location using archival databases. The resulting environment provides the input to an acoustic model that computes the acoustic field from the source along a vertical depth segment at the site position. This field is then beamformed to obtain the vertical-arrival structure of the ship contribution. Finally, the noise directionality is obtained by incoherently summing the contributions of the ships in elemental bearing intervals to produce the bearing-elevation angle distribution of the noise power generated by the ships in the shipping realization.

The two noise models differ in the propagation models that are used to compute the contribution from each ship and in the method for determining the environmental profiles along the great circle tracks. The RANDI noise model uses a finite element parabolic equation (FEPE) propagation model [5,6] with the environmental profiles determined on a fine range grid by directly sampling the environmental databases. The ANM-APL model uses an ANM propagation model, where the modes and eigenvalues are computed using the MODELAB algorithm developed by Levinson et al. [7]. In the noise model, the environmental profiles are determined through an "environmental partitioning" process that yields region-dependent range intervals. This process yields profiles that differ from those obtained through the direct sampling method used in the RANDI model. The environmental components for the two models are described further in Section 3.

The noise directionalities presented here were computed at deep-water sites in two fundamentally different areas — the Sargasso Sea in the Western Atlantic and the Gulf of Alaska in the Northeast Pacific. The results indicate that in the Sargasso Sea, the noise directionalities for the two models differ significantly from one another. The APL directionality shows a deep noise notch in almost all directions; whereas, the RANDI directionality shows almost no noise notch in the large bearing sector that spans the continental shelf and only a modest noise notch in most other directions. The noise directionalities for the Gulf of Alaska differ significantly from those for the Sargasso Sea, exhibiting deeper noise notches and slightly wider peaks. However, the Gulf of Alaska directionalities for the two noise models are much more similar to one another than the Sargasso Sea directionalities.

Manuscript approved January 20, 2006.

The noise directionalities were computed using the same ship locations and source levels for each model. Thus, the difference in the noise directionalities between the two models is due only to the differences in their propagation and environmental components. To interpret the impact of these differences, we present comparisons of the acoustic field obtained using the propagation and the environmental component of each noise model for a distribution of sources along tracks at selected bearings. These *propagation/environment* comparisons provide a quantitative measure of the effect of the differences in the two components of the two noise models. To isolate the effects of the differences in these components, we also present *environment-only* comparisons, obtained using the same propagation model with different environments, and *propagation-only* comparisons, obtained using the different propagation models with the same environment.

To aid in the interpretation of the different comparisons, we also compare the source-mode functions computed directly from the adiabatic-normal-mode model and from an orthogonal decomposition of the FEPE generated fields. The ANM source-mode functions admit a decomposition of the band of modes containing significant energy into waterborne modes, totally reflected modes and sediment-refracted modes. The dependence of these decompositions on the attributes of the acoustic environment is used to relate the differences in the acoustic fields to the range-dependent properties of the acoustic environments. The FEPE source-mode functions are used to interpret the differences in the acoustic field due to the different propagation models.

The report is organized as follows. In Section 2, we present a comparison of the noise directionalities computed from the two noise models for the two areas. Section 3 presents an overview of the methodology used in the acoustic analysis of the differences in the noise directionalities. In Sections 4 and 5, we present the acoustic analysis for the Sargasso Sea and the Gulf of Alaska, respectively. The results are summarized in Section 6.

2. NOISE DIRECTIONALITY COMPARISON

The noise directionalities for the two areas were computed from ship location realizations obtained from the shipping distributions shown in Fig. 1. The specific sites within each area are indicated by the origin of the range bearing grid. For both areas, the maximum range was limited to 3000 km, which corresponds to slightly more than three of the 500 nmi range contours in the figure.

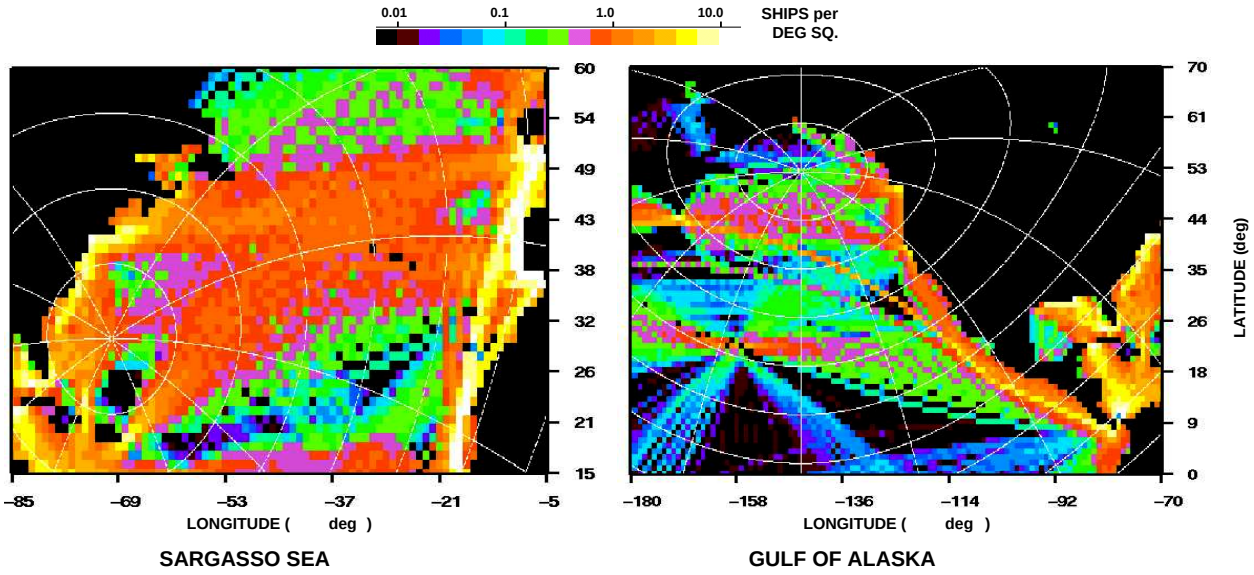

Fig. 1 — Commercial shipping distribution for two areas obtained from the HITS database: (left) the Sargasso Sea site; and (right) the Gulf of Alaska site

The bearing-elevation directionalities for each area were computed at 60 Hz by beamforming over a 204 m depth interval centered at 150 m and accumulating the results in 3° bearing intervals.

2.1 Sargasso Sea Directionalities

The bearing-elevation noise directionalities for the Sargasso Sea Site are shown in Fig. 2. A detailed comparison of the plots indicates that the levels in the elemental bearing intervals in the two directionalities are not the same, even though the directionalities are determined from the same ship locations and source levels. This is not surprising since the received energy in the individual shipping contributions is determined from the different propagation models and environmental components of the two noise models. On the other hand, there are similarities in the two noise directionalities. In particular, both noise directionalities show low noise to the southeast and comparatively high noise in the remaining directions. This is consistent with the light shipping towards the eastern Caribbean, the heavy shipping along the eastern coast of the United States to the west and north, and the moderate shipping in the open ocean directions to the northeast and east. Beyond these similarities, however, there are significant differences in the two noise directionalities. The most striking difference occurs in the southerly directions, where the APL noise directionality shows a deeper noise notch than the RANDI directionality. Further, the APL directionality exhibits a noise notch in the northeast direction, whereas the RANDI directionality does not.

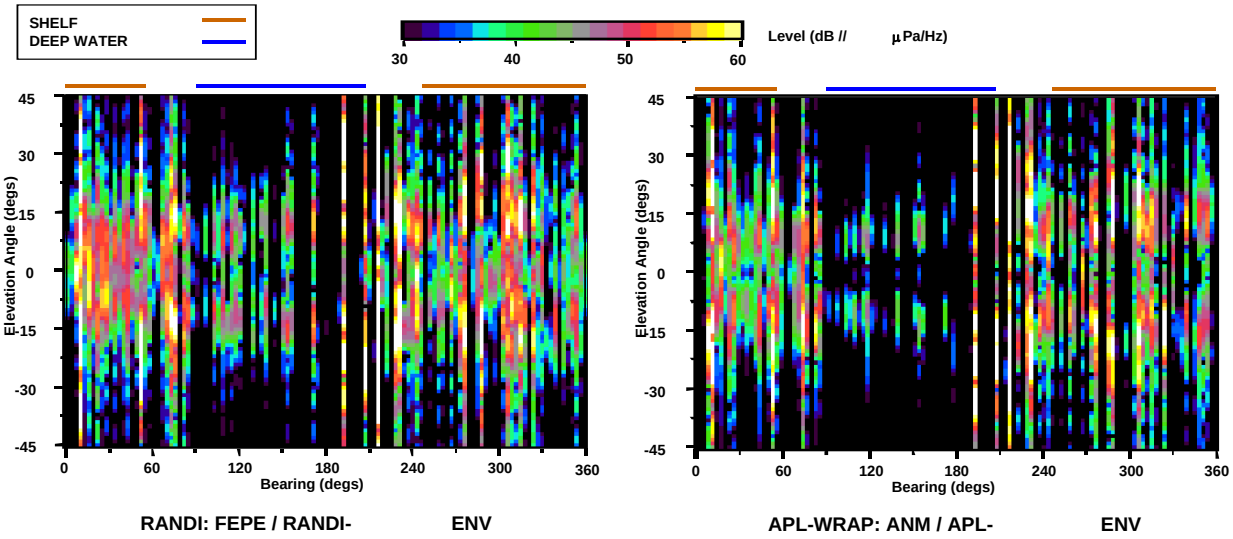

Fig. 2 — Noise directionality comparison for the Sargasso Sea: (left) RANDI and (right) APL. Horizontal bars above each plot indicate the bearing sectors designated as deep-water (blue) and shelf (brown).

To quantify these differences, we have computed bearing averages of the directionalities from the two models for different sectors and plotted the results in Fig. 3. The elevation-angle directionalities from the RANDI model are shown in blue; those from the APL model are shown in red. The directionalities in the center plot were computed for a "deep-water" bearing sector (90° to 210°); those in the right plot for a "shelf" bearing sector (250° to 60°); and those in the left plot for the full 360° bearing sector. Each of the elevation-angle directionalities is obtained as a decibel average over the bearing sector using eight realizations of the shipping distributions.

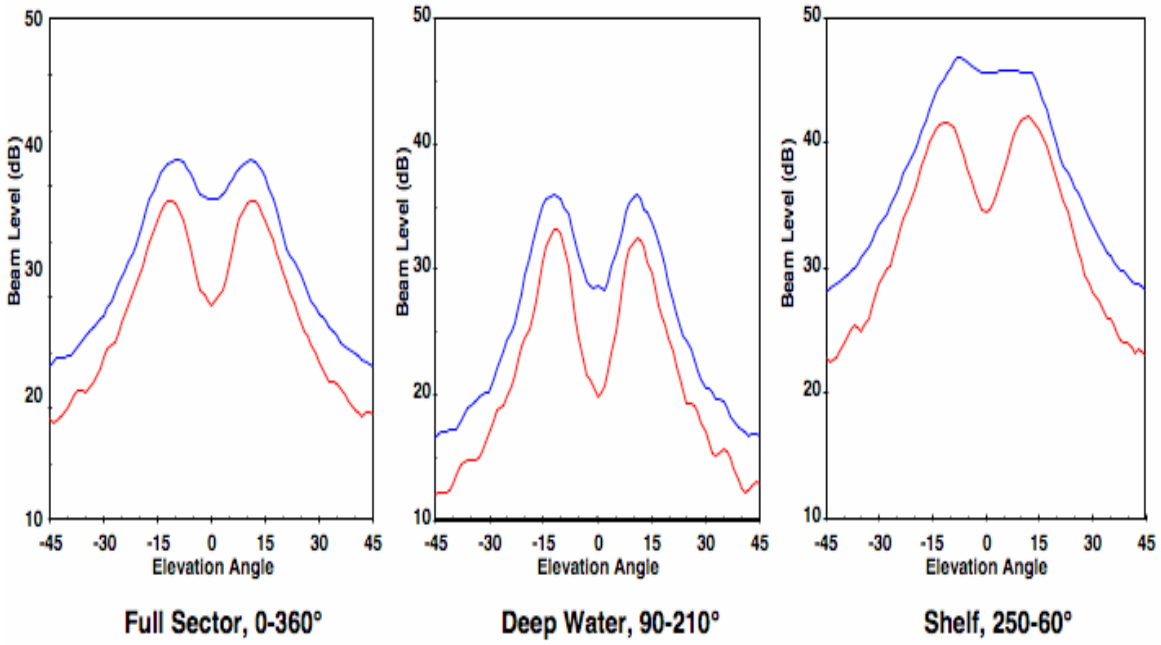

Fig. 3 — Noise directionality bearing averages for the Sargasso Sea from the two noise models: (blue) RANDI, and (red) APL

As seen in the figure, the deep-water directionalities for both models show a bimodal structure with the two peaks at essentially the same arrival angles, about ± 13°. The depth of the noise notch for the RANDI model is significantly less than for the APL model: about 6 dB compared to about 12 dB. Elsewhere, the overall levels for the RANDI model are about 2 dB larger than for the APL model. In the shelf directions, the differences are even more striking. As in the deep-water sector, the APL directionality shows a noise notch with peaks at about ± 13°, but the peaks are broader and the depth of the notch is less (about 6 dB). The RANDI directionality does not show a noise notch at all and is everywhere larger than the APL directionality. Finally, the full-bearing sector directionalities both show a bimodal structure with peak angles at ± 13°. The RANDI directionality is larger than the APL directionality and the depth of the RANDI noise notch (about 3 dB) is significantly less than the depth of the APL noise notch (about 9 dB). This is expected since the full-bearing sector directionalities are roughly equal to the average of the specific sector directionalities.

To interpret these differences we have computed the level-angle distributions of the noise source contributions from each model. The results are shown in Fig. 4. These plots are obtained by computing the vertical resolution of the contribution from each ship in a shipping realization. The dots in each distribution are located at the locations of the ships in the shipping realization; the size of each dot indicates the peak value of the vertical resolution in the ship contribution and the color of the dot indicates the elevation angle at which that peak occurs. The correspondence between the level and angle and the size and the color is shown in the legend. The array location is indicated by the star.

In Fig. 4, it is seen that in the deep-water, 90° to 210° sector, the majority of the ship contributions for both noise models have elevation angles between 8° and 16°. This is expected since an abyssal plain covers most of this region. There are, however, a number of gold dots in the RANDI distribution that are green in the APL distribution, indicating that at least some of the contributions for the RANDI model occur at smaller elevation angles than for the APL model. As discussed later, it is believed that this is due, at least in part, to the different environmental representations of isolated sea mounts as discussed later in the report. Also, note that the RANDI distribution has a few dots that are larger than those in the APL distribution. This is believed to be largely due to differences in the geoacoustic properties of the sediment between the two noise models.

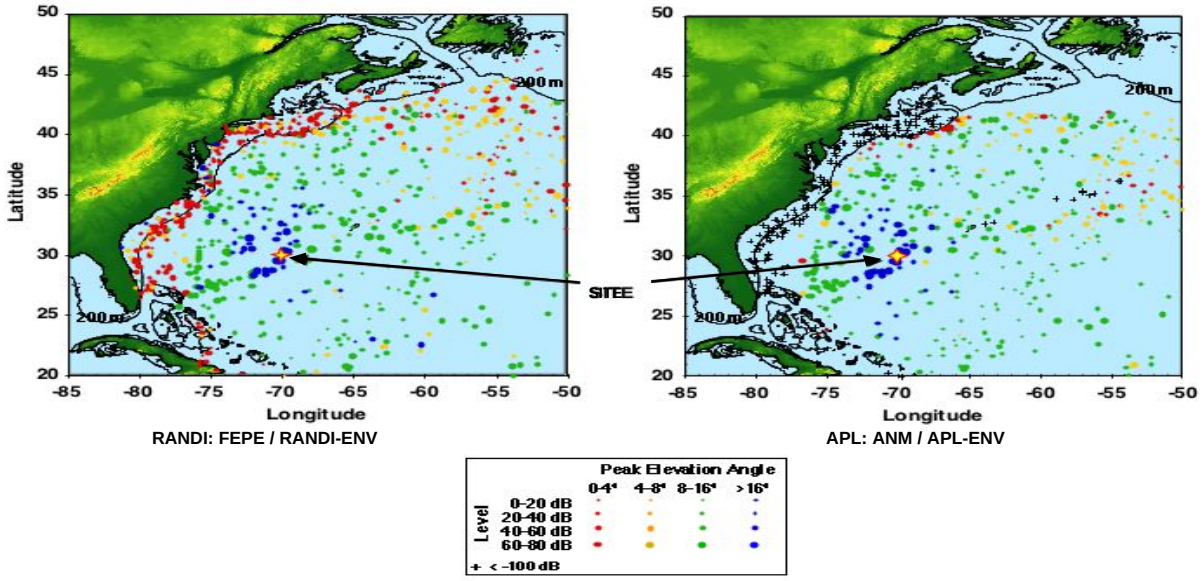

Fig. 4 — Ship noise level-angle distributions for the Sargasso Sea site from the two noise models: (left) RANDI; (right) APL

The major difference in the two level-angle distributions is in the contributions from ships that lie within the 200-m contour of the United States. For the RANDI distribution, there are a significant number of these contributions, most of which have maximum elevation angles that are less than 4°. The small angles are a consequence of the collapse of the bimodal arrival structure in the propagation down the continental slope. On the other hand, for the APL distribution, most ships within the 200-m contour have received levels of less than -100 dB at the array, as denoted by '+' symbols in the figure. Only a small number of ships near the 200-m contour directly north of the array contribute to low angle levels in the directionality. It is this disparity in the contributions from the shelf and the near shelf-break that is the major cause of the difference in the elevation-angle directionalities for the shelf sector, and hence, for the full-bearing sector.

2.2 Gulf of Alaska Directionalities

The bearing-elevation directionalities for the Gulf of Alaska are shown in Fig. 5. A comparison of these directionalities with those for the Sargasso Sea indicates that the noise notch is much more pronounced in the Gulf of Alaska and it extends over almost the full-bearing sector. Furthermore, the directionalities for the two noise models are much more similar to one another than those for the Sargasso Sea.

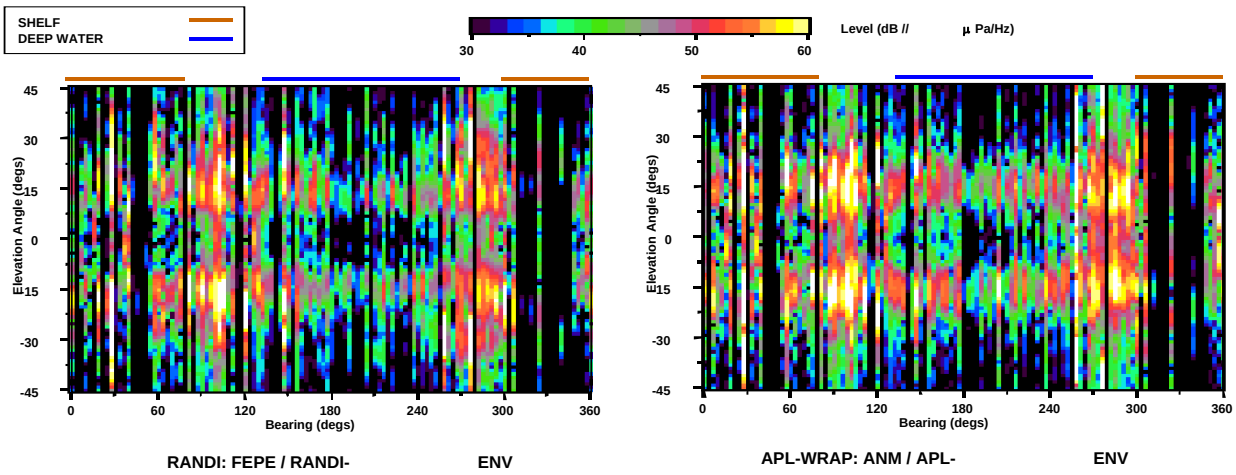

Fig. 5 — Noise directionality comparison for the Gulf of Alaska: (left) RANDI; (right) APL. Horizontal bars above each plot indicate the bearing sectors designated as deep-water (blue) and shelf (brown)

Plots of the elevation-angle directionality obtained by averaging the bearing-elevation directionalities over different bearing sectors are shown in Fig. 6. As for the Sargasso Sea (Fig. 3), the directionalities shown here are computed for a deep-water sector (130° to 275°), a shelf sector (300° to 75°) and the full 360° bearing sector. As seen in the figure, the directionalities for both models show the bimodal structure for all three sectors. In contrast to the Sargasso Sea, the levels for the APL model are larger than those for the RANDI model, except for the larger elevation angles, where the levels of the two directionalities are nearly equal. For the deep-water and the full-bearing sectors, the depth of the noise notch for the two models is comparable, about 11 dB for the full-bearing sector and about 14 dB for the deep-water sector. In the shelf sector, the noise notch depth of the APL directionality is about 8 dB, which is a few dB less than the noise notch depth of the RANDI directionality. Note that the peaks in the elevation-angle directionality occur at about ± 15° for the APL model, and ± 14° for the RANDI model, whereas in the Sargasso Sea, the peaks for both models occur at about ± 13°.

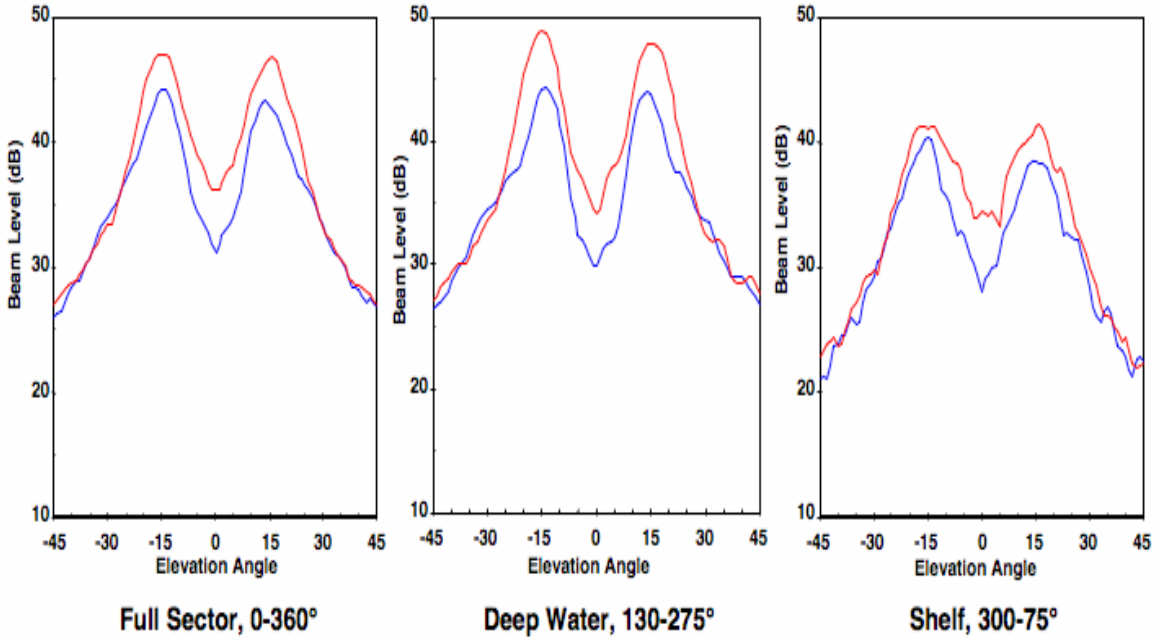

Fig. 6 — Noise directionality bearing averages for the Gulf of Alaska from the two noise models: (blue) RANDI and (red) APL

The level-angle distributions for the Gulf of Alaska are shown in Fig. 7. As expected from the similarity in the bearing-elevation directionalities, the level-angle distributions for the two models are much more similar to one another than those for the Sargasso Sea. The well-defined noise notch in each directionality is a consequence of the preponderance of large angle contributions (green and blue dots) in each distribution. The lack of small angle contributions in each distribution is a consequence of the deficiency in contributions from ships on the shelf which is, itself, a consequence of the much smaller breadth of the continental shelf in the Northeast Pacific. Note that, unlike the Sargasso Sea, the near shelf-break, small angle contributions in the RANDI distribution also appear in the APL distribution. In the Sargasso Sea, all the near shelf-break contributions in the APL distribution had received levels of less than -100 dB.

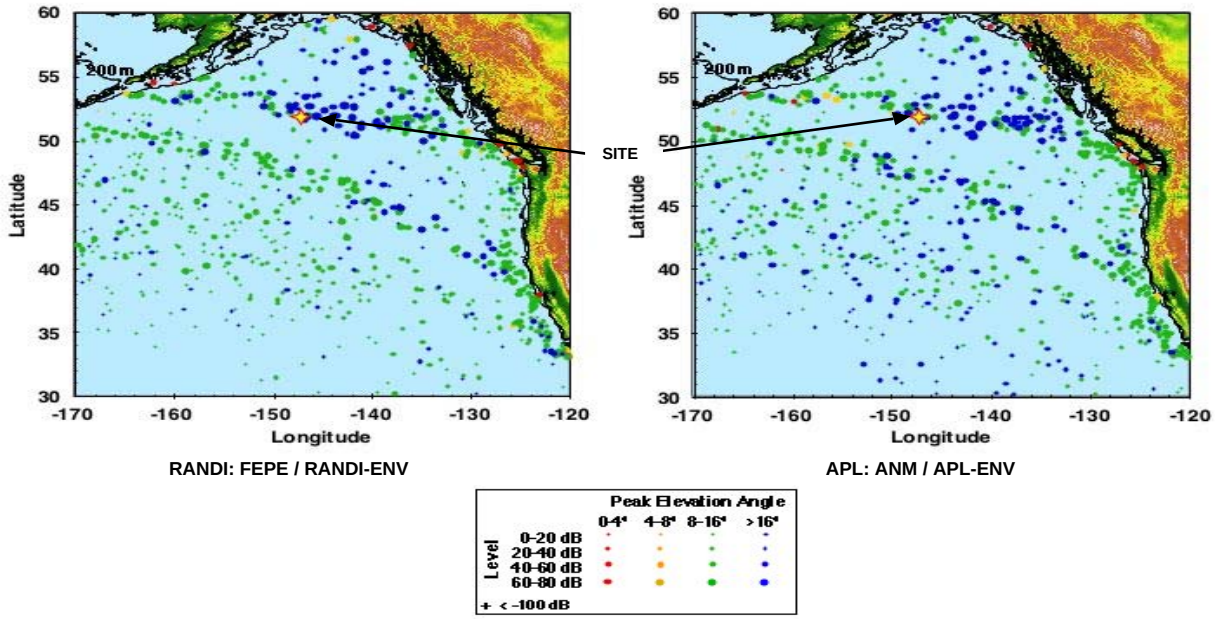

Fig. 7 — Ship noise level-angle distributions for the Gulf of Alaska site from the two noise models: (left) RANDI and (right) APL

3. ANALYSIS METHODOLOGY

The results of the preceding section indicate that there are significant differences in the noise directionalities computed by the two noise models for the Sargasso Sea, but comparatively minor differences in the directionalities for the Gulf of Alaska. Further, these differences are due only to the propagation and environment components of the two noise models and not to the distributions of the source levels and the positions of the ships that generated the noise. In this section, we describe the methodology used to interpret these differences in terms of the propagation and environmental components of the two noise models. In the following sections, we present the analyses leading to these interpretations for the Sargasso Sea and the Gulf of Alaska, respectively.

The acoustic comparisons are obtained using the propagation and the environmental component of each noise model to compute the received acoustic field as a function of source range for selected bearings in each area. To interpret the results, we have also conducted environment-only and propagation-only comparisons. The environment-only comparisons are obtained using a second adiabatic-normal-mode model, the KRAKEN-C version of KRAKEN [7], to compute the acoustic field for the environments generated by the environmental components of the two noise models. The propagation-only comparisons are obtained by computing the fields with the FEPE model and with the KRAKEN model using the environment component of the RANDI noise model. The three comparisons are shown schematically in Fig. 8 along with the computational components used in the comparisons.

In addition to the three computational components shown in Fig. 8, there is a fourth component consisting of the APL environment and the KRAKEN propagation model. The comparison of the results obtained from this component with those obtained from the “APL” component, provides confirmation that the two ANM models give comparable results for the same environment, and hence, that the ANM-KRAKEN model is suitable for the environment-only and the propagation-only comparisons.

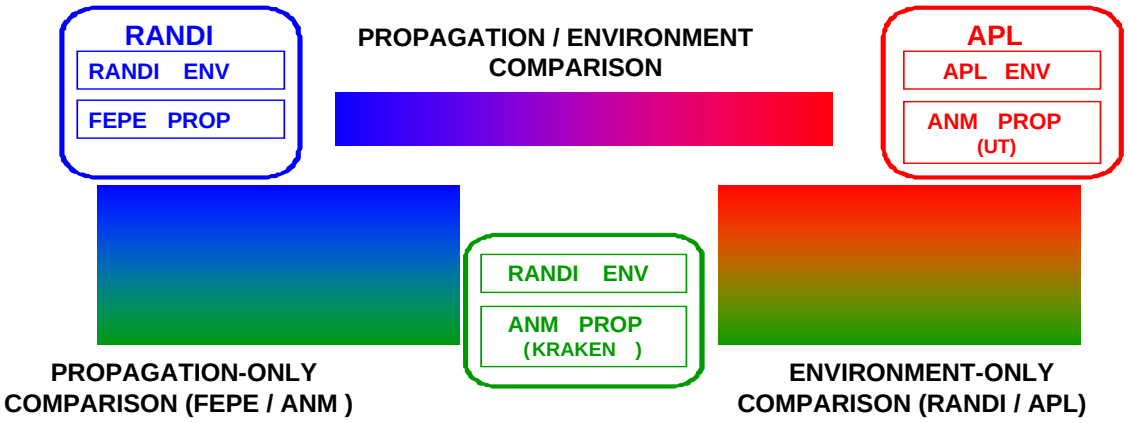

Fig. 8 — Model and environment comparisons

The environmental components of both noise models generate a sequence of environmental profiles on a range grid along the great circle track from the source to the site. Each of the environmental profiles describes the depth distribution of the sound speed, the density, and the attenuation in the water column and in a fluid sediment layer located beneath the water column. The sound speed and the depth of the water column for both models are obtained from archival databases as are the geoacoustic parameters used to determine the sound speed, density, attenuation, and thickness of the sediment layer.

The major elements of the environmental components for the two noise models are summarized in Table 1. The database sampling algorithms for the two noise models are fundamentally different. In the RANDI model, the environmental profiles are determined by directly sampling the environmental databases at range intervals commensurate with the latitude-longitude resolution in the bathymetry database. For the latitudes of interest in this analysis, this sampling results in range intervals of about 7 km. In the APL model, the environmental profiles are determined through an environmental partitioning process that determines regions of constant environment on a spatial scale that is considered appropriate for an adiabatic-normal-mode propagation model [8,9,10]. These partitions, which are strongly dependent on the spatial variability in the bathymetry, can result in very fine range grids in continental shelf and slope regions and much coarser resolution in the deep-water abyssal plains (e.g., range intervals from 5 km to over a 100 km). For large open ocean regions, the environmental partitioning approach produces fewer profiles than the direct sampling approach. This is particularly advantageous for noise models that use an ANM propagation model since the mode quantities for each of the subregions can be precomputed.

As seen in the table, the databases for the bathymetry, DBDB5 [11], are the same for the two environmental components. The databases for the sound speed in the water column for the RANDI model is a “provinced” version of the GDEM [12] database used in the APL model. The geoacoustic database for the RANDI model, Consolidated BLUG, was derived from an early version of the LFBL database [13] used in the APL model. A comprehensive analysis of these differences has not been conducted.

Table 1 — The RANDI and APL Environmental Components

	RANDI	**APL**
Sampling Method	Resolution-based	Environmental Partitioning
Databases		
Sound Speed	GDEM (Provincial)	GDEM
Bathymetry	DBDB5	DBDB5
Geoacoustic	Consolidated BLUG	LFBL
Bottom Extension	Absorbing fluid half space	1000 m fluid + Rigid

Finally, the two environmental components differ in the method of extending the environment below the sediment layer. In the RANDI model, the bottom extension consists of a fluid half-space. The sound speed in the half-space is obtained from the sediment layer sound speed by a continuity assumption and the density is obtained from a reflection coefficient and the continuous sound speed assumption. The attenuation in the half space in taken to be large enough so that no energy can propagate over an appreciable distance (10 dB/wavelength). In the APL model, the bottom extension is obtained by appending a 1000-m "sediment layer" followed by a rigid half-space. The geoacoustic parameters in the 1000-m extension are obtained as linear extrapolations of the sediment parameter profiles.

In the remainder of this report, we present an analysis of the propagation components of the two noise models for three source tracks in both the Sargasso Sea and the Gulf of Alaska: a "range-independent" track, a deep-water track, and a continental-shelf track. The range-independent track provides a characterization of the propagation for the acoustic environment at the site, which is common to all tracks. Further, since the environment does not vary with range, the adiabatic-normal-mode approximation is exact up to the continuous mode approximation, and the FEPE model is exact up to the parabolic equation approximation, both of which are reasonable for a range-independent environment except at very small ranges. Consequently, the comparison of the results for the range-independent tracks provides an important baseline for the interpretation of the results on the deep-water and the continental-slope tracks.

The deep-water tracks lie in the "deep-water" bearing sectors for the noise directionalities. As seen in Figs. 3 and 6, the elevation angle structures in these sectors have the bimodal form typical of deep-water propagation. This form is expected for deep-water tracks, where there are no strong bathymetric or sound speed variations. Furthermore, due to the comparatively weak environmental variations along these tracks, the differences in the propagation for the two noise models are primarily due to differences in the environmental components, rather than the different propagation models.

The continental-shelf tracks lie in the "continental shelf" bearing sector for the noise directionalities. For the Sargasso Sea, the vertical noise directionality in the shelf sector shows a unimodal structure for the RANDI model and a bimodal structure for the APL model. For the Gulf of Alaska, the noise directionality in the shelf sector shows a bimodal structure for both noise models. The unimodal form is expected for sources located near the shelf-break since the energy in the high order modes is converted to low order mode energy. Since the adiabatic-normal-mode model cannot redistribute energy across modes, the differences in the propagation can be due to differences in both components of the noise model.

We conclude this section with an overview of the definitions and properties of the source-mode functions used to interpret the propagation comparisons. These functions are particularly useful for the deep-water, shallow-source acoustic environments relevant to the ship-induced noise problem of interest here. The source-mode function determined under the adiabatic-normal-mode approximation admits a mode-band decomposition that is useful for isolating the dependence of the propagation on the specific attributes of the environment and for expressing a necessary condition on the suitability of the adiabatic approximation for downslope propagation. The comparison of these functions with those determined from

the FEPE acoustic model is useful for identifying those environmental conditions for which the ANM propagation is not acceptable.

To begin, recall that for a vertical array at a fixed latitude-longitude location, the acoustic field can be represented as a function of the depth z at that location and the source range r_s and depth z_s in an expansion of the form

$$p(z; z_s, r_s) = \sum_m \varphi_m^a(z)\gamma_m(z_s, r_s)/r_s\,, \tag{1}$$

where $\varphi_m^a(z)$ are orthonormal functions that describe the normal modes in the vicinity of the array and $\gamma_m(z_s, r_s)$ are the source mode amplitudes at r_s and z_s. Under the adiabatic assumption, the source mode amplitudes are given by

$$\gamma_m(z_s, r_s) = \sqrt{\frac{2\pi}{k_m(r_s)}}\varphi_m(z_s, r_s)\exp\left\{i\int_0^{r_s} k_m(r')\,dr'\right\}, \tag{2}$$

where $\varphi_m(z_s, r)$ is the m^{th} normal mode at range r and $k_m(r)$ is the corresponding complex wavenumber. For later use, it will be convenient to write the magnitude-squared of the source mode amplitude in the form

$$\left|\gamma(m, r_s)\right|^2 = \left|\varphi_m(z_s, r_s)\right|^2 \frac{\beta(m, r_s)}{r_s}, \tag{3}$$

where

$$\beta(m, r_s) = \frac{2\pi}{k_m(r_s)}\left|\exp\left\{i\int_0^{r_s} k_m(r')\,dr'\right\}\right|^2 = \frac{2\pi}{k_m(r_s)}\exp\left\{-2\int_0^{r_s} \alpha_m(r')\,dr'\right\} \tag{4}$$

is the reciprocal of the mode attenuation loss for the m^{th} mode at range r_s and $\alpha_m(r) = \text{Im}\left[k_m(r)\right]$ is the mode attenuation at range r. We refer to $\left|\gamma(m, r_s)\right|^2$ as the source-mode function. In the more general case, the source mode amplitudes can be computed from the acoustic field by an orthogonal decomposition with respect to the inner product determined by the local normal modes and a weighting function equal to the reciprocal of the density.

To illustrate the properties of the source-mode function, we have plotted an example computed using the RANDI propagation/environment model for the deep-water track in the Sargasso Sea in Fig. 9. The source-mode function is shown at the bottom of the figure. At the top of the figure, we have plotted the energy in the normal modes $\left|\varphi_m(z, r_s)\right|^2$ as a function of receiver depth for a specific source range $r_s = 1000$ km. For $r_s = 0$, this function is simply the array modes of Eq. (1), i.e., $\varphi_m^a(z) = \varphi_m(z, r_s = 0)$. As seen in the top plot, the normal modes have a depth-mode envelope, $M(z)$, which contains essentially all of the energy. This envelope can be approximated from the condition that, for a fixed mode number, the depth extremes of a mode correspond to the turning depths of the rays associated with that mode (see, for example, Section 6.7 of Brekhovskikh and Lysanov [14]). Thus, for each depth z, the mode envelope is the mode $M(z)$ that satisfies

$$\text{Re}\left[k_{M(z)}\right] = 2\pi f / c(z). \tag{5}$$

According to Eq. (5), the mode envelope is completely determined by $c(z)$, the sound speed in the water-column and the compressional speed in the sediment layer. Note that since $\mathrm{Re}[k_m]$ is a decreasing function of m, $M(z)$ is an increasing function of the sound speed evaluated at the depth z.

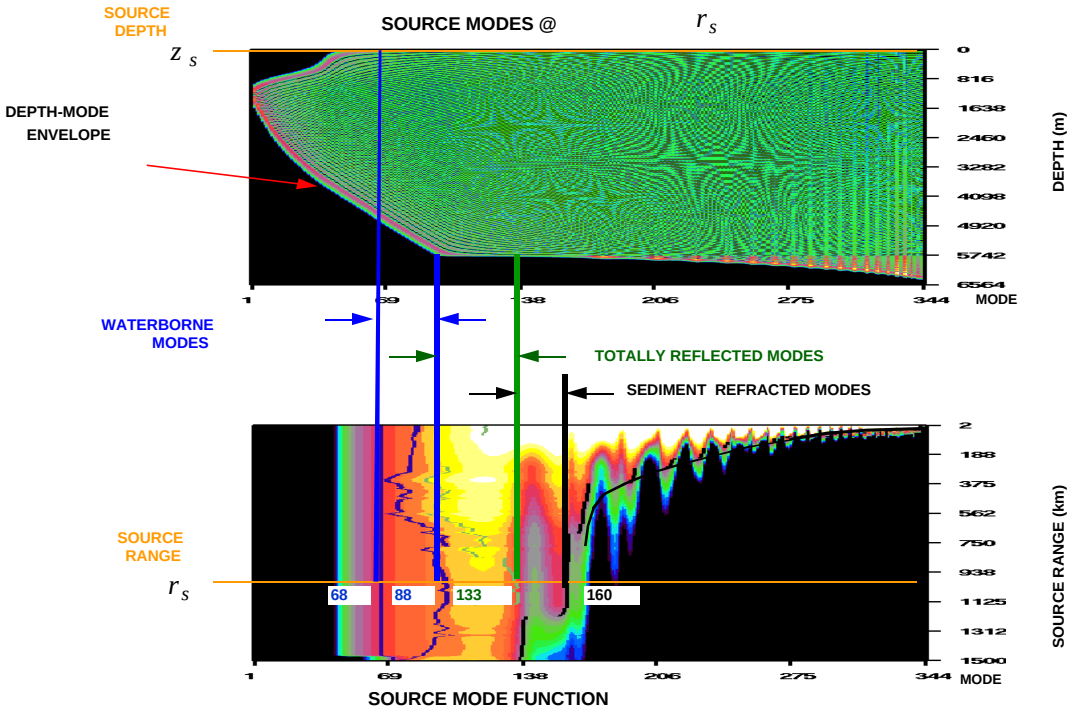

Fig. 9 — Source-mode function $\left|\gamma\left(m, r_s\right)\right|^2$ (bottom) and source-mode amplitudes at a fixed range, $\left|\varphi_m\left(z_s, r_s = 1000\right)\right|^2$ (top), computed using the RANDI propagation/environment model for the deep-water track in the Sargasso Sea.

The depth-mode envelope determines a partition of the energy in the source-mode function $\left|\gamma\left(m, r_s\right)\right|^2$ into waterborne modes and sediment-interacting modes. To see this, note that at the depth of the water column z_W the envelope of the source modes has an inflection point that occurs at a mode number $M_{w,u} = M\left(z_w^-\right)$. This mode corresponds to rays that just graze the sediment. Thus, mode numbers smaller than $M_{w,u}$ correspond to waterborne modes, and mode numbers larger than $M_{w,u}$ correspond to sediment-interacting modes. The smallest mode that contributes significant energy is determined by evaluating $M(z)$ at the source depth, i.e., $M_{w,l} = M\left(z_s\right)$. Thus, the waterborne modes are those modes that lie between $M_{w,l} = M(z_s)$ and $M_{w,u} = M\left(z_w^-\right)$. For the source range $r_s = 1000$ in Fig. 9, $M_{w,u}$ is about 68 and $M_{w,u}$ is about 88.

The environmental dependence of the waterborne mode limits is obtained by recalling that $M(z)$ is an increasing function of the sound speed. Thus, the lower limit of the waterborne modes, $M_{w,l}$, is an increasing function of the sound speed at the source depth. For the upper limit, recall that in the deep-water ocean basins, the sound speed at the sediment interface is essentially a function only of the water depth and is an increasing function of that depth. Thus, in deep water, the upper limit of the waterborne

modes $M_{w,u}$ is an increasing function of the water depth. The dependence of these limits on the source range is shown by the two blue curves in the source-modes function in the lower plot of Fig. 9. For this case, the sound speed in the water column is independent of source range out to the last 50 km. Thus, the lower limit of the waterborne modes (the leftmost blue curve) is independent of source range over this interval, and the range dependence of the upper limit (the rightmost blue curve) is governed by the variation in the bathymetry.

The sediment-interacting modes are those with mode numbers larger than the waterborne upper limit, $M_{w,u}$. There are two possibilities, depending on whether the jump in the sound speed at the water-sediment interface is positive or negative. For a positive jump, which is the case illustrated in the top plot of Fig. 6, the envelope of the source modes is essentially independent of depth for mode numbers between $M_{w,u} = M\left(z_w^-\right)$ and $M_{tr,u} = M\left(z_w^+\right)$. These modes describe the energy that is totally reflected from the water-sediment interface, i.e., the energy that is incident on the interface at grazing angles less than the critical angle. The upper limit of the total-reflection band, $M_{tr,u}$, depends on the environment through the value of the compressional speed at the top of the sediment layer, $c\left(z_w^+\right)$, which in turn depends on the sound speed at the bottom of the water column $c\left(z_w^-\right)$ and the sound-speed ratio $r_c = c\left(z_w^+\right) / c\left(z_w^-\right)$. It follows that $M_{tr,u}$ is an increasing function of both z_w and r_c. When the sound-speed ratio is less than unity, there is no critical angle, and hence, there is no total-reflection band. The range dependence of the upper limit of the total-reflection band in Fig. 9 is shown as the green curve; the value at $r_s = 1000$ km is 133.

The remaining band of interest consists of those modes that describe the energy that penetrates into the sediment and is then refracted back to the interface. We refer to this band as the sediment-refraction band. The lower limit of this band, $M_{sr,l}$, is the upper limit of either the waterborne band or the total-reflection band, depending on whether the sound-speed ratio is less than or greater than unity. The upper limit, $M_{sr,u}$, is determined by the fall-off rate of the source-mode function with range. For the shallow source depths of ships, $\left|\varphi_m\left(z_s, r_s\right)\right|^2$ is an increasing function of m for all mode numbers that carry energy to significant ranges. Thus, the upper limit is determined by the fall-off rate of the mode attenuation loss $\beta\left(m, r_s\right)^{-1}$. This function depends on the integral of the mode attenuation, $\alpha_m(r)$, over the interval $[0, r_s]$ which is dependent on the geoacoustic parameters over the interval. In addition, $\alpha_m(r)$ can depend on both the bathymetry and the sound-speed ratio over the range interval. This occurs since $M_{sr,l}$ depends on these components and a change in $M_{sr,l}$ that shifts a mode *m* from a sediment-refraction mode to either a total-reflection or a waterborne mode over a portion of $[0, r_s]$, causes $\alpha_m(r)$ to drop from a significant value to essentially zero for the low frequencies of interest here. Similarly, a change in $M_{sr,l}$ that shifts a mode into the sediment-refraction band results in a large increase in $\alpha_m(r)$. In either case, there will be a significant change in $\beta\left(m, r_s\right)^{-1}$ whenever a change in either the bathymetry or the sound-speed ratio results in shift in a mode from one band to the other. Thus, $M_{sr,u}\left(r_s\right)$ depends on the history of the total environment (sound-speed ratio, bathymetry, and geoacoustic parameters) up to range r_s. This differs from the limits of the waterborne and the total-reflection bands, which do not depend on the history of the environment up to range r_s, but only on the sound speed at range r_s. The upper limit of the sediment refraction band in Fig. 9 is shown as the black curve. Table 2 contains a summary of the relationships described above.

Table 2 — Summary of Mode-Band Decomposition Relationships and Environmental Dependencies

Band	**Dependencies**
Waterborne	$\beta(m, r_s)$ decreases slowly with r_s; $\lvert\varphi_m(z_s, r_s)\rvert^2$ decreasing function of z_w
$M_{w,l} = M(z_s)$	increasing function of $c(z_s)$
$M_{w,u} = M(z_w^-)$	increasing function of z_w
Total-Reflection ($r_c > 1$)	$\beta(m, r_s)$ decreases slowly with r_s; $\lvert\varphi_m(z_s, r_s)\rvert^2$ decreasing function of z_w
$M_{tr,l} = M_{w,u}$	
$M_{tr,u} = M(z_w^+)$	increasing function of z_w, r_c
Sediment-Refraction	$\beta(m, r_s)$ decreases rapidly with r_s
$M_{sr,l} = M_{w,u}, M_{tr,u}$	
$M_{sr,u}$	determined by $\beta(m, r_s)$

For acoustic fields computed from more exact models, e.g., FEPE, the source-mode amplitudes can be computed from the acoustic field by an orthogonal decomposition with respect to the inner product determined by the local normal modes and a weighting function equal to the reciprocal of the density. Examples are presented in the following sections.

4. SARGASSO SEA PROPAGATION COMPARISON

This section presents an analysis of the propagation components of the two noise models for the Sargasso Sea. As described in the preceding section, the analysis is obtained through three comparisons (a propagation/environment comparison, a propagation-only comparison, and an environment-only comparison) conducted on three tracks (a range-independent track, a deep-water track, and a continental-shelf track).

4.1 Range-Independent Track

The environments for the 500 km range-independent track are obtained from the environmental components of the two noise models for a site located about 720 nmi east of Jacksonville, Florida, in the Sargasso Sea. The depth profiles describing the two environments are shown in Fig. 10; the RANDI environment is described by the blue curves and the APL environment by the red curves. Parameters of the two environments are listed in Table A1 in Appendix A.

As seen in the figure, the water-column sound speeds (left) are identical down to a depth of 1200 m, after which the APL sound speed is 1.6 m/s to 1.7 m/s greater than the RANDI sound speed. Since the slopes of the two sound speed profiles are essentially the same below 1200 m, this difference is expected to have negligible effect on the propagation. The water depth for the APL model (5334 m) exceeds the water depth for the RANDI model (5309 m) by 25 m. This difference is also not expected to have a major effect on the propagation.

The sediment compressional speed profiles for the two models are shown at the top right. As seen in the figure, these profiles are very similar to one another over the approximately 1000-m sediment depth interval[1], except for the slightly larger values in the RANDI profile. This offset is largely due to the larger value of the sound-speed ratio for the RANDI model (1.020 vs 0.996). This difference results in larger values for the sound speed in the sediment layer at the sediment/water-column interface for the RANDI model, even though the sound speed in the water column at the interface is less. The larger compressional speed values, in themselves, do not have a major impact on the propagation. However, the RANDI sound-speed ratio of greater than unity (hard bottom) results in a critical grazing angle of about 11°. Consequently, all of the energy that is incident on the sediment for grazing angles less than 11° is reflected without loss. The APL sound-speed ratio of less than unity (soft bottom) does not result in a critical angle so that for all angles greater than zero, some of the energy is transmitted into the sediment layer. The reflection and transmission coefficients for the two environments are illustrated in Fig. A1 of Appendix A. These plots indicate that for the larger grazing angles, fully 60 percent of the energy is reflected for the RANDI environment and only about 18 percent for the APL environment. However, much of the energy that is transmitted into the sediment layer is refracted back to the interface and is then transmitted back into the water column. The difference in the reflection coefficients is primarily due to the larger density in the RANDI environment.

Finally, the attenuation profiles are shown in the lower right of Fig. 10. It is seen that the RANDI attenuation is larger than the APL attenuation at all depths except near the top of the sediment layer, where it is comparable. For long range propagation, however, only the attenuation near the top of the layer is important.

With the environmental characterization at hand, we turn to the acoustic propagation comparisons. In Fig. 11 we have plotted the acoustic field and the vertical-arrival structure as a function of source range obtained with the RANDI model (left) and with the APL model (right). The vertical-arrival structures (bottom plots) were computed from the complex field by beamforming over a uniformly shaded vertical aperture spanning the interval from 48 m to 252 m in 6 m increments. As such, the resolution used to compute the arrival structure is the same as that used to compute the noise directionalities of Section 2. We note that all of the propagation plots presented in this report are normalized by source range. With this normalization, the plots show the variation in the level with respect to cylindrical spreading. Further, unless otherwise noted, all of the propagation plots are obtained as a function of source range for a fixed receiver. This differs from the more usual case, where the field is plotted as a function of receiver range for a fixed source. For the range-independent track results shown here, the source range and the receiver range variables are interchangeable.

[1] Part of the difference in the shapes of the two compressional speed profiles is due to the fact that the RANDI profile is obtained by sampling the compressional speed in the RANDI geoacoustic database at only five depth points, whereas the APL profiles are created from 21 depth sample points.

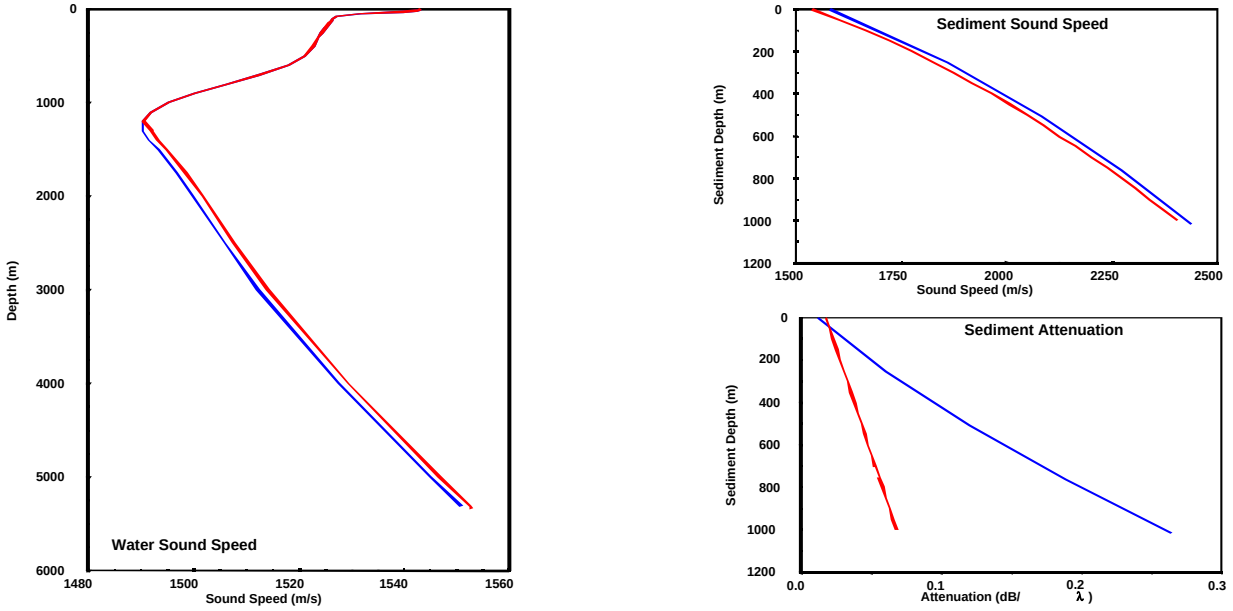

Fig. 10 — Environment profile comparisons at the Sargasso Sea site for the APL environment (red) and the RANDI environment (blue): water-column sound speed profile (left); sediment compressional speed profile (top right); sediment attenuation profile (bottom right)

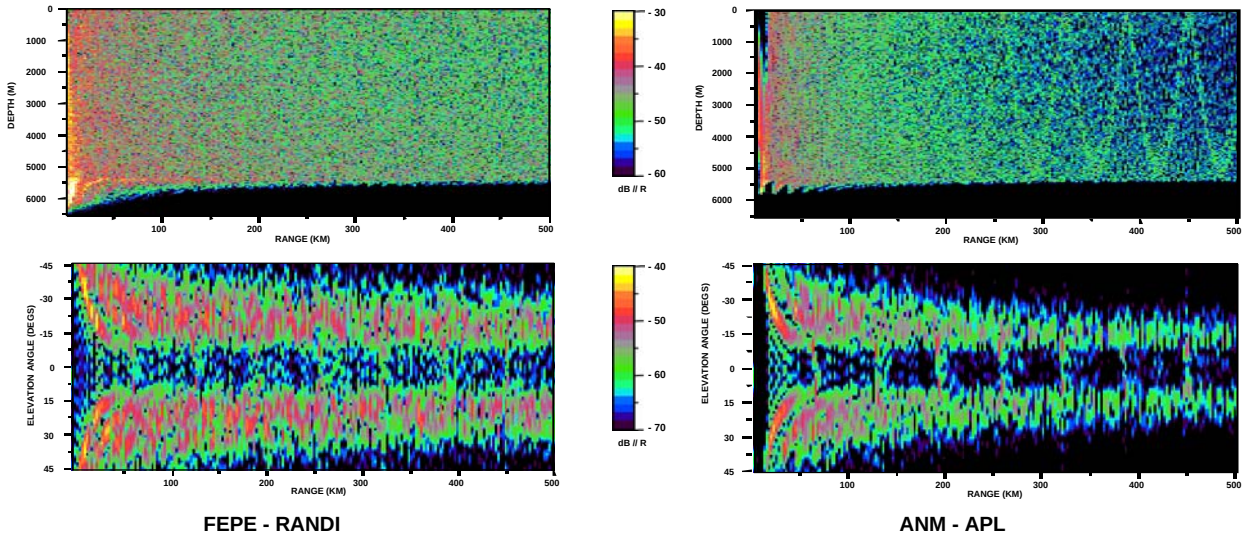

Fig. 11 — Propagation/Environment acoustic field comparisons for the Sargasso Sea range-independent track: (left panels) FEPE propagation model / RANDI environment; (right panels) ANM propagation model / APL environment; (top panels) range-depth distribution of the acoustic field; (bottom panels) vertical-arrival structure vs range

An inspection of the acoustic field for both models (top plots) indicates that the field is dominated by the energy that interacts with the sediment layer. This energy is either reflected at the water-sediment interface or is transmitted into the sediment, then refracted back to the interface by the strong compressional speed gradient, and then transmitted back into the water column or reflected back into the sediment, etc. Note that the convergence zone structure commonly associated with Sargasso Sea propagation is barely visible in the APL field and not visible in the RANDI field. The comparative insignificance of the convergence zone structure is a consequence of the relatively small depth excess for

the 5 m source depth[2] (see Table A1 of Appendix A). The convergence zone structure is visible in the APL field and not in the RANDI field because the sediment-interacting component of the RANDI field is larger than that in the APL field.

The vertical-arrival structure plots for the two models show that, for most source ranges, the energy is concentrated in narrow elevation angle sectors to either side of the horizontal. The minimum elevation angle for these sectors in both plots is about $\pm 10°$. This angle corresponds to the minimum arrival angle for the sediment-interacting energy, θ_{sw}, listed in Table A1. The maximum angle of the sediment-interacting sector is over $\pm 45°$ at about 5 km. This angle decreases with range since the higher order modes, which contain the high-angle energy, are attenuated more rapidly with range than the lower order modes. Finally, note that at the convergence zone ranges (about 65 km intervals), the vertical-arrival structure shows contributions that extend below the sediment-interacting limit to an angle of about $\pm 8°$, which is comparable to the waterborne limit, θ_w, listed in Table A1. This energy is the vertical resolution of the waterborne energy.

A comparison of the field and the arrival structure plots for the two models shows that the energy falls off much faster with range for the APL model than for the RANDI model. To quantify the difference between the two fields, we have computed propagation curves for the different propagation/environment components of Section 3. These curves are computed as a function of range by averaging over the same 204 m depth interval used to determine the vertical-arrival structure (48 m to 252 m). The results are shown in Fig. 12. The four plots in the figure correspond to the propagation/environment comparison (top left), the FEPE/ANM propagation-only comparison (top right), the RANDI/APL environment-only comparison (bottom left), and the ANM-KRAKEN/ANM-UT adiabatic-normal-mode propagation model comparison (bottom right). The propagation curves determined by the different propagation/environment components are color coded as follows: the RANDI noise model with the FEPE propagation model and the RANDI environment (blue curve), the APL noise model with the ANM-UT propagation model and the APL environment (red curve), the ANM-KRAKEN propagation model with the RANDI environment (green curve) and ANM-KRAKEN propagation model with the APL environment (black curve). This plot format and color correspondence will be used throughout this report.

The comparison of the four plots in Fig. 12 indicates that the difference in the propagation loss between the RANDI and the APL noise models is due to the difference in the environmental components and not to the difference in the propagation models. According to the propagation/environment plot (top left), the difference in the energy fall-off with range results in a difference of about 7 dB in the propagation loss over the 500 km range interval. As seen in the propagation-only plot (top right), the FEPE curve (blue) and the ANM curve (green) lie within one dB of each other, except at the very short ranges, where the abnormally low levels for the ANM curve result from neglecting the high-order modes that interact with the subbottom. This indicates that the difference in the propagation models is not a significant cause of the difference in the propagation curves. This is not surprising since the two models should produce comparable results for a range-independent environment. On the other hand, an inspection of the environment-only comparison plot (bottom left) shows that the APL propagation loss (black) is almost 6 dB less than the RANDI curve (green), indicating that the difference in the environments accounts for most of the 7 dB difference in the propagation/environment curves. Finally, the similarity in the red and the black propagation curves in the ANM model comparison plot (bottom right) indicates that the difference in the ANM propagation models is not a factor.

[2] Computations for a deeper source depth, 150 m, show a much stronger convergence zone structure.

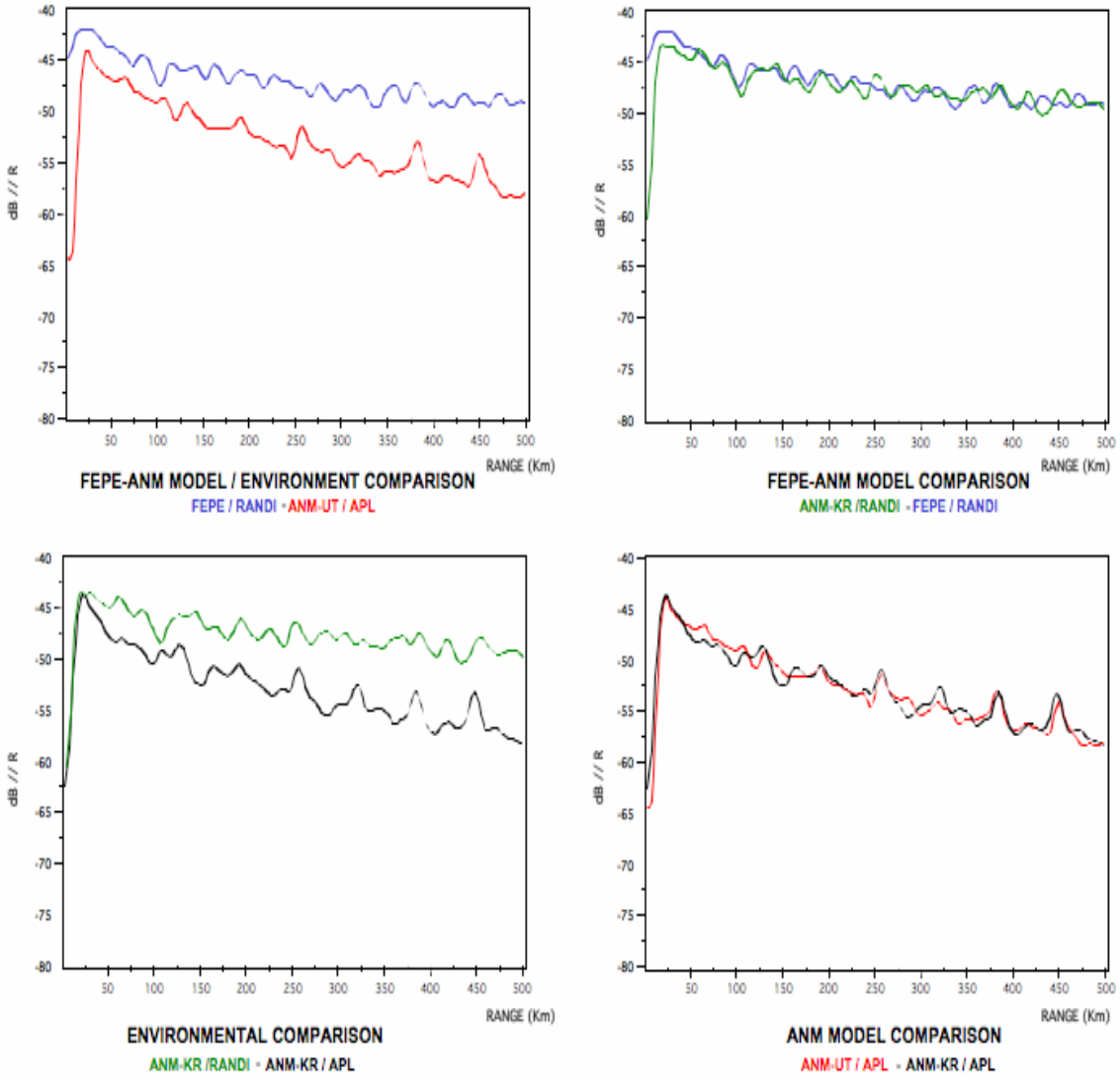

Fig. 12 — Depth-averaged propagation curves for the Sargasso Sea range-independent track: propagation/environment comparison (top left); propagation-only comparison (top right); environment-only comparison (bottom left); and ANM model comparison (bottom right)

The preceding analysis indicates that the large difference in the RANDI and the APL acoustic fields is due to the difference in the amount of the sediment-interacting energy and that this difference is due to the difference in the two environments. As noted earlier, the water-column sound speed, the water depth, and the sediment depth for the two environments are comparable. Thus, the two environments differ primarily in the sound-speed ratio, the sediment density, and the sediment attenuation profile. For the RANDI environment, the large sound-speed ratio (greater than unity) results in the total reflection of energy at grazing angles less than a critical angle of about 11°. Furthermore, the larger density for the RANDI environment results in a larger impedance contrast at the interface, and hence, the reflection of a larger fraction of the energy at grazing angles greater than the critical angle. Finally, the smaller near-surface attenuation for the RANDI environment results in a larger fraction of the energy that is transmitted into the sediment being available for transmission back into the water column.

To assess the relative importance of these factors, we have computed averaged propagation curves by replacing each of the three factors (the sound-speed ratio, the sediment density, and the attenuation

profile) in the RANDI environment by the corresponding quantity in the APL environment. The resulting propagation curves are shown in Fig. 13. Each plot in the figure is identified by a three-letter code: the first letter corresponds to the sound-speed ratio, the second to the density, and the third to the attenuation. The individual designators in the code are zero if the corresponding quantity has not been replaced in the RANDI profile and have a letter value if the quantity has been replaced in the RANDI profile. The letter values are "r" for the sound-speed ratio, "d" for the density, and "a" for the attenuation. Thus, the code "000" designates the RANDI profile itself, and the code "rda" designates the profile obtained by replacing the sound-speed ratio "r", the density "d", and the attenuation profile "a" in the RANDI profile by the corresponding quantities from the APL environment. This process results in decreasing the sound-speed ratio from 1.0200 to 0.9960, decreasing the density from 3.9 to 1.4, and increasing the surface attenuation from 0.0095 dB/λ to 0.0281 dB/λ.

An inspection of the plots of Fig. 13 indicates that all three environmental factors are significant contributors to the difference in the sediment-interacting energy. If only one factor is changed, the largest decrease in transmission loss, about 3 dB at 500 km, results from changing the sound-speed ratio (compare black and yellow curves). A change in only the density or in only the attenuation results in a decrease of only about 2 dB. Thus, for a single parameter change only, the largest decrease in the sediment-interacting energy results from decreasing the reflected energy by eliminating the critical angle, rather than decreasing the reflected energy by decreasing the impedance or by increasing the loss in the refracted energy.

If two of the three environmental parameters are changed, a change in the sound-speed ratio and either the density or the attenuation results in the largest decrease in the propagation loss (about 2 dB at the long ranges). A change in the density and the attenuation results in a decrease of only about 1 dB at long ranges. Note that although the change in the sediment interaction energy due to the ratio-density change is comparable to that of the ratio-attenuation change, the propagation mechanisms by which these changes occur are fundamentally different. The ratio-density change reduces the sediment-interacting energy by reducing the reflection coefficient (from about 60 percent to about 20 percent), whereas the ratio-attenuation change reduces the sediment-interacting energy by increasing the loss of the sediment-refracted energy that is transmitted back into the water column.

Finally, note that changing all three environmental parameters results in a further reduction of the long range propagation loss of over three dB. This indicates that the comparatively small amount of sediment-interacting energy for the APL environment is caused not only by more of the sediment-interacting energy being transmitted into the sediment but also by the greater attenuation of that energy.

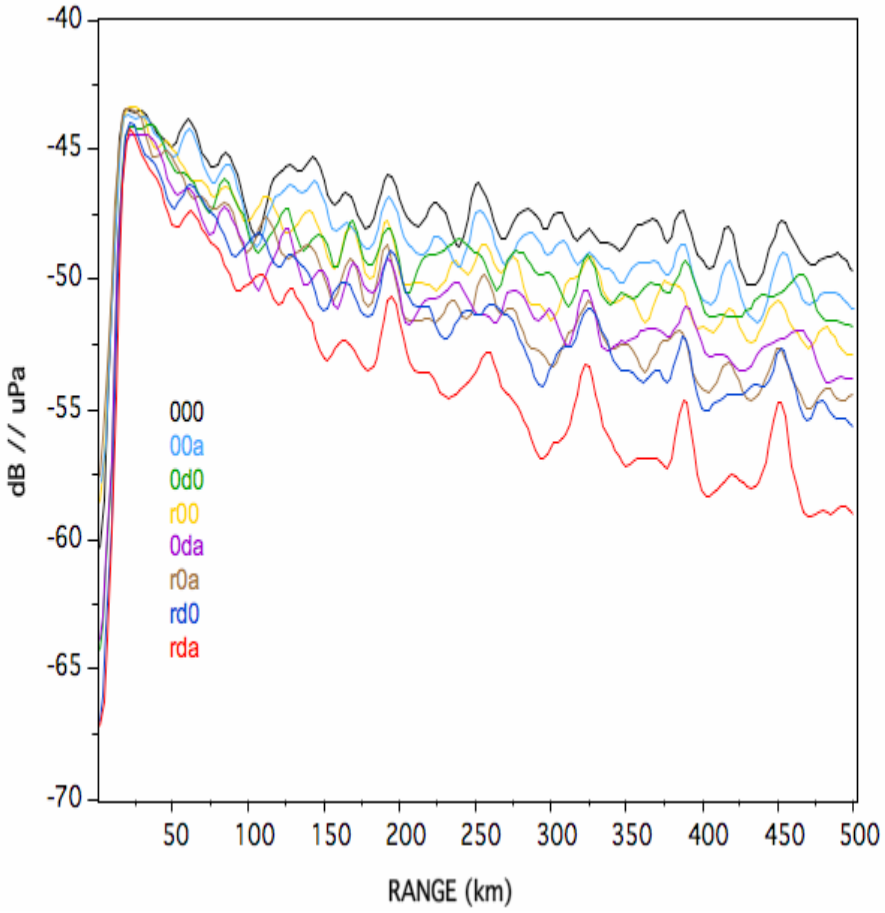

Fig. 13 — Depth-averaged propagation curves for the Sargasso Sea for different range-independent environments: 000, RANDI environment; 00a, RANDI environment with APL attenuation; 0d0, RANDI environment with APL sediment density; r00, RANDI environment with APL sound-speed ratio; 0da, RANDI environment with APL density and attenuation; r0a, RANDI environment with APL sound-speed ratio and attenuation; rd0, RANDI environment with APL sound-speed ratio and density; rda, RANDI environment with APL sound-speed ratio, density, and attenuation

To provide an alternate perspective on the impact of the differences in the environments, we have plotted the modal components of the acoustic fields for the two environments in Fig. 14. The modal components for the RANDI field are shown on the left; those for the APL field are shown on the right. In each set, the top plot shows the depth-mode distribution of the energy in the array-mode functions, $\left|\varphi_m^a(z)\right|^2$; the bottom plot shows the range-mode distribution of the energy in the source-mode function $\gamma(m, r_s)$. It follows from the definitions of these quantities in Section 3 that the term-by-term product of a horizontal slice from the top plot at the receiver depth z and a horizontal slice from the bottom plot at the source range r_s is equal to the magnitude-squared of the terms in the modal expansion of the acoustic field at depth z and range r_s, weighted by r_s. The sum of these terms has been referred to as the incoherent transmission loss (Ref. 9, Chapter 5). The format of the plots in Fig. 14 is followed throughout this report.

For the range-independent environments shown in Fig. 14, the source modes are independent of range and equal to the array modes, $\varphi_m(z_s, r_s) = \varphi_m(z_s, 0) = \varphi_m^a(z_s)$. Furthermore, the mode attenuation, $\alpha_m(r_s) = \mathrm{Im}\left[k_m(r_s)\right]$, is independent of range so that the attenuation integral is simply equal to the mode attenuation at the array site times the source range. Thus, for the range-independent track, the

source-mode function is completely determined by the mode quantities at the array site, and the range dependence appears only through the mode attenuation loss, $\beta(m, r_s) = \exp\{-2\alpha_m r_s\}$.

As seen in the top plots of Fig. 14, the envelopes of the array-mode functions for the two environments are approximately the same for depths down to the water depth. This is not surprising because the envelopes are determined by the sound speed and the sound speed profiles in the water column for the two environments are essentially equal. For depths greater than the water depth, the two envelopes differ since the compressional sounds speeds differ. For the RANDI environment, the envelope is essentially independent of depth for mode numbers from 80 to about 140. These modes describe the totally reflected energy that results from the critical angle corresponding to the larger than unity sound-speed ratio. For the APL environment, the envelope continues to decrease as the depth decreases since the sound-speed ratio is less than unity, and hence, there is no totally reflected energy.

The main difference in the array-mode functions within the envelopes also appears in the sediment layer. In the water column, there is almost no difference except for the larger mode numbers (> 320), where the RANDI levels are a few dB greater than the APL levels. However, as seen in the bottom plots, the source-mode functions do not contain significant energy at these large mode numbers for all but the smallest ranges. Thus, excluding these small ranges, the array-mode functions for the two environments are equivalent for the array depths relevant to the current analysis (48 to 252 m).

An inspection of the bottom plots of Fig. 14 indicates that both the band of mode numbers containing significant energy and the energy within that band are larger for the RANDI environment. This is expected since it is the difference in the energy in the source-mode function that accounts for the larger energy in the RANDI acoustic field. To relate this difference to the environmental differences, we first identify the mode limits that specify the modal decomposition. To this end, we recall that for range-independent environments, the array modes are the same as the source modes at all ranges so that the mode-band limits that are determined by the envelope of the source modes $\varphi_m(z, r_s)$ are also determined from the envelope of the array modes $\varphi_m^a(z)$, which are shown in the top plots. Since the envelopes of the array modes for the two environments are essentially the same in the water column, the waterborne limits are essentially the same. The lower limit of the waterborne energy $M_{w,l}$, which is determined from the envelope sampled at the source depth z_s, is 68 for both environments and the upper limit $M_{w,u}$, which is determined from the envelope sampled at the water depth z_w^-, is 84 for the RANDI environment and 85 for the APL environment. The energy in this waterborne band is the same for both environments. For the RANDI environment, there is a total-reflection band with an upper limit, $M_{tr,u}$, determined from the envelope sampled at the water depth z_w^+. This limit is about 119. The energy in this band does not decrease significantly with range because the attenuation is negligible. For the APL environment, there is no total-reflection band because the sound-speed ratio is less than unity. The remaining band is the sediment-refraction band which extends for modes greater than 119 for the RANDI environment and for modes greater than 85 for the APL environment. The upper limit of this band is determined by the mode attenuation loss which, expressed in decibels, is $-\alpha_m r_s 10 \log e$. Thus, for the range-independent case, the upper limit of the sediment-refraction band is a contour of $-\alpha_m r_s$. As seen in the figure, the upper limit is much larger for the RANDI environment than for the APL environment (e.g., at 500 km, the RANDI upper mode limit is about 229, whereas the APL upper limit is only about 167). This difference results because the mode attenuation α_m for the APL environment is much larger than the mode attenuation for the RANDI environment. This is expected from the analysis of the effect of the differences in the geoacoustic parameters described above. Taken together, these observations indicate that the larger energy in the RANDI field is due to two factors: (1) the presence of a total-reflection band with negligible attenuation that results from a sound-speed ratio greater than unity, and (2) a much smaller mode attenuation in the sediment-refraction band that results from the differences in all of the geoacoustic

parameters. The mode-band limits for the waterborne and the total-reflection bands are indicated on the figure along with the upper limit of the sediment-refraction band at a range of 500 km.

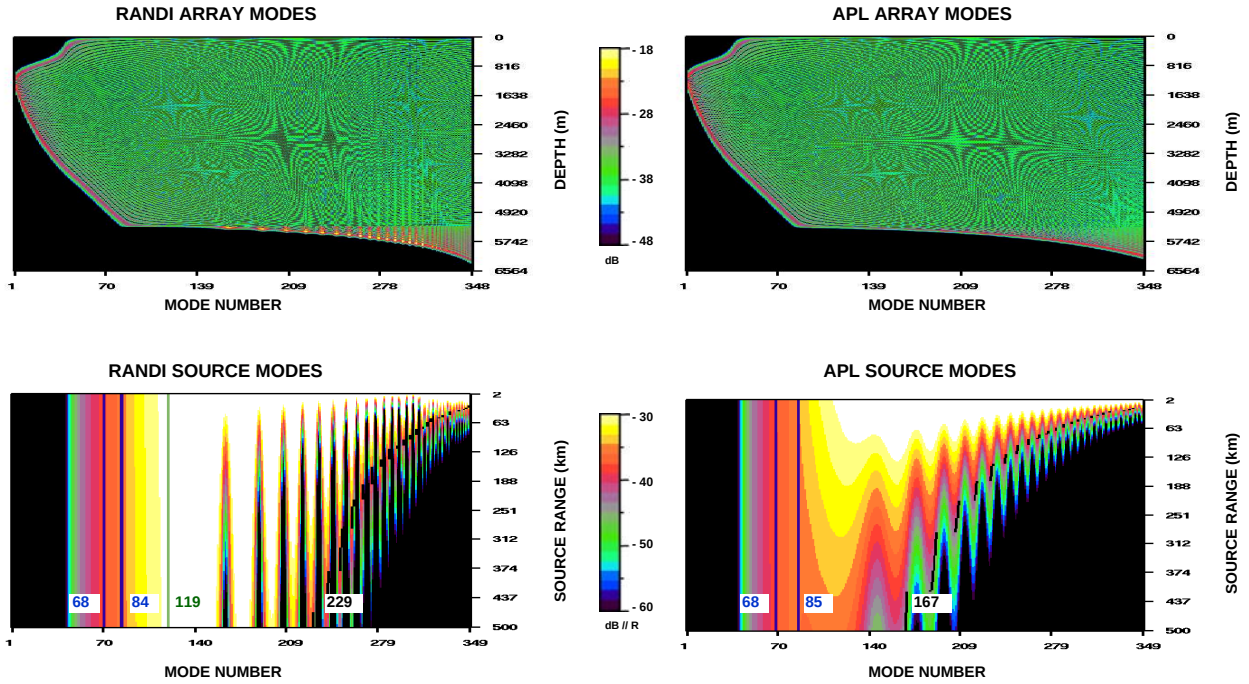

Fig. 14 — Mode function components for the RANDI and the APL Sargasso Sea range-independent track: (top panels) array-mode functions; (bottom panels) source-mode functions; (left panels) RANDI components; (right panels) APL components

4.2 Deep-Water Track

The two environments for the deep-water track are illustrated in Figs. 15 and 16. Figure 15 shows the sound-speed fields for the RANDI environment (top) and for the APL environment (middle) as a function of range and depth. The bathymetry for each environment is shown in the bottom plot. Note that the scales on both the range axis and the depth axis for the sound-speed fields are not linear and that the scales for the two axes are different for the two environmental models. The scale on the depth axis is the same for both sound-speed fields down to a depth of 3000 m. Below 3000 m, the depth scales differ due to a different method of extrapolating the sound speed to the bottom. The scale on the range axis, which is linear in the profile index, is different for the two environments because the range sampling for the APL environment is significantly coarser than for the RANDI environment. This comparative sparseness of the APL environment profiles, which holds for the deep-water portions of all of the tracks considered in this report, is a consequence of the different environmental construction algorithms used in the two models (see Section 3).

An inspection of the sound-speed fields in Fig. 15 indicates that the APL sound speed varies along the full length of the track, whereas the RANDI sound speed is independent of range out to nearly the end of the track. At the beginning of the track, the APL sound speed almost has a near double-duct form, characterized by an inflection in the sound speed at a depth of around 500 m (see Fig. 10). Near the middle of the track, the near double-duct gives way to a single duct as the inflection at 500 m is diminished. As the range increases further, the sound speed in the upper water column continues to increase. In contrast, the RANDI sound speed is independent of range out to the very last profile, where it takes the form of the APL profile at the end of the track.

The bathymetry (lower plot) shows a total variation of roughly 800 m along the track for both environments. This appears as a decrease in the water depth of about 300 m out to almost 600 km, followed by an increase of about 800 m out to about 750 km, followed by a comparatively flat segment out to about 1350 km, followed by a decrease of almost 800 m out to the end of the track. Note that the RANDI bathymetry exhibits significantly more local variation than the APL bathymetry (e.g., the two small seamounts located at about 350 km and about 560 km in the RANDI bathymetry are not evident in the APL bathymetry). This results because of the coarser range sampling for the APL environment in the deep-water portions of the track.

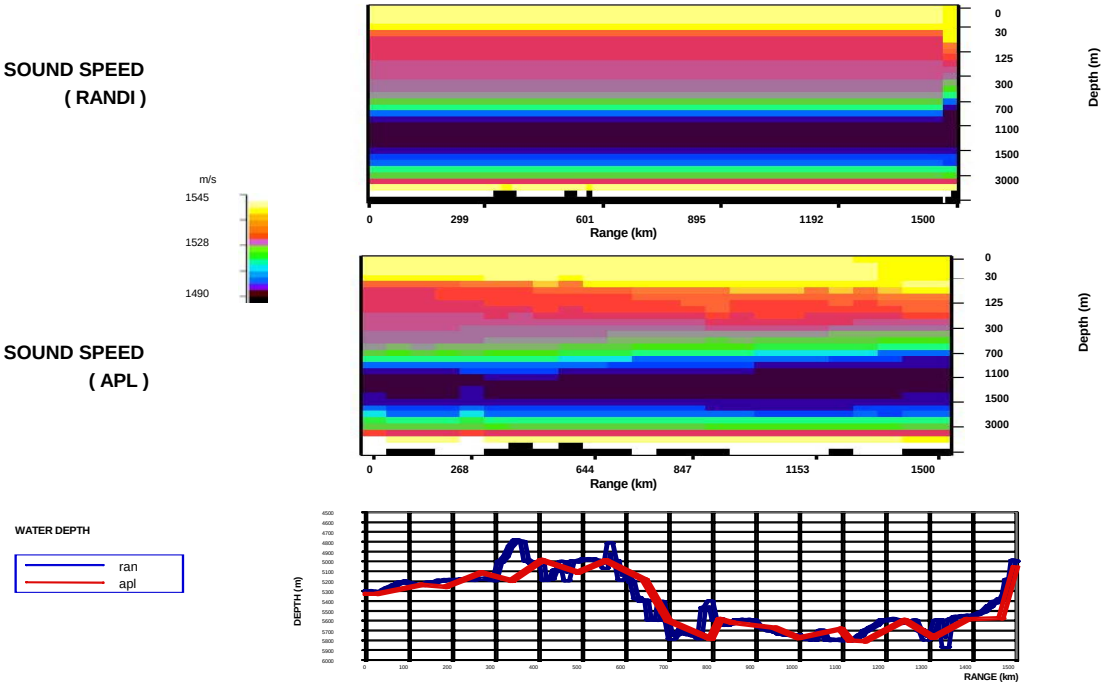

Fig. 15 — Sound speed and bathymetry comparisons for the Sargasso Sea deep-water track: RANDI sound-speed field (top); APL sound-speed field (middle); water depth comparison (bottom)

The four geoacoustic parameters (sound-speed ratio, sediment density, interface attenuation, and sediment thickness) for both environments are illustrated in the plots of Fig. 16. The full compressional sound-speed field and the attenuation field for both environments are illustrated in Appendix A.

An inspection of the plots in Fig. 16 indicates that the sound-speed ratio (top left) for the RANDI environment is greater than unity except for ranges between 75 and 275 km and ranges greater than about 1150 km. On the other hand, the APL sound-speed ratio is less than unity except between about 800 and 1100 km, where it is slightly larger than unity. Thus, for both environments there are range segments where there is a critical angle below which all incident energy is reflected without loss. The sediment density plot (bottom left) shows that the RANDI density is generally larger than the APL density. These larger densities, together with the larger sound-speed ratios, result in larger impedance differences at the water-sediment interface, and hence, larger reflection coefficients for the regions where the energy interacts with the sediment. The interface attenuation plot (bottom right) indicates that the attenuation at the sediment-water interface is larger for the APL environment than for the RANDI environment. However, as was the case for the range-independent track, the RANDI attenuation is larger than the APL attenuation at all depths except near the top of the sediment layer (see the attenuation field plots in Appendix A). The sediment thickness for the RANDI environment exceeds 300 m along the full length of

the track. Taking into account the 1000 m extension (not included in the figure), the sediment thickness for the APL environment is considerably larger than that for the RANDI environment.

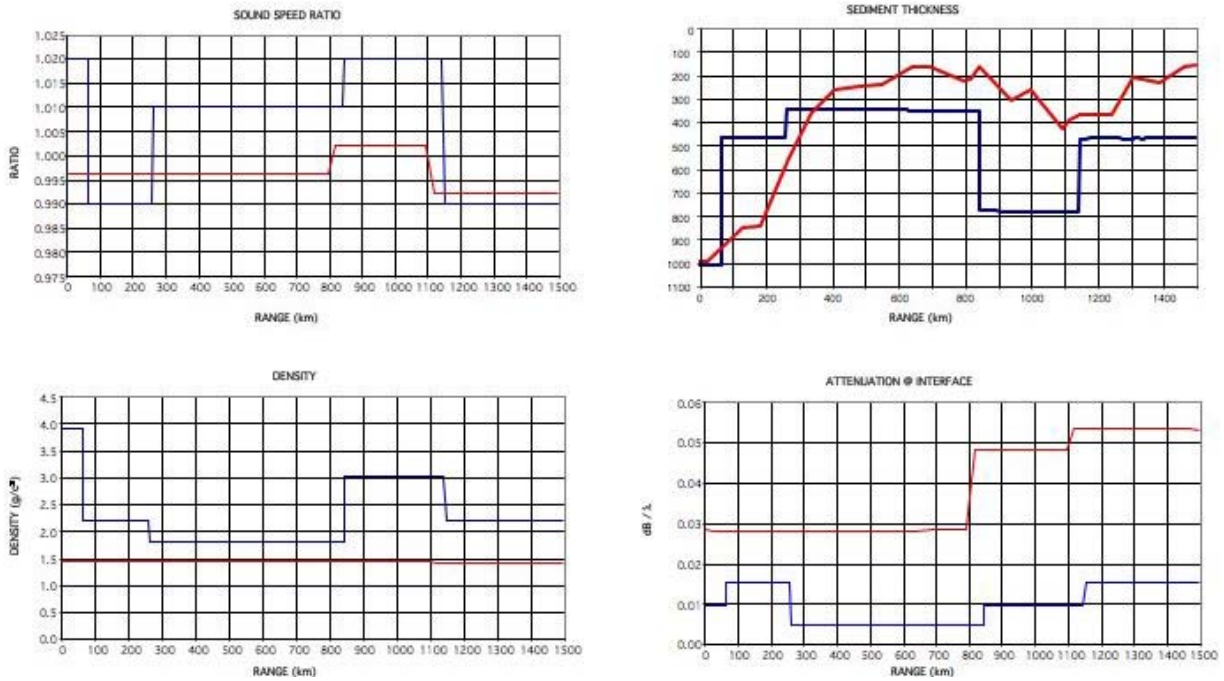

Fig. 16 — Geoacoustic parameters for the APL environment (red) and the RANDI environment (blue) on the Sargasso Sea deep-water track: sound-speed ratio (top left); sediment thickness (top right); sediment density (lower left); and interface attenuation (lower right)

In Fig. 17, we have plotted the acoustic field and the vertical-arrival structure as a function of source range for the deep-water track in the same format as Fig. 11. As seen in the figure, both the field and the arrival structure are similar to those for the range-independent track. For both tracks, the field is dominated by the sediment-interacting component. Furthermore, the energy in the APL field falls off much faster with range than the energy for the RANDI field. This similarity to the range-independent case is not surprising since the environment for the deep-water track is roughly the same as the range-independent environment.

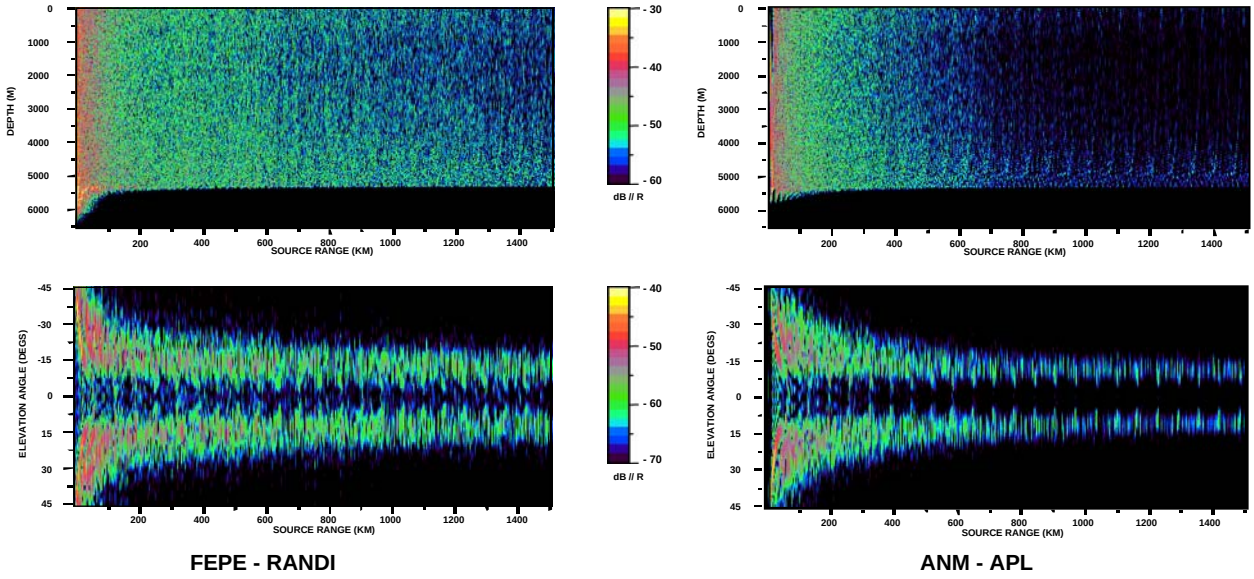

Fig. 17 — Propagation/environment acoustic field comparison for the Sargasso Sea site deep-water track: (left panels) FEPE propagation model / RANDI environment; (right panels) ANM propagation model / APL environment; (top panels) range-depth distribution of the acoustic field; (bottom panels) vertical-arrival structure vs range

The propagation curve comparisons for the deep-water track are plotted in Fig. 18 with the same format and color coding as the range-independent comparisons of Fig. 12. An inspection of these plots indicates that, as was the case for the range-independent track, the difference in the propagation loss between the RANDI and the APL noise models is largely due to the difference in the environments and not to the difference in the propagation models.

The analysis is analogous to that of the range-independent track. According to the propagation/ environment plot (top left), the difference in the energy fall-off with source range results in a difference of about 7 dB in the propagation loss over the 1500 km range interval. As seen in the propagation-only plot (top right), the FEPE curve (blue) and the ANM curve (green) lie within two dB of each other. This indicates that the difference in the propagation models is not a major cause of the difference in the propagation curves. This is not surprising since the two models should produce comparable results for the comparatively weak range dependence of the deep-water track. On the other hand, the environment-only plot (bottom left) shows that the APL environment energy (black) is almost 7 dB less than the RANDI environment energy (green), indicating that the difference in the environments accounts for most of the 7 dB difference in propagation/environment curves. Finally, the similarity in the red and the black propagation curves in the ANM model comparison plot (bottom right) indicates that, as for the range-independent track, the different ANM propagation models are not a factor.

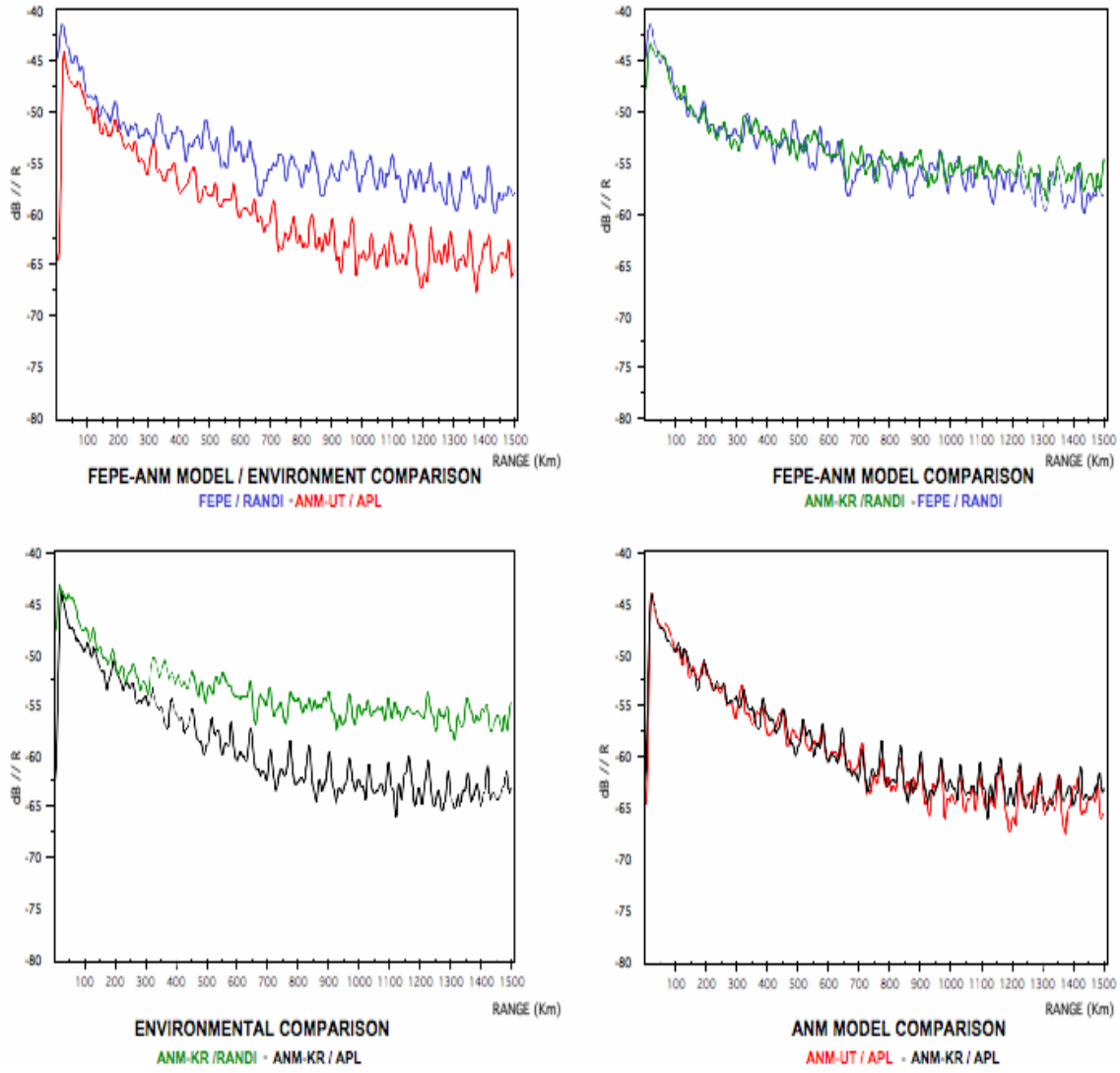

Fig. 18 — Depth-averaged propagation curves for the Sargasso Sea deep-water track: propagation/environment comparison (top left); propagation-only comparison (top right); environment-only comparison (bottom left); and ANM model comparison (bottom right)

To quantify the difference in the arrival structure for the two models, we have computed range averages of the arrival structure for the different propagation component comparisons. The results are shown in Fig. 19. The averages are computed over the range interval from 1000 to 1400 km. The format and color coding of the figure are the same as that used for the propagation curve comparison plots.

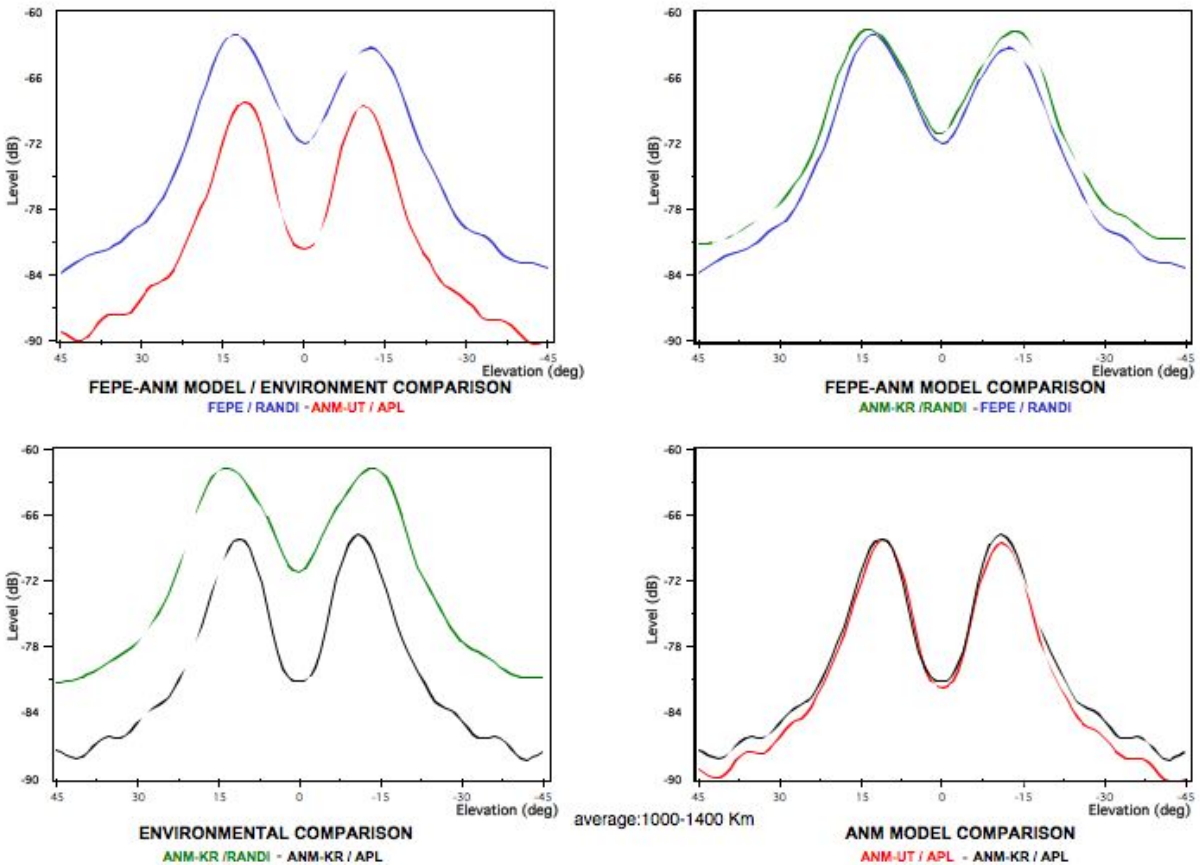

Fig. 19 — Range-averaged vertical-arrival structure for the Sargasso Sea deep-water track: propagation/environment comparison (top left); propagation-only comparison (top right); environment-only comparison (bottom left); and ANM model comparison (bottom right)

An inspection of the propagation/environment plot of Fig. 19 indicates that the overall energy in the arrival structure is greater for the RANDI model than for the APL model and that the depth of the notch is less. In particular, the peaks in the arrival structure for the RANDI model are about 5 dB greater than for the APL model and the depth of the notch for the RANDI model is about 4 dB less (about 9 dB compared to about 13 dB). An analysis of the remaining plots in the figure, analogous to that of the propagation curve comparisons plots, indicates that these level differences are almost entirely due to the difference in the environments and not the propagation models.

Finally, note that the separation between the peaks in the arrival structure is somewhat larger for the RANDI model than for the APL model — about 25° for the RANDI model, but only about 22° for the APL model. An inspection of the environment-only plot (lower left) indicates that the separation for the APL environment is about 5° smaller than the separation for the RANDI environment. On the other hand, the propagation-only plot (upper right) indicates that the separation for the ANM model is about 2° larger than the separation for the FEPE model. Taken together, these results indicate that the larger separation for the RANDI model occurs because the smaller separation for the FEPE model is more than offset by the larger separation for the RANDI environment. The difference in peak angles is in contrast to what would be expected from the range-independent parameters. These parameters result in a minimum sediment-interacting angle for the RANDI environment that is about 0.4° less than that for the APL environment (see Table A1).

The preceding analysis indicates that the differences in the acoustic fields are primarily due to the differences in the environments. To gain insight into these differences, we first consider in greater detail the differences in the propagation curves for the environment-only comparison plots in the lower left hand corner of Fig. 19. An inspection of this plot indicates that out to a range of about 330 km, the two propagation curves fall off at about the same rate. At about 330 km, the RANDI curve shows a sharp increase of about 2 dB. As the range increases beyond 330 km, the RANDI fall-off rate decreases to the point that there is only about a 5 dB decrease in the energy over the remaining 1200 km. In contrast, for ranges greater than 330 km, the APL propagation curve continues to fall off at a rate comparable to that at the shorter ranges out to about 800 km. Beyond 800 km, the APL fall-off decreases to a rate only slightly greater than that of the RANDI propagation curve. The waterborne contribution to the APL propagation is clearly visible as the peaks in the curve at the CZ ranges; the peaks are not clearly evident in the RANDI propagation curve.

The differences in the environment-only propagation curves over the first half of the deep-water track can be largely explained in terms of the geoacoustic parameters using the analysis results from the range-independent track. Consider first the APL propagation curve. A detailed comparison of the deep-water and the range-independent propagation curves indicates that the large fall-off rate for the APL propagation in the first 800 km of the deep-water track is comparable to that of the range-independent track. This is not surprising since the geoacoustic parameters (sound-speed ratio, density, and interface attenuation) for the APL environment are the same as those for the range-independent track over this range interval. Thus, the only difference in the deep-water propagation and the range-independent propagation is due to the range dependence of the water-column sound speed and the bathymetry variation. These environmental differences cause the sediment-interacting energy at 500 km to be about one dB lower on the deep-water track and the waterborne energy at the nearest CZ to be between one and two dB lower. We discuss the impact of the range variation in the sound speed and the bathymetry later in the subsection.

We turn next to the RANDI propagation curve. Out to a range of about 300 km, the RANDI propagation curve falls off at a rate comparable to that of the APL propagation curve. Over a substantial portion of this segment (about 50 km to 280 km), the sound-speed ratio is less than unity with a value comparable to that of the APL environment (0.990). Similarly, over this range interval, the RANDI density is reduced to within a factor of 1.5 of the APL density, and the RANDI attenuation remains within a factor of two of the APL interface attenuation. Thus, the RANDI geoacoustic parameters roughly approximate the “rd0” case from the range-independent track analysis. As seen in that analysis, the “rd0” propagation curve falls off at a rate that approaches the APL propagation curve.

Over the range interval from 300 km to 800 km, the fall-off rate for the RANDI propagation curve decreases dramatically. Slightly before the beginning of this interval (about 280 km), the sound-speed ratio increases from a value less than unity to a value greater than unity (1.01). Furthermore, both the density and the attenuation remain small. Thus, the change in the sound-speed ratio, together with the values of the other parameters, approximates the “0d0” case for the range-independent track. For this case, there is a much smaller fall-off rate than for the “rd0” case that applies to the 50 km to 280 km range interval.

Over the last half of the range interval, there is only a loose correspondence between the propagation curves and geoacoustic parameters. For the APL environment, the decrease in the fall-off rate at 800 km is accompanied by an increase in the sound-speed ratio from a value less than unity to a value slightly greater than unity (1.0025). The density remains constant, but there is an increase in the interface attenuation. Ignoring the attenuation increase, the APL geoacoustic parameters roughly approximate the “0da” case. For this case there is a substantial reduction in the fall-off rate compared to the “rda” case. Nevertheless, the “0da” fall-off rate significantly exceeds the long range fall-off rate seen in the APL curve of Fig. 18. For the RANDI environment, the reduction in the fall-off rate at 800 km is accompanied

by an increase in the density and an increase in the sound-speed ratio to an even larger value (1.0025 vs. 1.01). The interface attenuation stays about the same. According to the range-independent track analysis, these changes should decrease the fall-off rate, but not to the extent seen in the RANDI propagation curve of Fig. 18. Furthermore, the RANDI sound-speed ratio decreases to a value less than unity. This would dramatically increase the fall-off rate beyond that seen in Fig. 18.

The deficiencies in the geoacoustic interpretation for the long range propagation curves are most easily explained in terms of the mode function components. These quantities are plotted in Fig. 20 in the same format as the range-independent mode components of Fig. 14. Note that the array-mode functions (top panels) are the same as those for the range-independent track. This results because the environment profiles at the array site are the same as those for the range-independent track for both environments. Thus, for both environments, the difference in the propagation between the deep-water track and the range-independent track is due only to the difference in the source-mode functions (bottom panels).

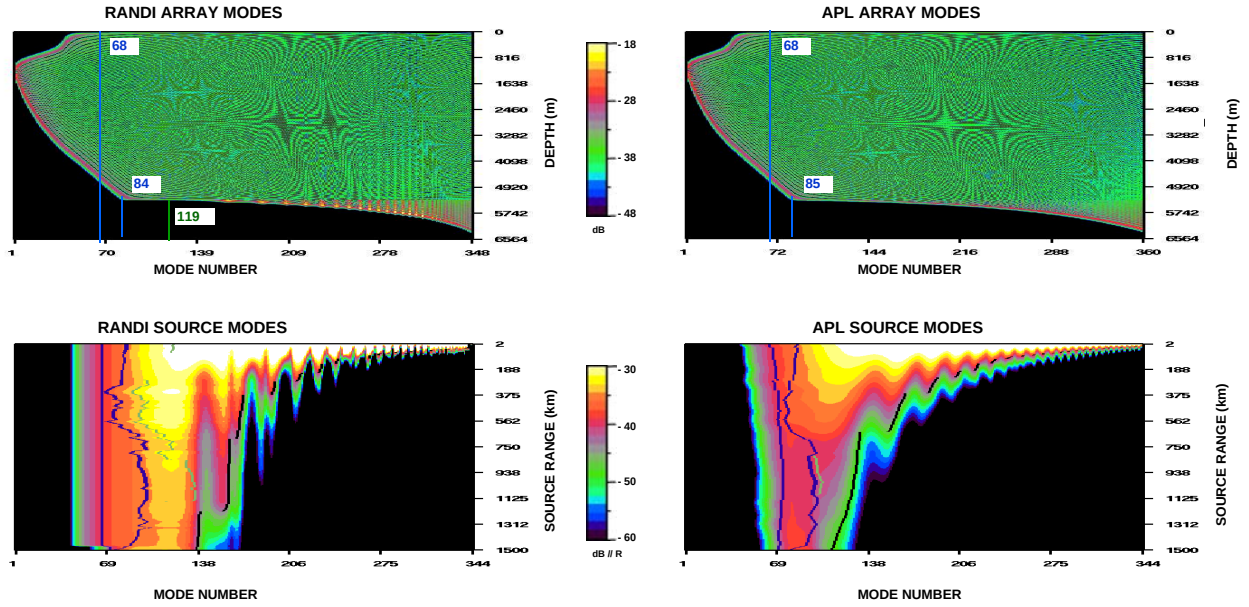

Fig. 20 — Mode function components for the RANDI and the APL Sargasso Sea deep-water track: (top panels) array-mode functions; (bottom panels) source-mode functions; (left panels) RANDI components; (right panels) APL components

An inspection of the bottom plots of Fig. 20 indicates that, as for the range-independent track, there is considerably more energy in the RANDI source-mode function than in the APL function. This is expected for the first half of the track in the light of the preceding discussion on the impact of the geoacoustic parameters on the propagation. To interpret the difference in the propagation loss for the last half of the track, we describe the decomposition of the mode band into the waterborne, the totally reflected and the sediment-refracted modes.

We first consider the waterborne modes. The lower limit of the waterborne band is determined by the sound-speed field at the 5 m source depth. As was seen in Fig. 15, the sound-speed field for the APL environment varies continuously along the track; whereas, the sound-speed field for the RANDI environment is constant up to the last 50 km, where it changes abruptly to a profile that is similar to the last profile in the APL environment. It follows that the lower limit of the mode band for the RANDI environment (leftmost blue curve) is independent of range, except at the end of the interval, where it increases sharply from its value at the array site. For the APL environment, the lower limit increases gradually over the length of the range interval until it becomes approximately equal to the RANDI lower

limit at the final range (about 71). Thus, the effect of the sound speed variation in the APL environment is to decrease the extent of the mode band, and hence, to decrease the waterborne energy in the field. This results in a small decrease in the energy in the APL propagation curve in addition to that attributable to the geoacoustic parameters describe above. Note that most of this decrease occurs in the first 750 km.

The upper limits of the waterborne band are determined from the sound speed evaluated at the water depth. These limits are approximately equal since the deep-water sound speeds and the large scale variations in the bathymetries for the two environments are approximately equal. As seen in the figure, the upper limits (right-most blue curves) decrease from about 84 at the array site to the mid 70s between 500 km and 600 km, and then increase to the high 90s between 700 km and 1350 km, and finally decrease to the mid 70s at the end of the track. According to the discussion in Section 3, an increase in the upper limit of the waterborne modes causes modes that were sediment-interacting to become waterborne modes. This can result in a significant reduction in the mode attenuation loss, provided that these modes were sediment-refracting and not totally reflecting modes. This is the case for the bathymetry-induced increase in the upper limit that occurs around 700 km for the APL source-mode function. As seen in the figure, this increase in the upper limit causes the rate of change in the mode attenuation loss for the affected modes to decrease dramatically. Thus, it is the nearly 800 m increase in the water depth that occurs between 600 km and 700 km that is the major cause of the reduction in the rate of decrease in the energy in the APL field. The bathymetry-induced increase in the upper mode limit for the RANDI environment causes modes that were totally reflecting to become waterborne modes. However, this does not result in a reduction in the attenuation loss for those modes since the attenuation loss for totally reflecting modes is negligible.

We note in passing that according to the discussion in Section 3, changes in the bathymetry also result in changes in the energy in the waterborne band. This is most apparent in the RANDI source-mode function since the source modes are not affected by a range-dependent, sound-speed field and the small-scale range variation of the bathymetry is more severe than for the APL environment. In particular, it is seen in the lower left hand plot that there are local minima in the -35 dB contour at about 345 km and about 560 km that correspond to the two seamounts in the RANDI bathymetry. The former is the cause of the 2 dB increase in the RANDI energy that occurs at about this range. Similarly, there is an increase in the -35 dB contour over the range interval of increased water depth between about 700 km and about 1400 km followed by a decrease in this contour at 1450 km, where the water depth decreases substantially. Similar variations can be seen in the APL source-mode function by tracing the -45 dB contour (gray). These variations are less dramatic since the APL bathymetry variations are less severe.

We next consider the total-reflection band. This band occurs only when the sound-speed ratio is greater than unity. Thus, for the APL environment there is no total-reflection band except over the interval from 800 km to 1100 km, where the small sound speed excess introduces a small total-reflection band than spans no more than 5 modes. For the RANDI environment, there is a total-reflection band at all ranges except for the interval between about 60 km and 280 km and for ranges greater than 1130 km. In the interval from zero to about 60 km, the upper limit is about 119, which is the value at the site. From 280 km to about 650 km, the upper limit varies from 89 and 100; from 650 km to 830 km, the upper limit increases from 100 to 135, where it levels off out to a range of 1100 km.

In analogy to the waterborne modes, the introduction of a total-reflection band or alternatively, an increase in its upper limit, reduces the mode attenuation loss by changing modes from sediment-refraction to total-reflection modes. This is clearly seen in the RANDI source-mode function over the range interval from about 280 km to about 1150 km, where the levels are essentially independent of range for modes less than the upper limit of the total-reflection band. Thus, it is the introduction of the total-reflection band by the increase in the sound-speed ratio at 280 km that is the primary cause of the reduction in the RANDI fall-off rate that occurs at about 300 km. Further, it is the increase in the upper limit of the total-

reflection band that accompanies the bathymetry-induced increase in the waterborne limit that is the major cause of the comparatively small fall-off rate in the RANDI propagation at the larger source ranges.

The remaining band is the sediment-refraction band. This band extends from the upper limit of the waterborne band or the upper limit of the total-reflection band, depending on whether the sound-speed ratio is less than or greater than unity. As seen in the figure, the upper limit of the sediment-refraction band for the RANDI environment is significantly larger than that of the APL environment for ranges in excess of about 50 km. However, much of this difference is due to the presence of the total-reflection band in the RANDI environment. The actual widths of the sediment-refraction bands for the two environments differ by less than 10 modes over most of the range interval between 50 km and 1150 km. However, beyond 1150 km, the RANDI sediment-refraction band is from 20 to 40 modes larger than the APL sediment-refraction band. As noted in Section 3, the limits of the sediment-refraction band depend on the history of the mode attenuation integral (see Eq. (4)), and hence, on the history of the geoacoustic parameters and the sound speed in the sediment. The analysis of the "range-independent" track presented at the beginning of the section, suggests that the larger upper limit for the RANDI environment results from a combination of the larger sound-speed ratios, the larger densities, and the smaller interface attenuations.

4.3 Continental-Shelf Track

The environments for the continental-shelf track are illustrated in the water-column plots of Fig. 21 and the geoacoustic plots of Fig. 22 in the same format as the environment plots of Figs. 15 and 16.

As seen in Fig. 21, the water depth for the RANDI environment is nearly constant out to a range of about 300 km and then decreases gradually from about 5300 m to about 2500 m at a range of about 675 km. The depth then decreases more rapidly out to a range of about 753 km, where the shelf-break occurs at a depth of about 54 m. The depth continues to decrease over the next 36 km, reaching a minimum depth of about 7 m at a range of 789 km. The APL bathymetry is similar to the RANDI bathymetry, but a little less smooth.

The sound-speed field for the RANDI environment is independent of range out to about 500 km with the form of the sound speed profile at the site (Fig. 10). At 500 km there is a sharp transition that results from a dramatic decrease in the sound speed in the upper water column. At 725 km there is a second transition to a form that is similar to the array site profile. Beyond 725 km the sound speed varies slowly with range except for the bathymetry induced truncation depths. The APL sound-speed field shows no sharp transitions with range, but instead, varies gradually with range with a form similar to that at the array site. As such, it is similar to the RANDI environment except over the 226 km range interval, where the RANDI sound-speed field undergoes the transition.

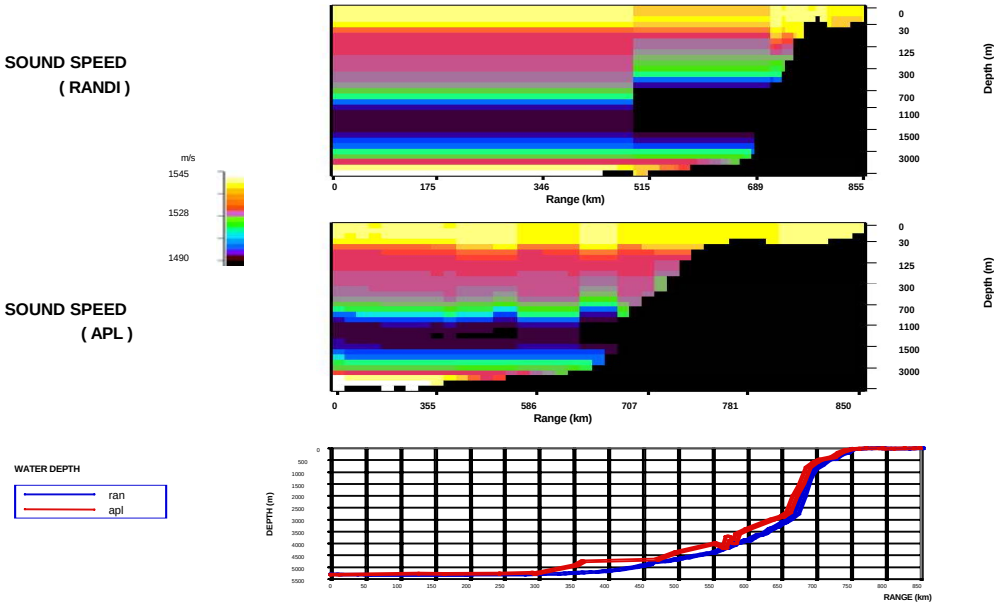

Fig. 21 — Sound speed and bathymetry comparisons for the Sargasso Sea shelf track: RANDI sound-speed field (top); APL sound-speed field (middle); water depth comparison (bottom)

The geoacoustic parameters for the continental-shelf track are shown in Fig. 22. For the RANDI environment, the values of the sound-speed ratio, the sediment density and the interface attenuation are identical to those at the site out to about 400 km. From 400 km to about 725 km, the sound-speed ratio decreases to a value below unity, the density decreases by almost a factor of two and the interface attenuation increases somewhat. Beyond 725 km, the RANDI parameters are the same as the site values, except for the sediment thickness which has a value of approximately 150 m. For the APL environment, the sound-speed ratio drops abruptly to a value that is even smaller than the site value, which is less than unity, and then remains constant out to a range of about 450 km. Over this interval, the density is essentially unchanged. From 750 km to the end of the track, the sound-speed ratio increases to values that vary around unity and the density increases slightly. The interface attenuation also drops abruptly at a short distance from the site, taking on values that are two orders of magnitude less that at the site, about 0.00015 dB / λ. The interface attenuation then increases significantly at a range of about 470 km.

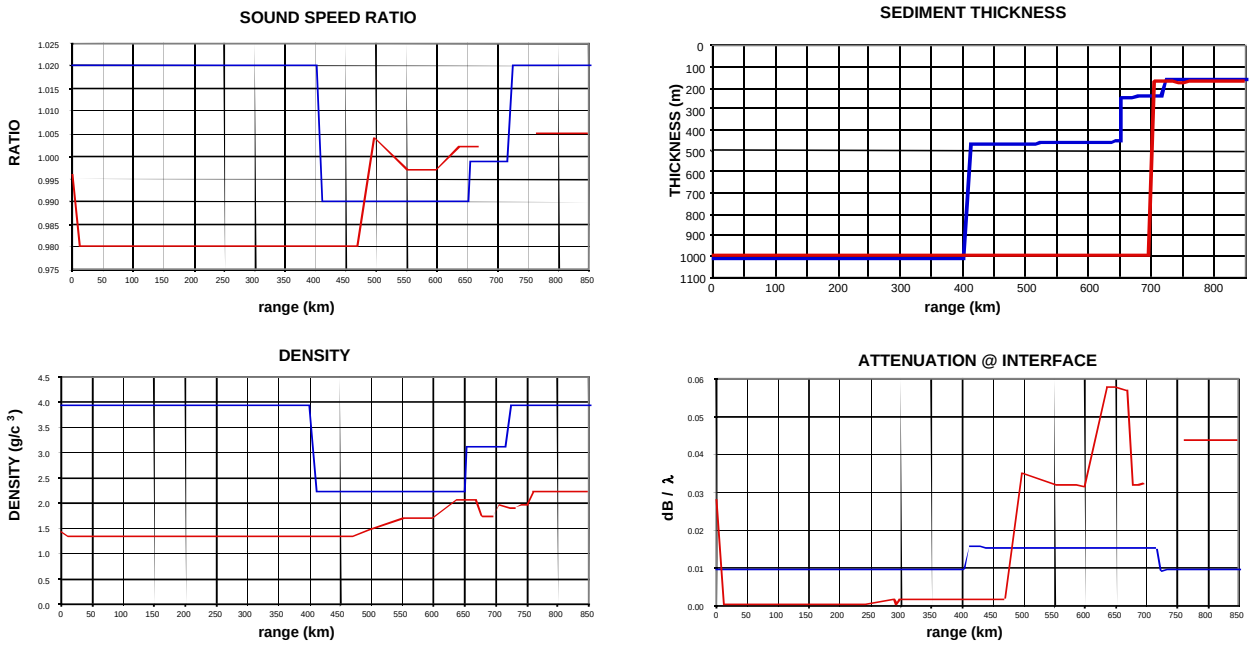

Fig. 22 — Geoacoustic parameters for the APL environment (red) and the RANDI environment (blue) on the Sargasso Sea shelf track: sound-speed ratio (top left); sediment thickness (top right); sediment density (lower left); interface attenuation (lower right)

Figure 23 shows the acoustic field and the vertical-arrival structure for the shelf track in the same format as Fig. 11. As seen in the left hand plots, both the RANDI field and the corresponding arrival structure are similar to those of the range-independent track over the first 500 km. The RANDI field has a range fall-off comparable to that in Fig. 11 and the arrival structure has the energy concentrated in elevation angle sectors similar to those in Fig. 11. This is not surprising since the environment is only weakly dependent on range over this interval. As the source range increases into the slope region, the received energy begins to fall off more slowly with range and the vertical separation in the arrival structure begins to decrease. At about 675 km., where the water depth has decreased to about 2500 m, there is a sharp increase in the received energy across the full water column and the vertical separation decreases dramatically. Beyond about 700 km, the level of the RANDI field falls off rapidly and the arrival structure collapses into a single mode. At about 750 km, the level of both the received field and the arrival structure has fallen below the plot scale.

Both the field and the arrival structure for the APL model are similar to those of the RANDI model out to a range of about 675 km. Unlike the RANDI model, neither the field nor the arrival structure for the APL model extends beyond about 700 km. This is consistent with the observation in Section 2 that there are no contributions to the APL noise directionality from sources located on or near the shelf-break.

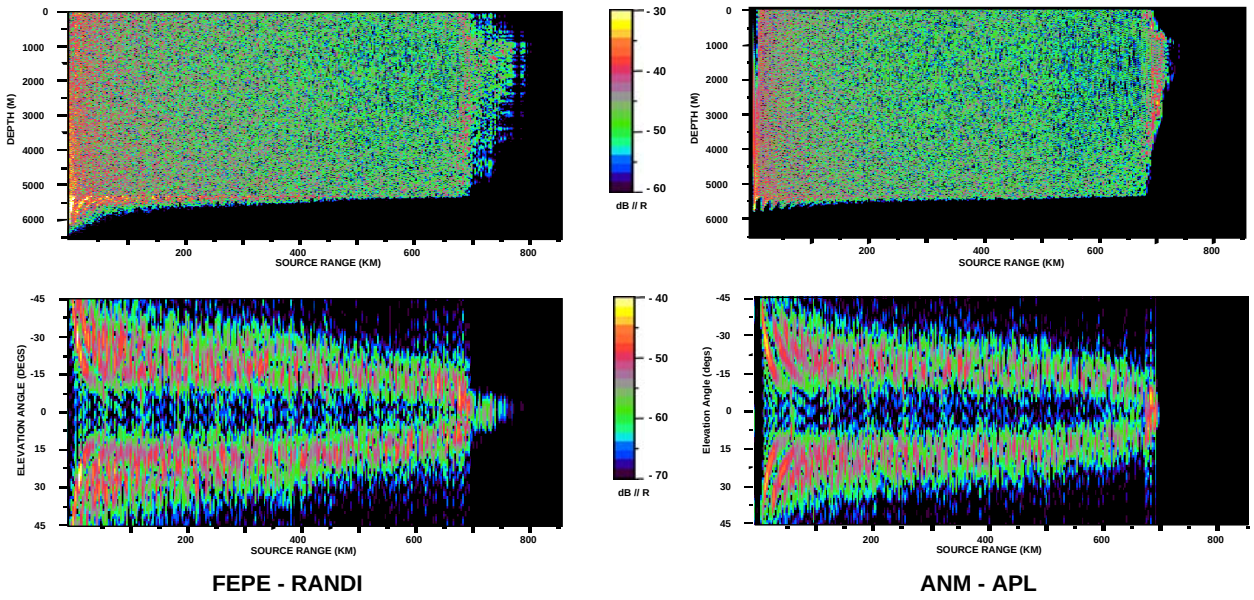

Fig. 23 — Propagation/environment acoustic field comparison for the Sargasso Sea site continental-shelf track: (left panels) FEPE propagation model / RANDI environment; (right panels) ANM propagation model / APL environment; (top panels) range-depth distribution of the acoustic field; (bottom panels) vertical-arrival structure vs. range

The propagation curve and the arrival structure comparisons are shown in Figs. 24 and 25, respectively. An inspection of the propagation/environment plot in Fig. 24 (top left), indicates that the RANDI energy exceeds the APL energy by less than a few dB for sources out to about 600 km and by less than about five dB for sources from 600 km out to about 675 km. At 675 km, the local maxima of the energy for the two models are essentially equal. For sources beyond 675 km, the APL energy falls off over 35 dB within a few km; the RANDI energy falls off much more gradually. The environment-only and the propagation-only comparison plots indicate that the small difference in the RANDI and the APL propagation for sources out to 500 km is primarily due to the environment. The small difference from 500 to 675 km and the dramatic difference for source ranges greater than about 700 km are primarily due to the difference in propagation models. As with the other tracks, the similarity in the red and the black propagation curves in the ANM model comparison plot (bottom right) indicates that the difference in the ANM propagation models is not a factor.

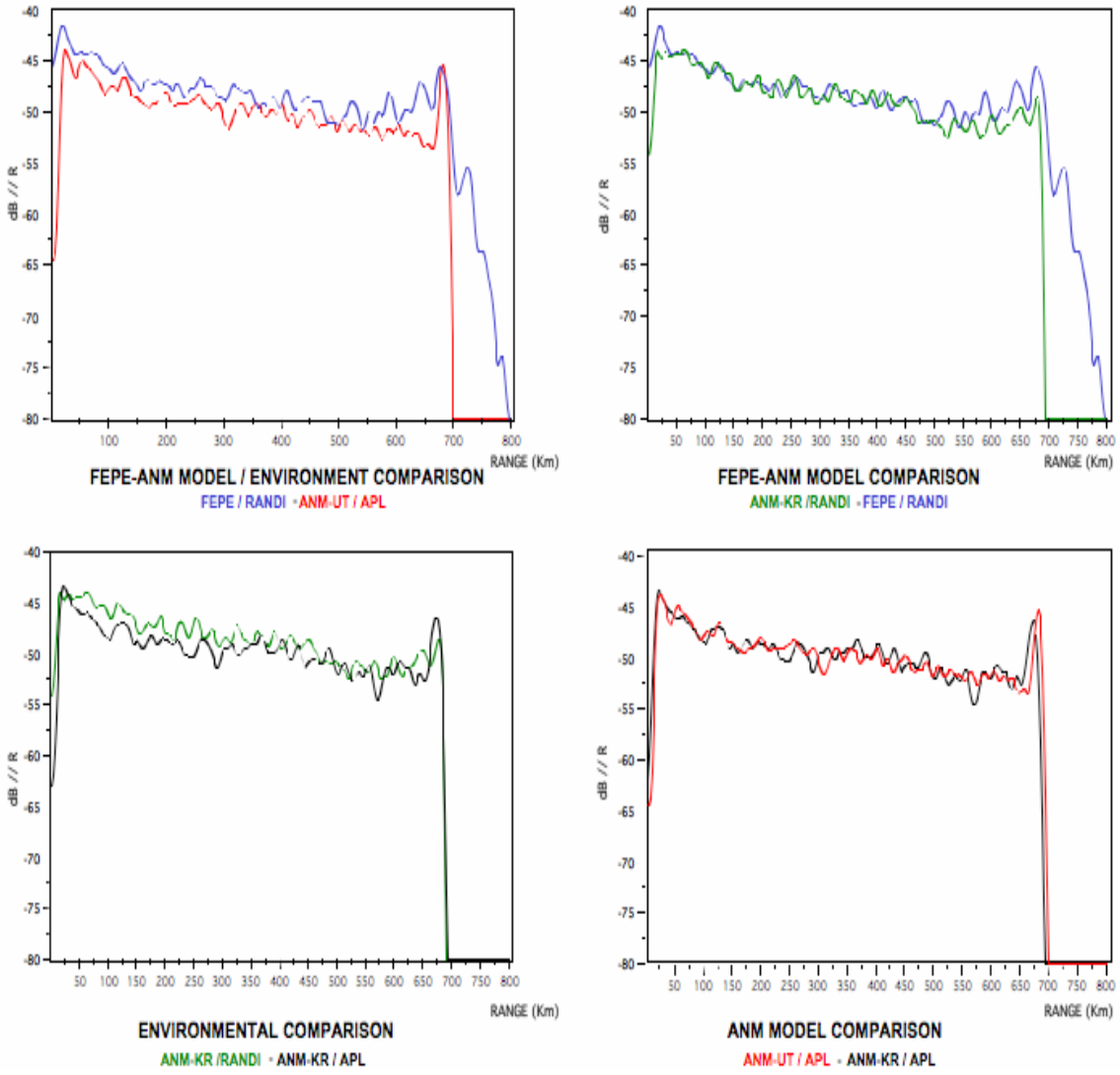

Fig. 24 — Depth-averaged propagation curves for the Sargasso Sea continental-shelf track: propagation/environment comparison (top left); propagation-only comparison (top right); environment-only comparison (bottom left); ANM model comparison (bottom right)

The vertical-arrival structure plots of Fig. 25 show three source range averages, a 500 to 650 km average (solid curves), a 673 to 695 km average (dashed lines), and a 697 to 740 km average (dotted lines). As noted above, only the RANDI field has significant energy in the 697 to 740 km interval, and hence, only the RANDI arrival structure for this interval appears in the propagation/environment and the propagation-only plots.

Consider the 500-650 km vertical-arrival structure averages first. The propagation/environment plot indicates that the RANDI arrival structure is about one to two dB greater than that of APL with a slightly smaller separation. As for the deep-water track, the propagation plot shows that the separation for the ANM model is greater than that for the FEPE model and the environment-only comparison plot shows that the separation for the RANDI environment is greater than the separation for the APL environment. The FEPE levels are greater than the ANM levels.

Next consider the 673 to 695 km arrival structure average shown by the dashed lines. The propagation/environment plot shows a unimodal structure for the APL arrival structure and the remnants

of a bimodal structure for the RANDI arrival structure. The difference in the curves in the propagation-only plot indicates that the unimodal structure is an artifact of the adiabatic-normal-mode approximation. The environment-only comparison plots show that, at least for an ANM propagation model, the APL environment results in considerably more energy than the RANDI environment over the 673 to 695 km range interval. Taken together, these observations indicate that the unimodal structure in the APL curve is a consequence of the ANM approximation and the larger energy is a consequence of environmental differences.

Finally, note that for the 697 to 740 km interval, the RANDI model vertical-arrival structure is unimodal as expected for downslope propagation.

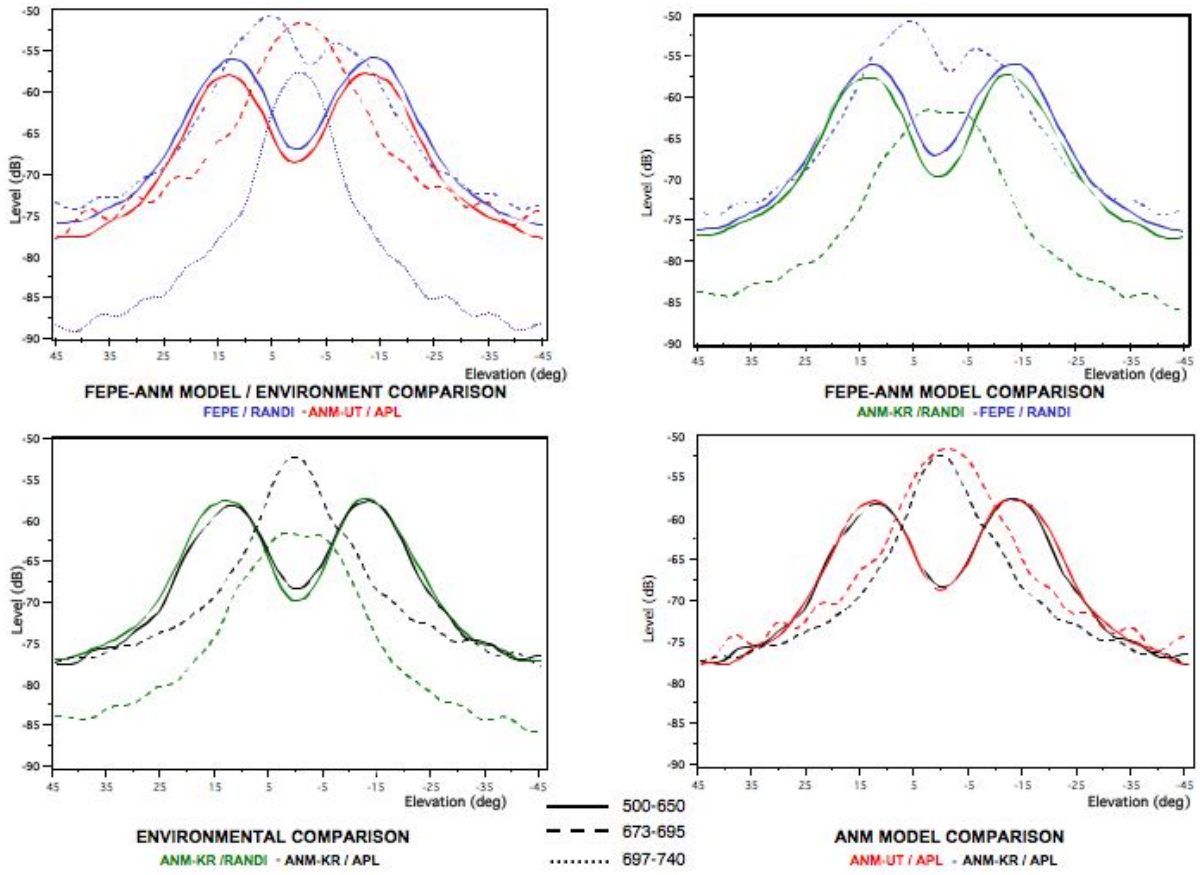

Fig. 25 — Range-averaged vertical-arrival structure for the Sargasso Sea continental-shelf track: propagation/environment comparison (top left); propagation-only comparison (top right); environment-only comparison (bottom left); ANM model comparison (bottom right)

The previous results indicate that the FEPE field is significant for source ranges up to and on to the shelf; whereas, the ANM field is not significant for these source ranges. To aid in the interpretation of this result, we have computed the field as a function of receiver range for a fixed source position using the FEPE propagation model and the ANM-KRAKEN model. The RANDI environment is used in both cases. As such, the results correspond to the blue and to the green cases. The results are shown in Fig. 26 for four source ranges, 675 km, 700 km, 725 km, and 750 km. The FEPE results are plotted on the left and the ANM-KRAKEN result are plotted on the right. The depth at the source for the four source ranges are

2510 m, 855 m, 466 m and 54 m, respectively. The ANM-KRAKEN plot for 750 km is not shown since the levels are substantially less than the dynamic range for all but the first few kilometers.

The FEPE plots show that as the source moves up the slope and onto the shelf, the energy becomes concentrated in a depth interval that is centered below the 48 to 252 m depth interval corresponding to the array. As the source range increases, the width of this depth interval decreases, accounting for the decrease in the energy incident on the array. Note the sharp change in the width of the interval associated with the sharp change in the sound speed. The ANM-KRAKEN plots also show that the energy becomes concentrated in depth as the source range increases. However, the structure of the field differs significantly from that of the FEPE field, as expected, since there is no mechanism for transferring energy from the low order modes to the high order modes.

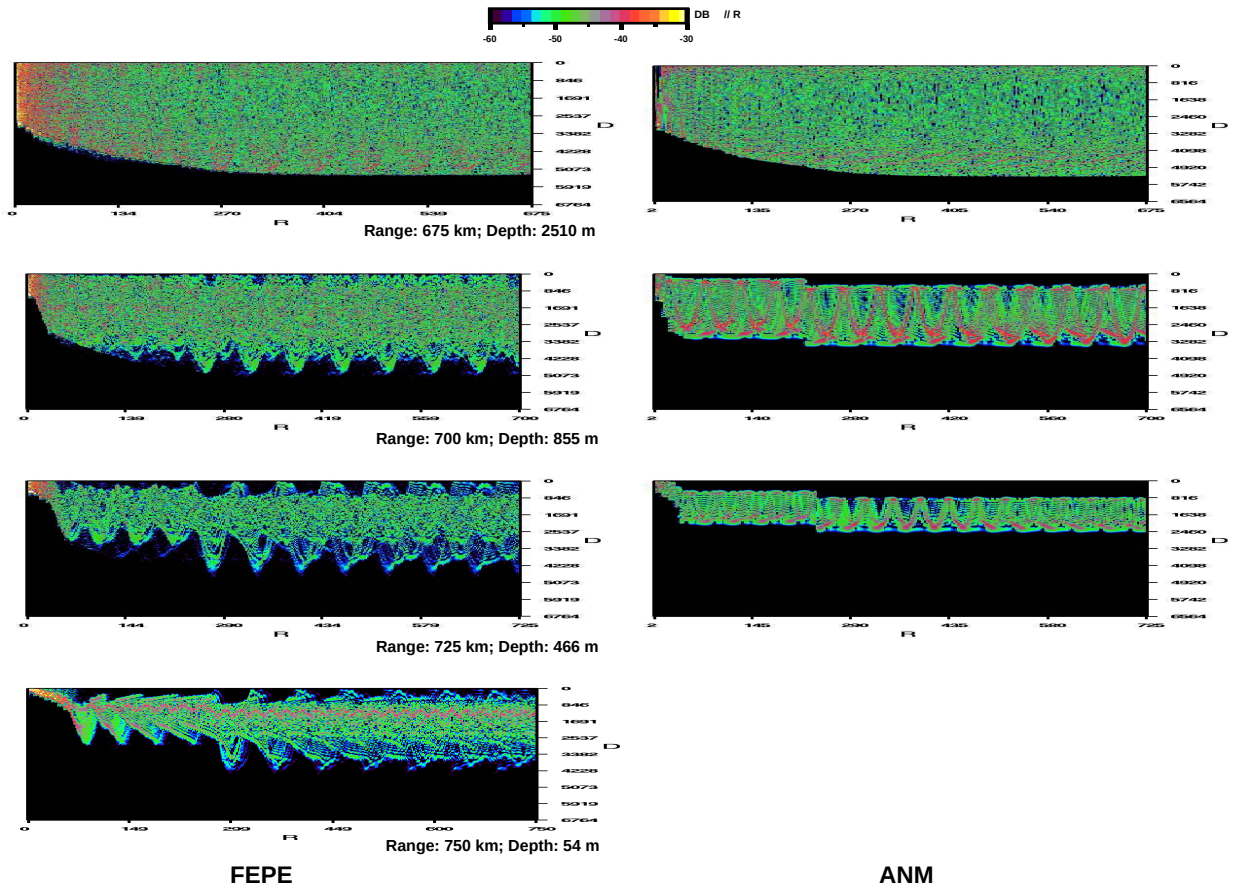

Fig. 26 — Acoustic field for the Sargasso Sea shelf track for selected source ranges: FEPE model (left); KRAKEN Adiabatic-normal-mode model (right)

To interpret the propagation results for the continental-shelf track, we have plotted the modal components for the two environments in Fig. 27. As with the deep-water track, the array-mode functions, shown at the top of Fig. 25, are the same as those for the range-independent track. As noted above, these two array-mode functions are essentially the same over the depth interval spanned by the receiver array. Thus, the impact of the difference in the two environments on the propagation is the result of the difference in the source-mode functions. On the other hand, the failure of the adiabatic approximation for the near-slope/on-slope source ranges is a consequence of the relationship between the source-mode function and the array-mode function. This can be seen in the plots for either environment.

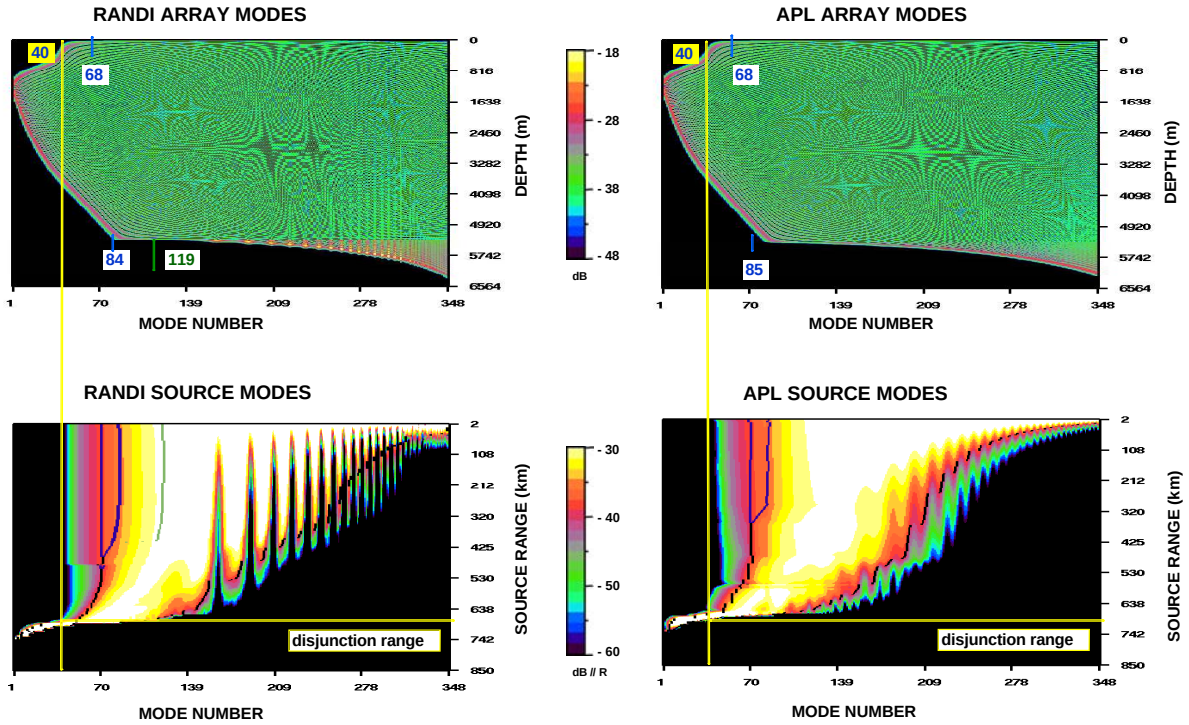

Fig. 27 — Mode function components for the RANDI and the APL Sargasso Sea continental-shelf track: (top panels) array-mode functions; (bottom panels) source-mode functions; (left panels) RANDI components; (right panels) APL components

We consider first the impact of the environmental differences. As seen in the environmental-only comparison plot of Fig. 24, the energy for the RANDI environment is only about 2 dB higher than the energy for the APL environment out to about 600 km. Over this range interval, the RANDI source-mode function is similar to that of the RANDI range-independent track, as expected, since the environment for the tracks are similar over this range interval. For the APL environment, the lower limit of the modal band is similar to that of the range-independent track out to a range of about 300 km, where it decreases somewhat due to the decrease in the water depth. However, for ranges out to about 475 km, the upper limit of the modal band is considerably larger than that of the range-independent track, even though the sound-speed ratio and the density are similar to those on the range-independent track. The difference in the upper limits for the two tracks is due to the difference in the attenuation. For the range-independent track, the interface attenuation is 0.0281dB/λ; whereas, for the continental slope track, the interface attenuation is two orders of magnitude less. Thus, even though the APL environment does not have a critical angle and the reflection coefficient is smaller than the RANDI environment at the larger grazing angles, the total energy is only a few dB less since the attenuation in the refracted energy is negligible.

We now consider the adiabatic assumption limitation. To this end, recall that the modal representation for the field at a depth z and a range r_s is obtained as the coherent summation of the product of the complex array-mode function, $\varphi_m^a(z) = \varphi_m(z, r_s = 0)$ at depth z and the complex source-mode function $\varphi_m(z_s, r_s)$ at range r_s. For a nominal array depth of 150 m (the midpoint of the 50 to 250 m depth interval assumed in the computations), the array-mode function is significant only for modes greater than about 40. This limit is plotted as the white line in the two source-mode function plots. Now, as seen in the source-mode function plots, as the source moves up the slope and the water depth decreases, the source-mode function becomes negligible for the larger mode numbers. In particular, there is an upper limit of the modes for which the source-mode function is significant and that limit decreases as the source range increases, and hence, the water depth decreases. The intersection of the array mode lower limit (the white

line) with the source mode upper limit occurs at a source range of about 697 km for the RANDI environment and about 690 km for the APL environment. For ranges greater than these intersection ranges, the field is negligible because the complex product of the array-mode function and the source-mode function is negligible. We refer to this phenomenon as mode-set-disjunction since the set of modes that contain significant energy at the array is disjoint from the set of modes observed by the array. The range at which the mode sets first become disjoint is referred to as the disjunction range.

To provide an explicit illustration of the deficiencies in the ANM model, we have computed the source-mode function for the FEPE generated field directly from Eq. (1) using the orthonormal properties of the array-mode functions. The result is shown in Fig. 28 along with the ANM source-mode function. Both source-mode functions are obtained for the RANDI environment. A comparison of the source-mode functions indicates that the FEPE source-mode function (shown on the right) is similar to the ANM source-mode function (shown on the left) out to a range of about 500 km, where the sharp transition in the sound speed profile occurs. In the interval from about 500 km to about 650 km, there is a modest redistribution of the modal energy in the FEPE source-mode function due to the sound speed transition and a small increase in the energy due to the decreasing bathymetry. It is this increase that accounts for the larger energy in the FEPE propagation curve on the top right of Fig. 24. However, as expected, the major difference in the source-mode functions occurs for ranges beyond the minimum disjunction range, where the FEPE function shows energy for modes greater than the cut-off mode. This energy results from the conversion of low mode energy to high mode energy high in downslope propagation.

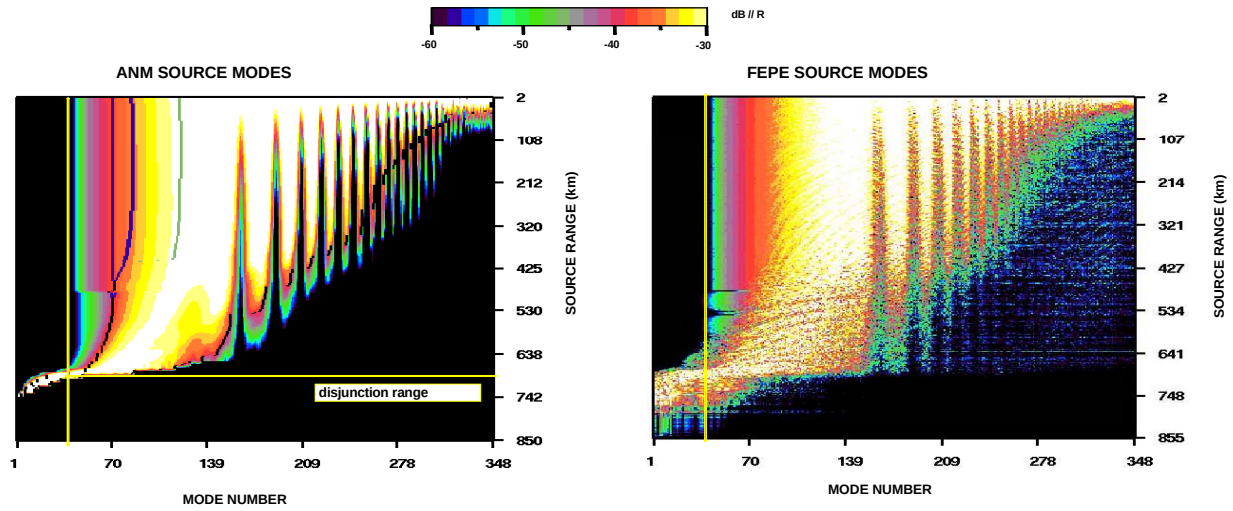

Fig. 28 — Source-mode functions for the Sargasso Sea shelf track with the RANDI environment: ANM source-mode function (left); FEPE source-mode function (right)

5. GULF OF ALASKA PROPAGATION COMPARISON

This section presents the analysis of the propagation components of the two noise models for the Gulf of Alaska. As for the Sargasso Sea, the analysis is obtained though three comparisons, (a propagation/environment comparison, a propagation-only comparison, and an environment-only comparison) conducted on three tracks (a range-independent track, a deep-water track, and a continental-shelf track).

5.1 Range-Independent Track

The environments for the 500 km range-independent track are obtained from the environmental components of the two noise models at a location about 600 nmi south of Anchorage, Alaska in the Gulf of Alaska. The depth profiles describing the two environments are shown in Fig. 29 in the same format as Fig. 10; parameters of these environments are presented in Table B1 of Appendix B in the same format as Table A1 of Appendix A. Note in Fig. 29 that, unlike the Sargasso Sea, the sound speed profiles for the two environments are different over the full water column with the largest differences of between 1 and 2 m/s occurring between 75 and 200 m. Furthermore, unlike the Sargasso Sea, neither profile has a sound-speed ratio greater than unity.

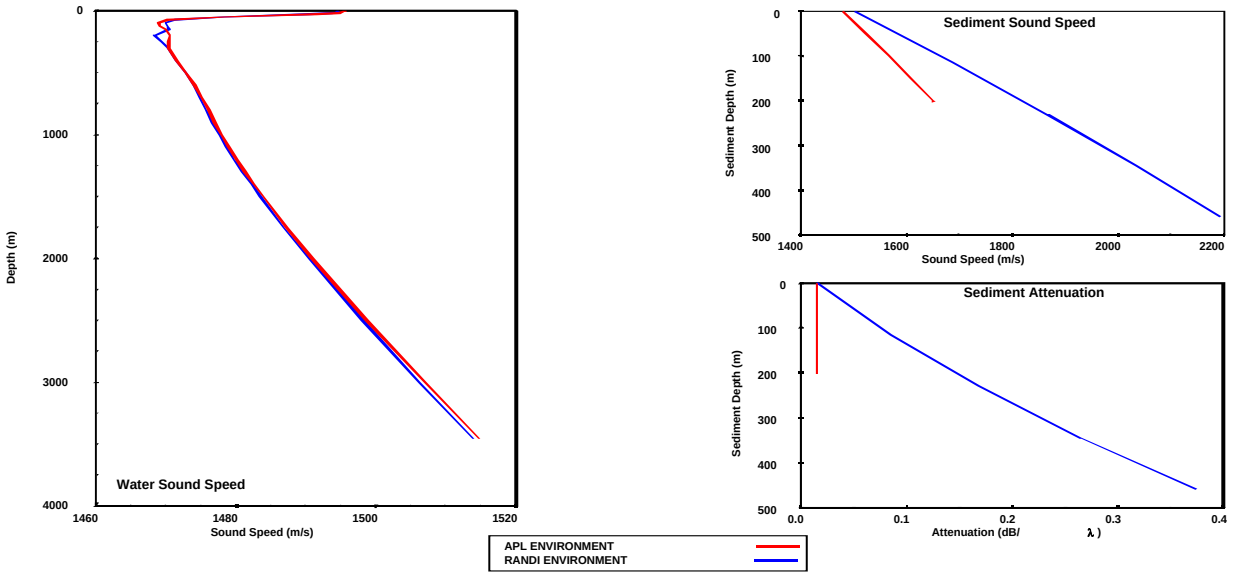

Fig. 29 — Environment profile comparisons at the Gulf of Alaska site for the APL environment (red) and the RANDI environment (blue): water-column sound speed profile (left); sediment compressional speed profile (top right); sediment attenuation profile (bottom right)

The acoustic field and the vertical-arrival structure for the two environments are shown in Fig. 30. An inspection of the acoustic field for both models (top plots) indicates that, as for the Sargasso Sea, the sediment-interacting energy is a major component of the field. Note, however, that, unlike the Sargasso Sea, the convergence zone structure can be seen in the APL acoustic field at the longer ranges.

The vertical-arrival structure plots for the two models are similar to those for the Sargasso Sea (see Fig. 10). The minimum elevation angle for the energy sectors in both plots is about $\pm 10°$ as was the case in the Sargasso Sea. However, in the Gulf of Alaska, this angle corresponds to the minimum arrival angle for the waterborne energy, $\theta_{w,}$ in Table B1, rather than the minimum angle for sediment-interacting energy, θ_{sw}. The difference is due to that fact that for the Gulf of Alaska, the waterborne energy, which occurs for smaller angles, is distributed in range; whereas, for the Sargasso Sea the waterborne energy occurs only at the regular spaced convergence zone ranges. Thus, even though θ_w and θ_{sw} are larger for the Gulf of Alaska, the minimum separation is comparable because it is the waterborne energy that determines the minimum separation. As for the Sargasso Sea, the maximum angle of the sediment-interacting energy is over $\pm 45°$ at about 5 km.

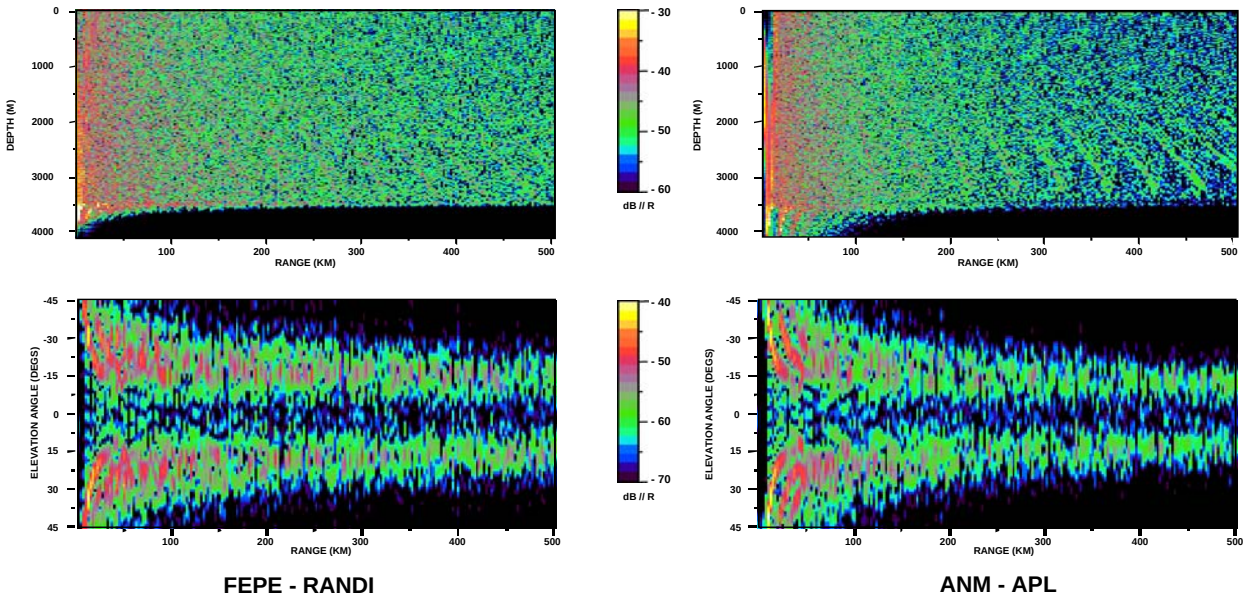

Fig. 30 — Propagation/environment acoustic field comparisons for the Gulf of Alaska range-independent track: (left panels) FEPE propagation model / RANDI environment; (right panels) ANM propagation model / APL environment; (top panels) range-depth distribution of the acoustic field; (bottom panels) vertical-arrival structure vs. range

The depth-averaged propagation curves for the different propagation components are shown in Fig. 31. An inspection of these curves indicates that, as for the Sargasso Sea, the difference in the two propagation/environment curves is due almost entirely to the environmental differences. However, the difference in the propagation loss at the end of the 500 km range interval is only about 3 dB compared to 7 dB for the Sargasso Sea.

The normal mode components for the range-independent track are shown in Fig. 32. As for the Sargasso Sea, the array-mode functions for the two environments (top panels) are similar to one another, except in the sediment, where the energy in the RANDI array modes is appreciably larger than that for the APL array modes. The Gulf of Alaska array modes differ from those for the Sargasso Sea in the shape of the depth-mode envelope. This is a consequence of the difference in the sound speed profiles for the two areas.

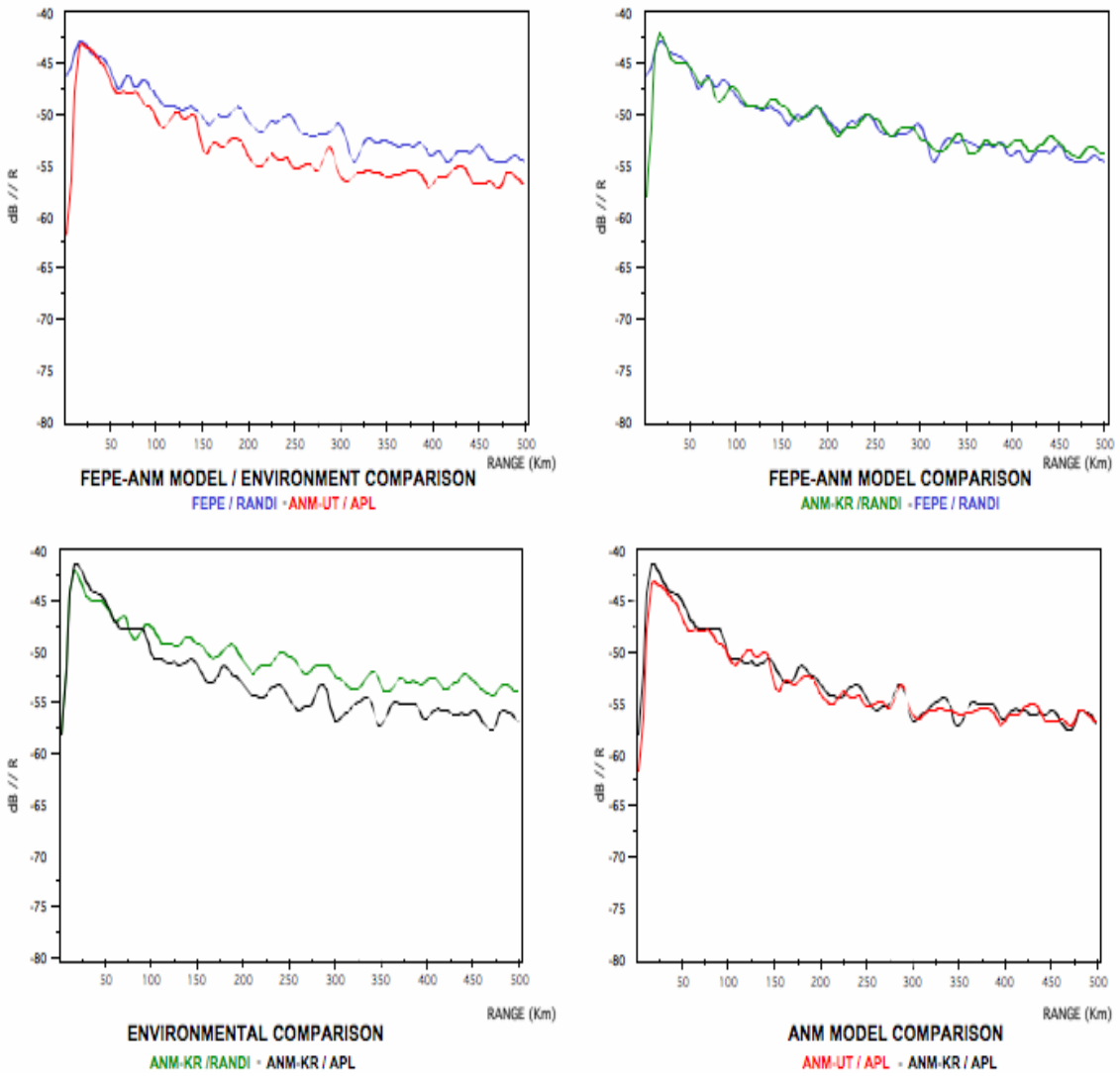

Fig. 31 — Depth-averaged propagation curves for the Gulf of Alaska range-independent track: propagation/ environment comparison (top left); propagation-only comparison (top right); environment-only comparison (bottom left); ANM model comparison (bottom right)

The source-mode functions for the Gulf of Alaska (bottom plots) have a different modal decomposition than those for the Sargasso Sea, range-independent track. As for the Sargasso Sea, both the lower and the upper limits for the waterborne modes are essentially the same for the two environments since the sound speeds at the source depth and at the water bottom are essentially the same. For the Gulf of Alaska, the lower limits of the waterborne band are 24 for the RANDI environment and 25 for the APL environment compared to 68 for the Sargasso Sea. This difference is a consequence of the colder water in the Gulf of Alaska, and hence, the lower sound speeds at the 5-m source depth. The waterborne upper limit is 48 for both environments for the Gulf of Alaska, compared to about 84 for the Sargasso Sea. This is due to the shallower water depth in the Gulf of Alaska. For the Gulf of Alaska, there is no total-reflection band for either environment since the sound-speed ratio is less than unity. Accordingly, the upper limit of the waterborne band is the lower limit for the sediment-refraction band. At 500 km, the upper mode limits of the sediment-refraction band for the RANDI and APL environments are about 108 and 69, respectively, whereas the corresponding upper limits for the Sargasso Sea are about 230 and 135, respectively. Thus, the band of modes that carry the sediment-interacting energy (the difference between the upper limit and the waterborne upper limit), is smaller for the Gulf of Alaska than for the Sargasso

Sea, and the band of modes that carry the waterborne energy (the difference between the waterborne upper limit and the lower limit) is larger for the Gulf of Alaska. It is this fact that accounts for the difference in the proportion of waterborne to sediment-interacting energy in the two areas. Finally, note that the difference in the extent of the waterborne band between the different environments in the Gulf of Alaska is much smaller than in the Sargasso Sea. It is this fact that accounts for the smaller difference in the long-range propagation loss between the two environments in the Gulf of Alaska.

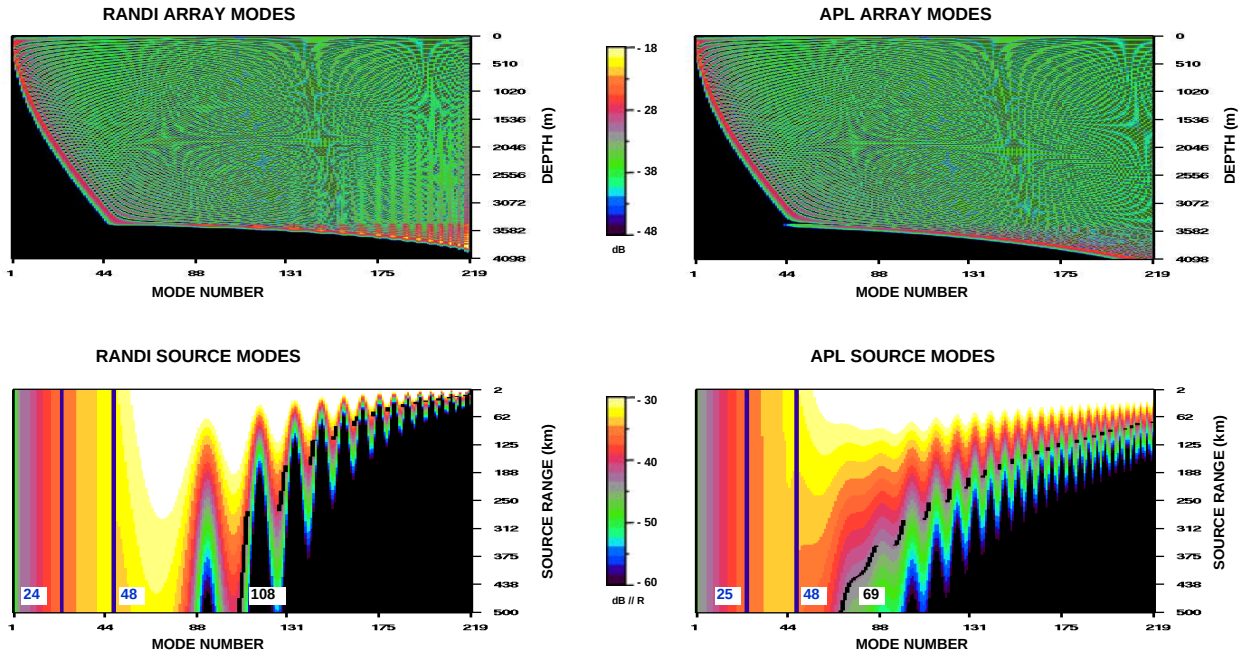

Fig. 32 — Mode function components for the RANDI and the APL Gulf of Alaska range-independent track: (top panels) array-mode functions; (bottom panels) source-mode functions; (left panels) RANDI components; (right panels) APL components

5.2 Deep-Water Track

The two environments for the deep-water track are illustrated in the water-column plots of Fig. 33 and the geoacoustic plots of Fig. 34 in the same format as that for the range-dependent tracks in the Sargasso Sea.

As seen in Fig. 33, the APL sound speed is similar to the RANDI sound speed along the full length of the track. They both show a deepening of the sound-speed channel due to the increase in the water temperature in the upper water column as the range increases, and hence, as the latitude decreases. The sharp increase in the upper water-column sound speed at a range of about 1600 km occurs at the Sub-Arctic Transition Zone. Finally, the bathymetry for both environments show a small seamount at about 150 km followed by a decrease of almost 2000 m along the 2000 km track and a number of even smaller seamounts in the last half of the track. As for the Sargasso Sea deep-water track, the APL bathymetry has a slightly smaller variation.

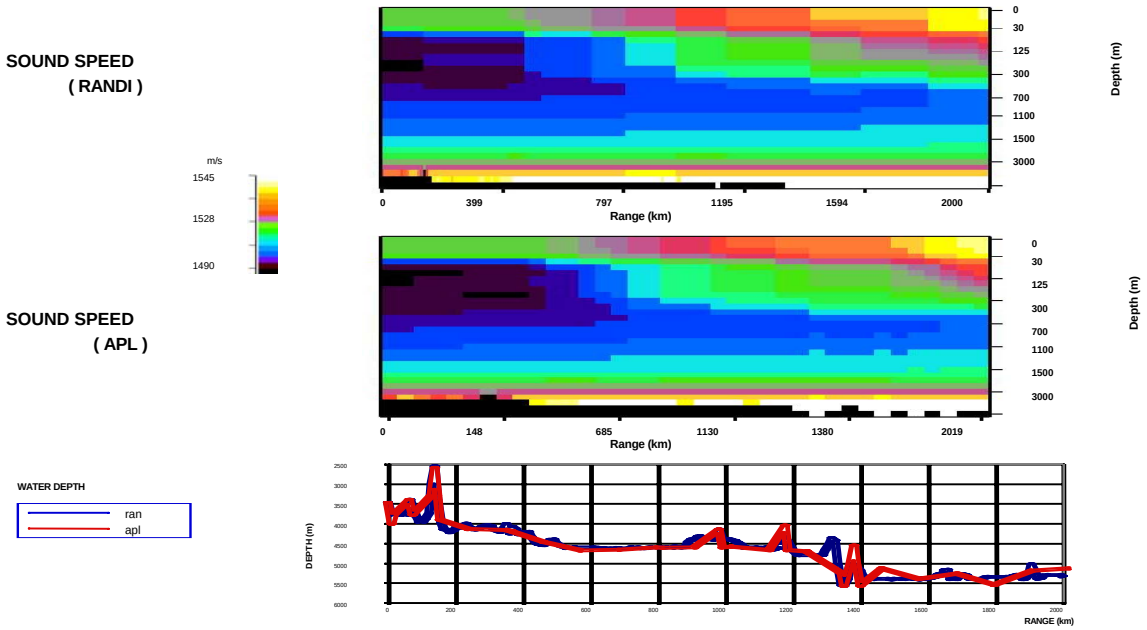

Fig. 33 — Sound speed and bathymetry comparisons for the Gulf of Alaska deep-water track: RANDI sound-speed field (top); APL sound-speed field (middle); water depth comparison (bottom)

The geoacoustic parameters are plotted in Fig. 34. Excluding the sediment thickness, the RANDI sediment parameters are roughly the same as those at the site along the full length of the track. The RANDI sediment density and interface attenuation are essentially unchanged and the RANDI sound-speed ratio is the same out to a range of 800 km, where it then decreases somewhat from 0.990 to 0.976. The RANDI sediment thickness exceeds 450 m out to a range of about 800 m, where it drops to about 80 meters along the remainder of the track. In contrast, the APL parameters show a significant change in both the sound-speed ratio and the sediment density immediately after the site. The sound-speed ratio increases from 0.976 at the site to 0.997 and then remains constant out to a range of about 375 km, where it then increases to a value slightly greater than unity (1.001) out to a range of 800 km. It then decreases to the value at the site for the rest of the deep-water track. Similarly, the density increases from 1.5 at the site to 3.6 and then remains constant out to about 275 km, where it decreases to the value at the site for the remainder of the track. The interface attenuation shows a modest variation along the track that is similar to that of the RANDI interface attenuation. The APL sediment thickness (without the 1000-m extension) varies between 80 and 200 meters along the full length of the track.

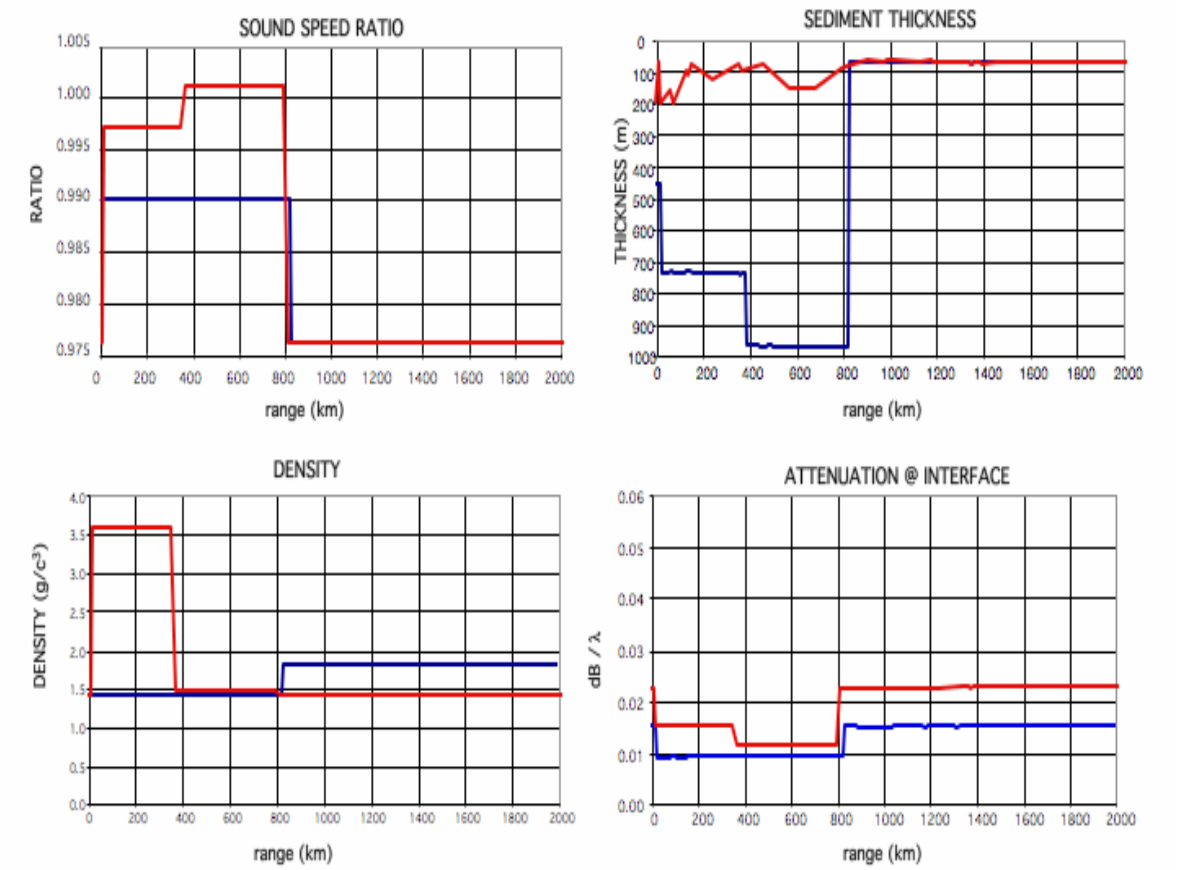

Fig. 34 — Geoacoustic parameters for the APL environment (red) and the RANDI environment (blue) on Gulf of Alaska deep-water track: sound-speed ratio (top left); sediment thickness (top right); sediment density (lower left); interface attenuation (lower right)

In Fig. 35, we have plotted the acoustic field and the vertical-arrival structure for the deep-water track. The field plots for both environments show a significant decrease in the energy starting at about 1000 km. This decrease, which is more pronounced for the RANDI environment, is also evident in the arrival structure plots. Also note that the arrival structure plots show an increase in the elevation angle separation with range.

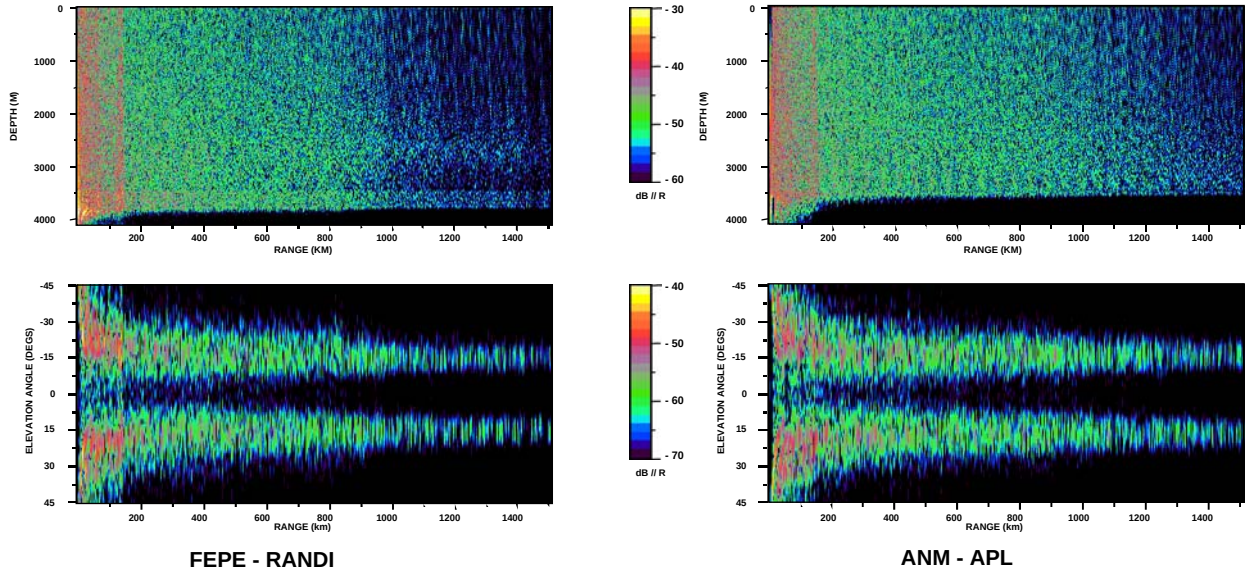

Fig. 35 — Propagation/environment acoustic field comparison for the Gulf of Alaska deep-water track: (left panels) FEPE propagation model / RANDI environment; (right panels) ANM propagation model / APL environment; (top panels) range-depth distribution of the acoustic field; (bottom panels) vertical-arrival structure vs. range

The propagation comparisons for the deep-water track are plotted in Fig. 36. As seen in the propagation/environment plot (top left), the energy for both models drops off abruptly at about 150 km, then falls off gradually out to about 900 km and then falls off more rapidly out to the end of the track. The two curves are comparable out to about 800 km, where the RANDI model energy falls below the APL model energy by a few dB for much of the remainder of the track. Note that at the end of the track, the energy in both curves is comparable to that of the APL model propagation curve for the deep-water track in the Sargasso Sea, which is about 8 dB less than the deep-water, Sargasso Sea RANDI model curve. The propagation-only plot (top right) indicates that the adiabatic approximation underestimates the energy by one to two dB in the interval from 150 km to 800 km and overestimates the peaks in the energy by a few dB in the interval from 1000 km to 1500 km. The environment-only plot (lower left) indicates that the RANDI environment results in a few dB less energy than the APL environment from about 150 km to the end of the track. Thus, in the interval from 150 km to about 800 km, the decrease in the energy due to the adiabatic approximation is compensated for by the increase in the energy due to the APL environment to produce the near comparability in the propagation/environment curves over this range interval. The small difference in the propagation/environment curves over the last half of the range interval results because the larger energy in the APL environment propagation curve is not compensated for by the smaller energy in the ANM propagation curve.

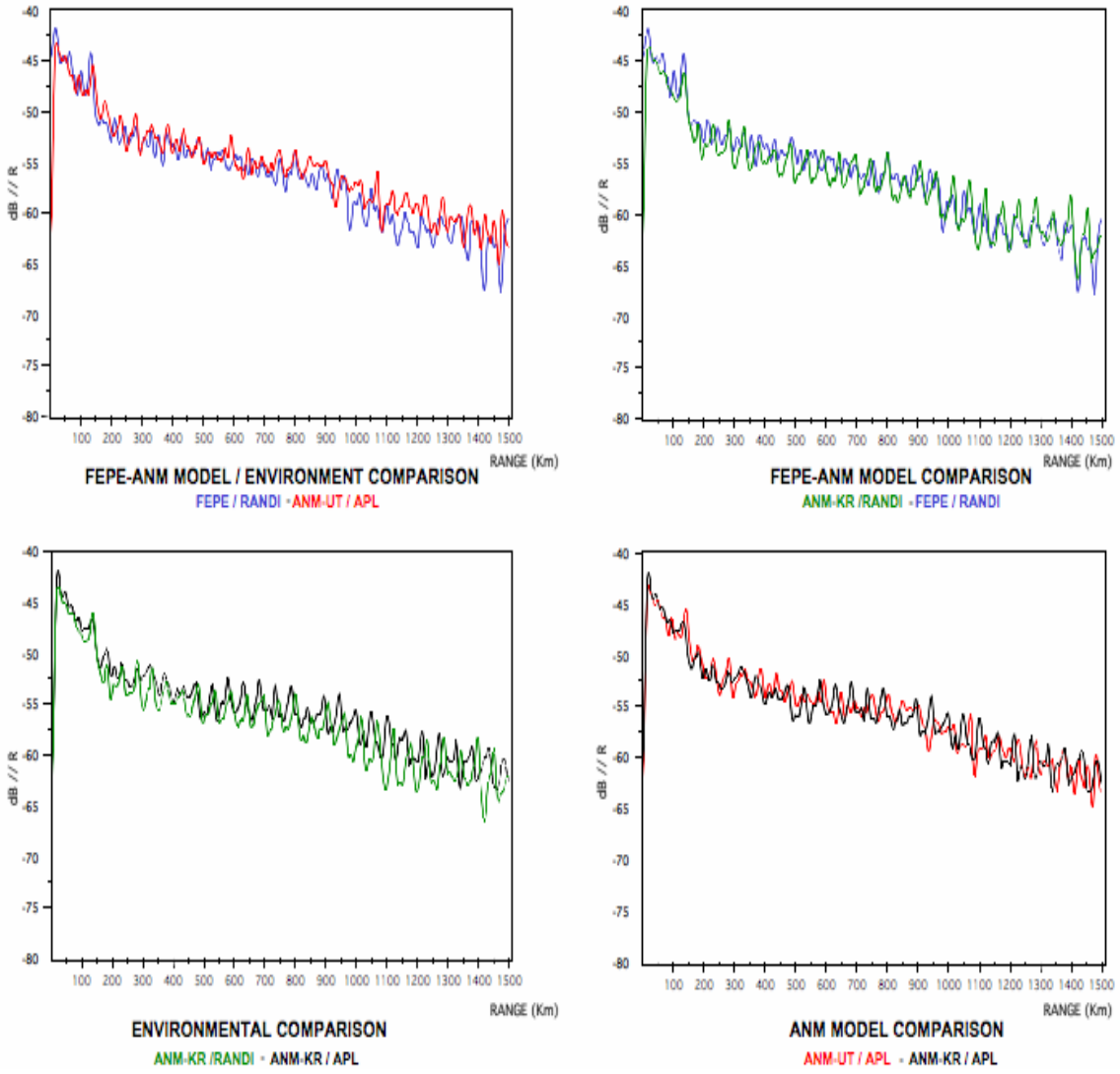

Fig. 36 — Depth-averaged propagation curves for the Gulf of Alaska deep-water track: propagation/environment comparison (top left); propagation-only comparison (top right); environment-only comparison (bottom left); ANM model comparison (bottom right)

The range-averaged arrival structure plots for the different comparisons are shown in Fig. 37. The averaging interval is 1000 to 1400 km. An inspection of the propagation/environment plot (upper left) indicates that although the overall energy in the arrival structure for the APL model is slightly greater than for the RANDI model, the depth of the notch for the two models is comparable. Also note that the separation between the peaks in the arrival structure is somewhat larger for the APL model than for the RANDI model. As discussed above, the slight difference in the level for this range interval can be attributed to the increase in the energy due to the adiabatic approximation. The increase in the peak separation appears to be caused by a small increase due to the adiabatic approximation and a small increase due to environmental differences.

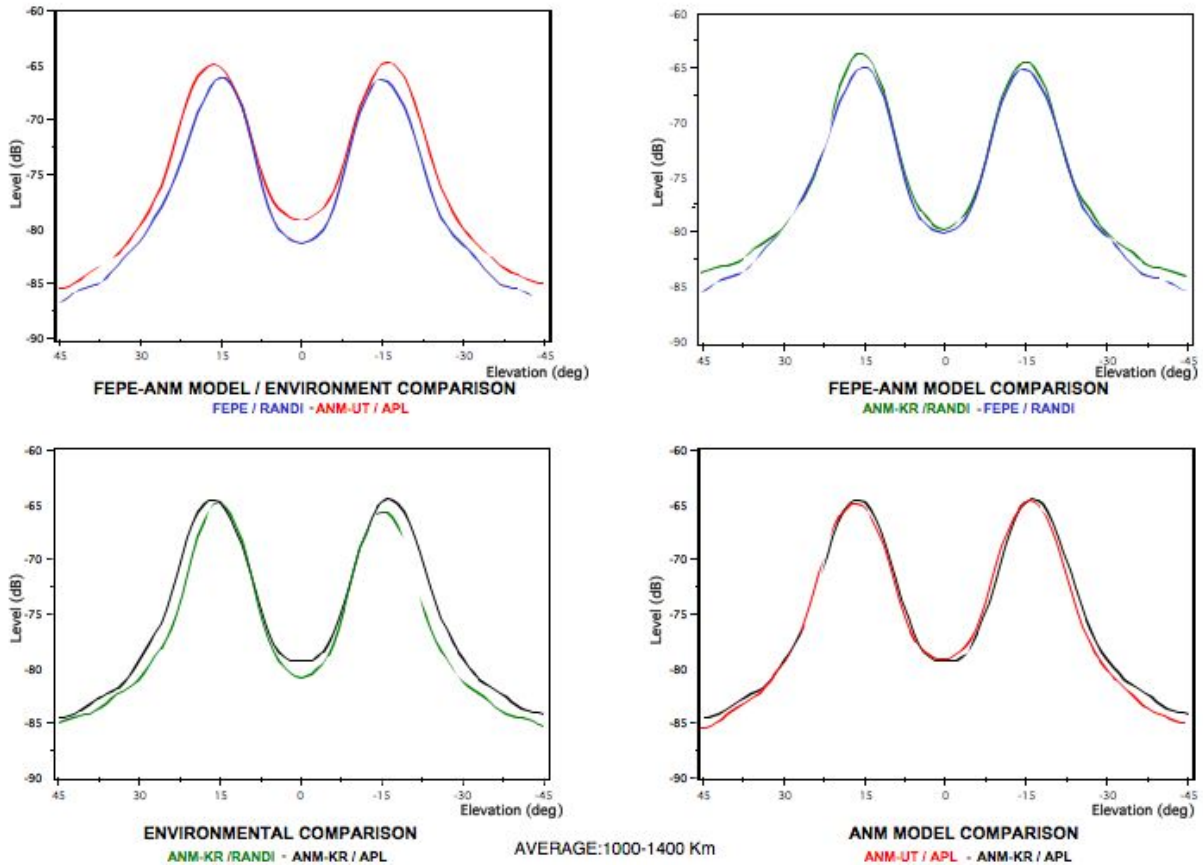

Fig. 37 — Range-averaged vertical-arrival structure for the Gulf of Alaska deep-water track: propagation/environment comparison (top left); propagation-only comparison (top right); environment-only comparison (bottom left); ANM model comparison (bottom right)

The mode function plots for the deep-water track are shown in Fig. 38. As with the other range-dependent tracks, the array-mode functions, shown at the top of Fig. 38, are the same as those for the range-independent track.

The mode-band decomposition for the two environments is as follows. For the waterborne band, both the lower limits and the upper limits for the two environments are comparable since the near surface sound speeds and the bathymetries are comparable. The lower limits increase with range from about 24 at the site to about 55 at the end of the 1500 km interval due to the increase in the near surface sound speed. The upper limits vary around the array site value of about 48 out to about 150 km, where there is a sharp decrease in the limit and an increase in the energy in the source-mode function due to the seamount at 150 km. The upper limits then increase with range out to values in the low nineties as the water depth increases with range.

The only total-reflection band occurs for the APL environment between about 390 km and about 800 km. The small width of this band, only about two modes, is due to the small value of the sound-speed ratio (1.001). Excluding this case, the lower limits of the sediment-refraction band are the upper limits of the waterborne band, which are essentially the same for both environments.

Finally, the upper limits of the sediment-refraction band for both environments decrease dramatically with range out to about 150 km. At 150 km, the source-mode functions for both environments show a sharp decrease in level that follows the sharp increase in the waterborne band levels associated with the

seamount at 150 km. This results because much of the energy in the sediment-refracted modes does not propagate beyond the seamount to the array site. From 150 km to about 410 km, the upper limit for the RANDI environment falls off slowly with source range and then from 420 km to about 800 km, the upper mode limit remains almost constant with range. This is due to the conversion of sediment-refracted modes to waterborne modes resulting from the bathymetry-induced increase in the upper limit of the waterborne band. (This also occurred in the deep-water track in the Sargasso Sea.) Between about 800 km and 1000 km, the upper limit for the RANDI environment decreases sharply and then levels off out to a range of about 1300 km, where it merges with the upper limit of the waterborne band as the sediment-refracted energy becomes negligible. The upper limit for the APL environment exhibits a similar behavior over the 150 km to 980 km range interval, except that the decrease in the energy with range following the seamount is even less than the decrease for the RANDI environment. This difference can be attributed to the difference in the reflection coefficients that results from the difference in the sound-speed ratios and the densities out to 410 km. It is this difference that accounts for the slightly larger energy values in the APL environment propagation curve.

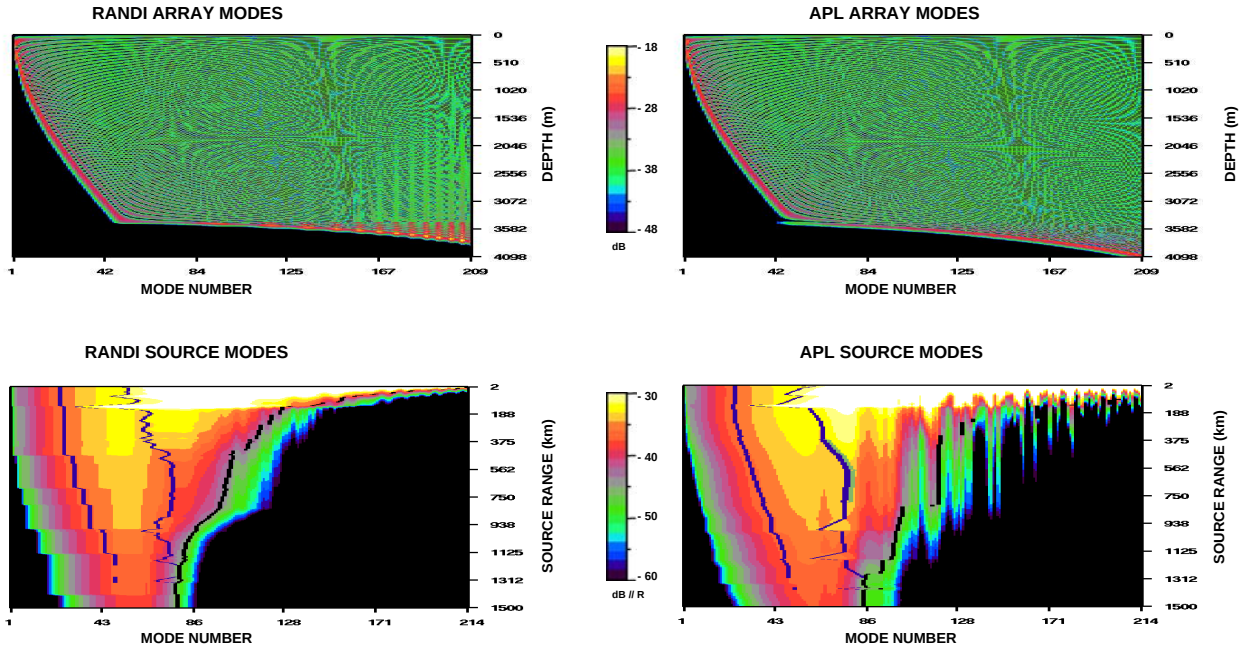

Fig. 38 — Mode function components for the RANDI and the APL Gulf of Alaska deep-water track: (top panels) array-mode functions; (bottom panels) source-mode functions; (left panels) RANDI components; (right panels) APL components

5.3 Continental-Shelf Track

The two environments for the continental-shelf track are illustrated in the water-column plots of Fig. 39 and the geoacoustic plots of Fig. 40.

As shown in Fig. 39, the bathymetry for both the RANDI and the APL environments is nearly flat out to a range of about 850 km. From about 850 km to about 900 km, there is a group of large seamounts that result in a decrease in water depth of over 2500 m for the RANDI environment and 1500 m for the APL environment. A detailed inspection of the bathymetry for the two environments indicates that the 1000 m difference in the water depths is due to the environmental partitioning used in the APL model. Beyond the seamounts, the water depth varies over about a 500 m interval out to a range of about 1580 km. At 1630 km, the water depth decreases to about 200 m at the beginning of the shelf.

The APL water-column sound speed is similar to the RANDI sound speed along the full length of the track, as was the case for the deep-water track. They both show an increase in the near surface sound speed and a deepening of the sound speed channel as the range increases out to about 1400 km. Beyond 1400 km, the near surface sound speed decreases somewhat.

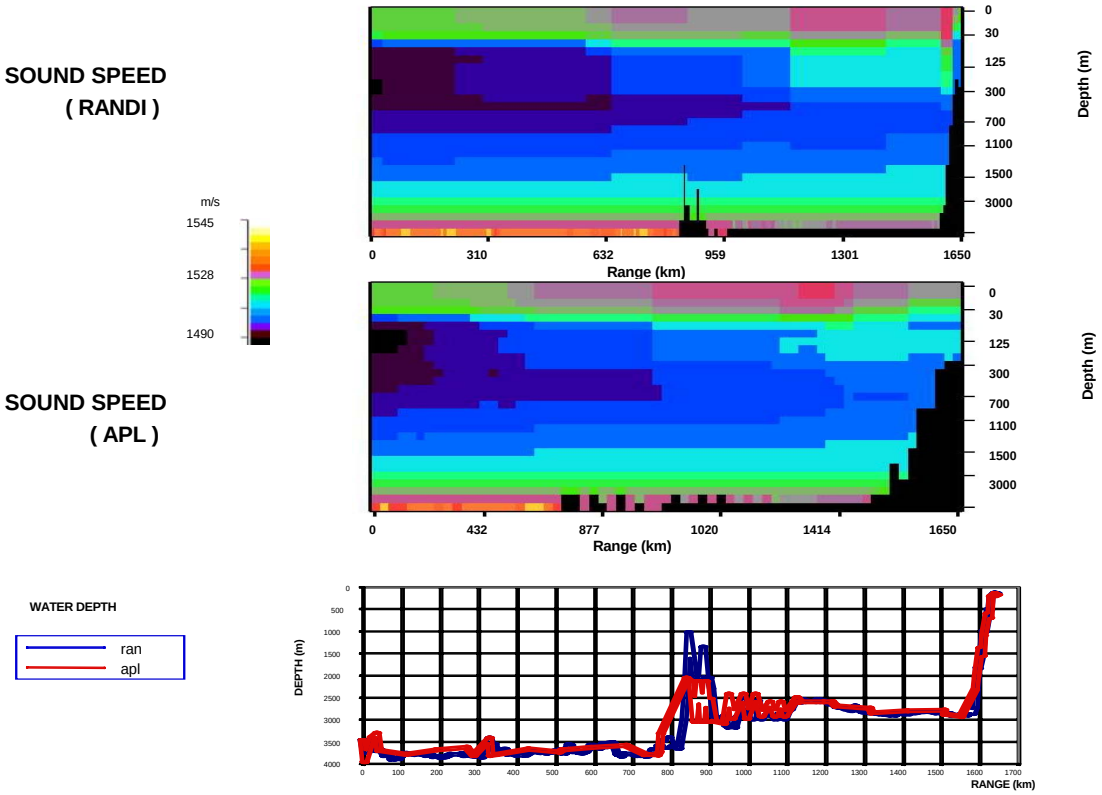

Fig. 39 — Sound speed and bathymetry comparisons for Gulf of Alaska continental-shelf track: RANDI sound-speed field (top); APL sound-speed field (middle); water depth comparison (bottom)

The sediment parameters are shown in Fig. 40. Note that for both environments, most of the sediment parameters incur significant changes within a few kilometers of the array site. For example, the RANDI sound-speed ratio increases from less than unity (0.99) to greater than unity (1.020) within a 0.5 km of the site. A listing of the parameter values at the site and a short distance away from the site is presented in Appendix B for both environments. Also note in Fig. 40 that all of the geoacoustic parameters, except the APL sediment thickness, are constant across the group of seamounts between 850 and 900 km.

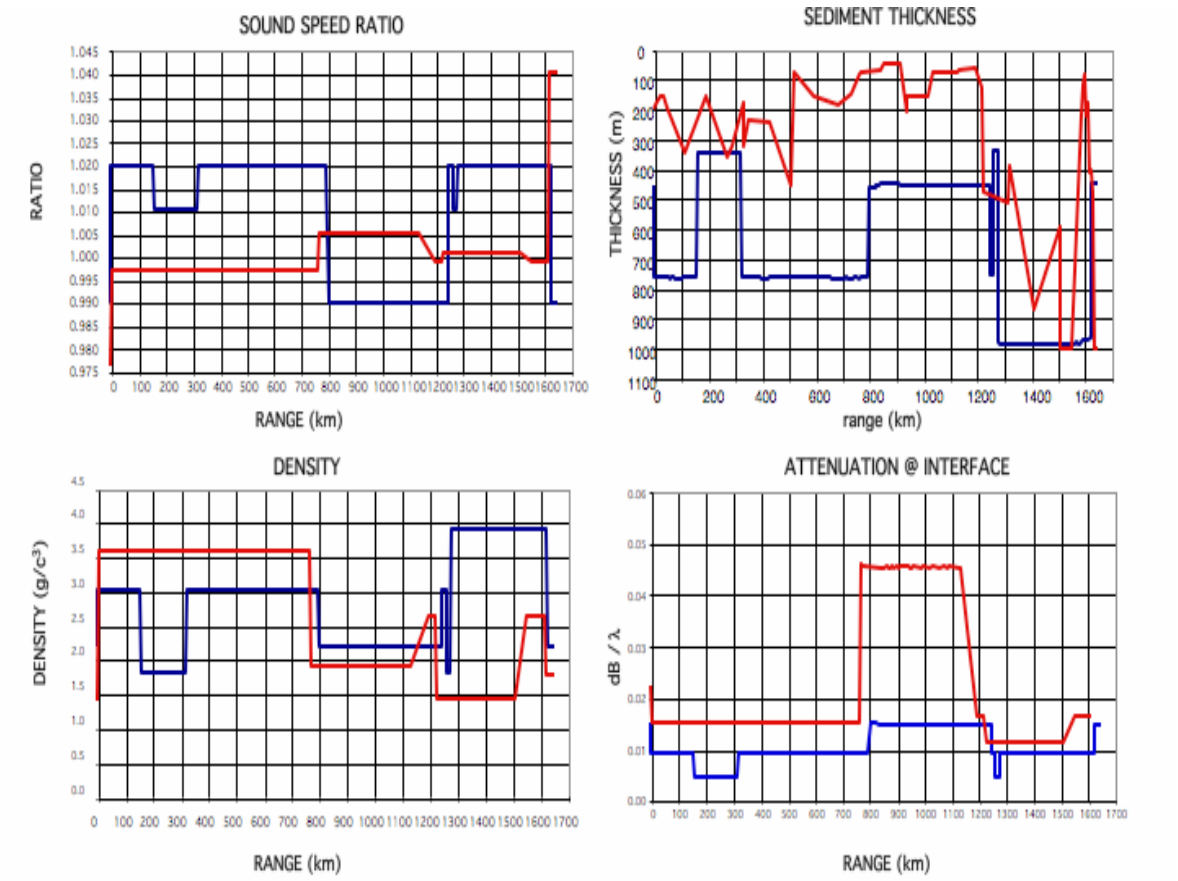

Fig. 40 — Geoacoustic parameters for the APL environment (red) and the RANDI environment (blue) on the Gulf of Alaska shelf track: sound-speed ratio (top left); sediment thickness (top right); sediment density (lower left); interface attenuation (lower right)

In Fig. 41, we show the received field and the vertical-arrival structure as a function of source range. To describe the plots in Fig. 41, we consider four range intervals: the *pre-seamount* interval, where the range extends to the beginning of the seamount; the *seamount* interval, where the range spans the seamounts; the *post-seamount* interval, where the range extends from just beyond the seamount to the slope; and the *slope/shelf* interval, where the range extends up the slope and onto the shelf. In the pre-seamount interval, both the RANDI and the APL fields are similar to those of the range-independent track, with the energy in the RANDI field slightly greater than the APL energy. In the seamount interval, there is a significant increase in the energy in both fields due to downslope conversion as the source approaches the seamount. This additional energy is distributed across the full water column and is accompanied by a reduction in the elevation angle separation between the peaks in the arrival structure plots. In the post-seamount interval, the energy in both fields decreases significantly and the elevation angle separation is reduced. Note that these changes are much greater for the RANDI field than for the APL field. Finally, in the slope interval, both fields show a significant increase in energy and a transition from a bimodal to a unimodal arrival structure as the source ranges extend into the region. In this region, the levels for the APL field are slightly larger than those for the RANDI field.

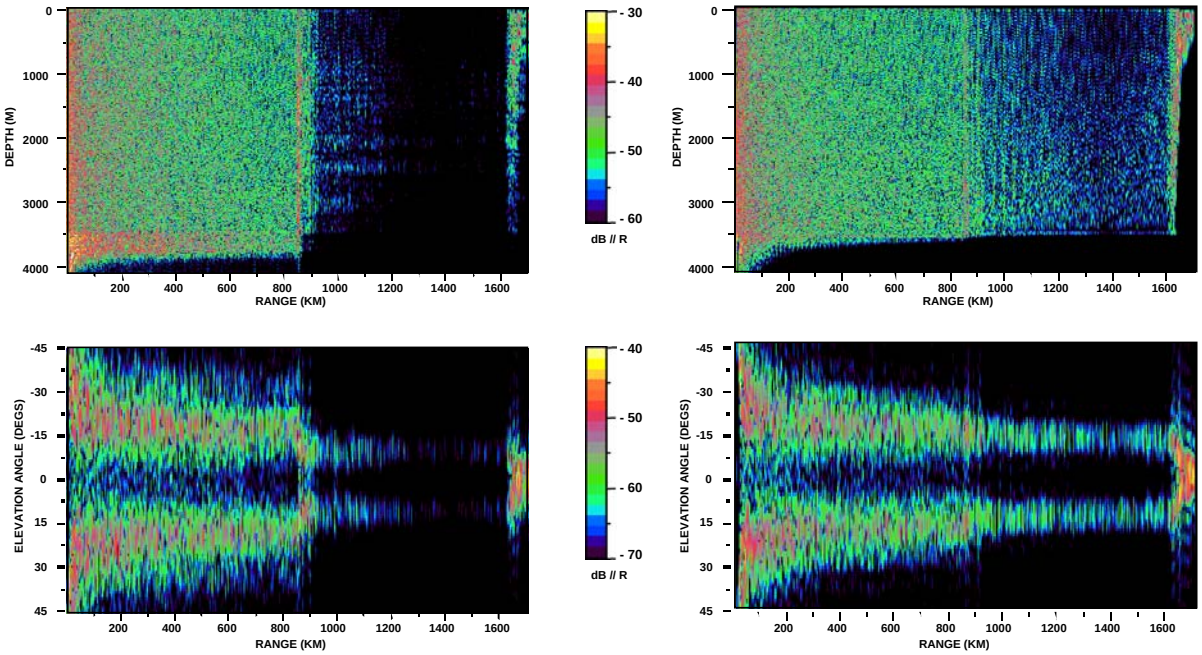

Fig. 41 — Propagation/environment acoustic field comparison for the Gulf of Alaska site continental-shelf track: (left panels) FEPE propagation model / RANDI environment; (right panels) ANM propagation model / APL environment; (top panels) range-depth distribution of the acoustic field; (bottom panels) vertical-arrival structure vs. range

The propagation comparison plots are shown in Fig. 42. We consider the four range intervals in turn. First, in the pre-seamount region, the propagation/environment plot indicates that the RANDI model energy is a few dB larger than the APL model energy. The propagation-only plot shows slightly more energy in the ANM curve than the FEPE curve with the extent of the difference increasing with range from about one dB at 250 km to over two dB at 700 km. This disparity indicates that the ANM propagation model slightly overestimates the energy over this range interval. Finally, the environment-only plot shows significantly more energy for the RANDI environment, with the difference increasing from 2 dB at 250 km to about 5 dB at 700 km. Thus, the comparatively small difference in the propagation/environment curves is due to the small increase in the ANM model energy partially compensating for the larger decrease in the APL environment energy.

Consider next the seamount region. In the propagation/environment plot, the RANDI model curve shows a slightly larger peak than the APL model curve and a somewhat longer tail. In the propagation-only plot, the ANM curve shows a slightly larger peak than the FEPE curve. Finally, in the environment-only plot, the levels in the APL curve are significantly less than those of the RANDI curve and are distributed over a much larger range interval. Thus, again, the small increase due to the ANM model energy partially compensates for the larger decrease due to the APL environment energy.

Consider next the post-seamount region. In this region, the propagation/environment plot shows that the difference between the APL model energy and the RANDI model energy increases from about 5 to around 10 dB as the source range increases. The propagation-only plot shows that the ANM energy is larger than the FEPE energy for ranges from about 1100 to about 1500 km, with the difference increasing with range from a few dB up to almost 10 dB. The environment-only plot shows that the APL environment energy is about 5 dB larger than the RANDI energy. Thus, in this case, the larger APL model energy is partly due to the larger energy for the adiabatic approximation and partly due to the larger energy associated with the APL environment.

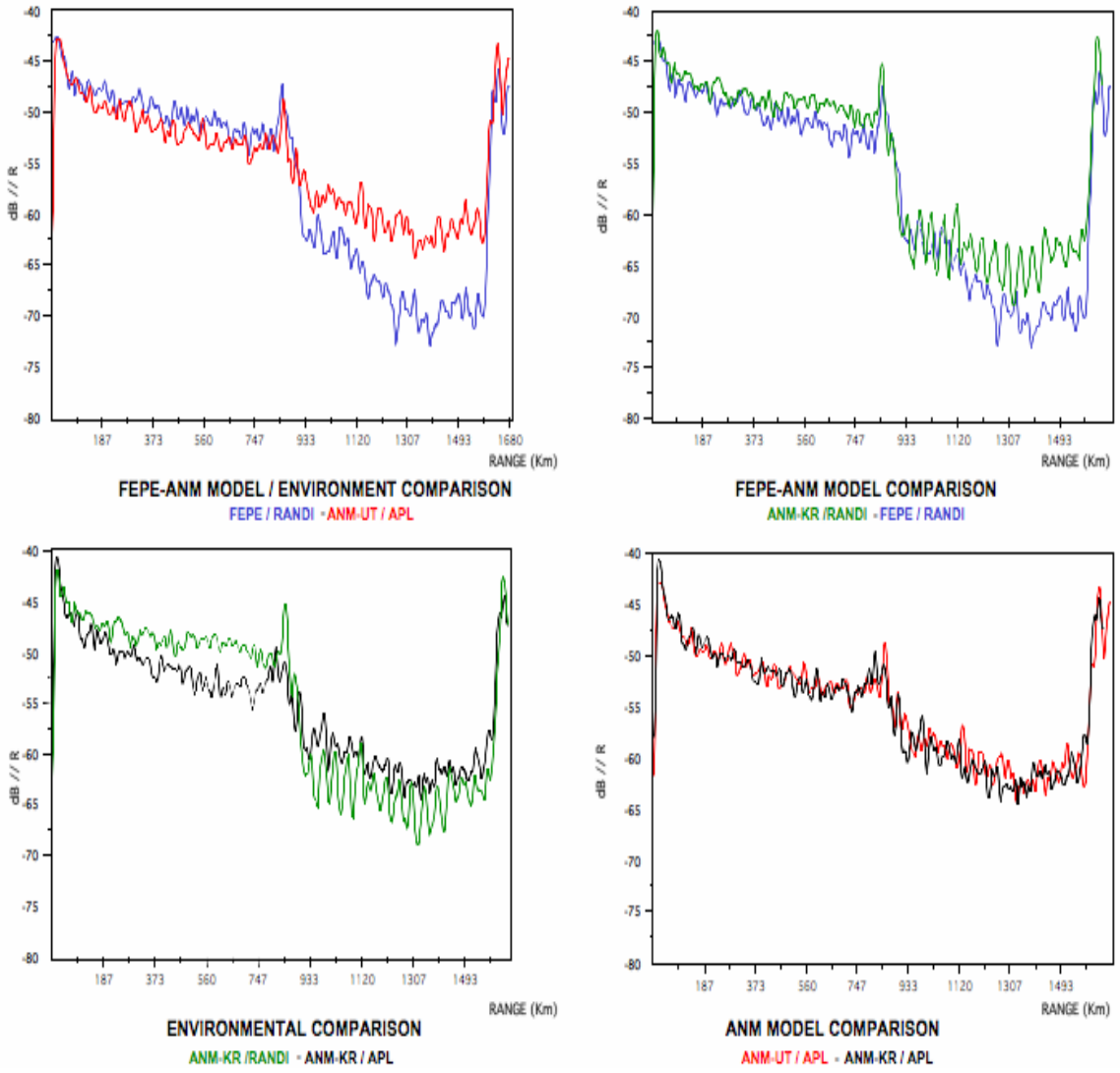

Fig. 42 — Depth-averaged propagation curves for the Gulf of Alaska continental-shelf track: propagation/environment comparison (top left); propagation-only comparison (top right); environment-only comparison (bottom left); ANM model comparison (bottom right).

Finally, consider the slope region. As seen in the propagation/environment plot, the APL model curve is slightly larger than the RANDI model curve and, unlike the Sargasso Sea, the APL energy does not cut off before the end of the track. The propagation-only plot shows that the ANM energy is larger than the FEPE energy over the slope part of the track, but that the ANM energy cuts off on the shelf part of the track. Thus, the propagation-only comparison indicates that, at least for the RANDI environment, the adiabatic approximation overestimates the energy for the slope portion of the track and underestimates the energy for the shelf part of the track. In the environment-only plot, the propagation curves extend only over the slope part of the region. Over this range interval, the peak of the RANDI curve is almost 2 dB greater than the peak of the APL curve.

The propagation curves in the ANM model comparison plot in the lower right are essentially the same over the full range interval except that in the seamount regions, the maximum peak for the ANM-UT model occurs at the same location as the smaller peak in the ANM-KRAKEN model.

The arrival structure comparison plots have been computed by averaging over two source range intervals, a 1000 km to 1400 km interval located just beyond the seamount and a 1620 km to 1650 km interval located on the slope. The 1000 km to 1400 km results are shown in Fig. 43.

An inspection of the propagation/environment plot of Fig. 43 indicates that the overall energy in the peaks of the arrival structure is about 7 dB greater for the APL model than for the RANDI model and that the depth of the notch is about 14 dB for the APL model compared to about 11 dB for the RANDI model. Furthermore, the separation between the peaks in the APL arrival structure (about 28°) is about 6° larger than for the FEPE/RANDI model (about 22°). An inspection of the propagation-only comparison and the environment-only comparison plots indicates that part of the difference in both the levels and the separation in the propagation/environment arrival structures is due to corresponding differences in both the propagation and the environmental components of the noise models.

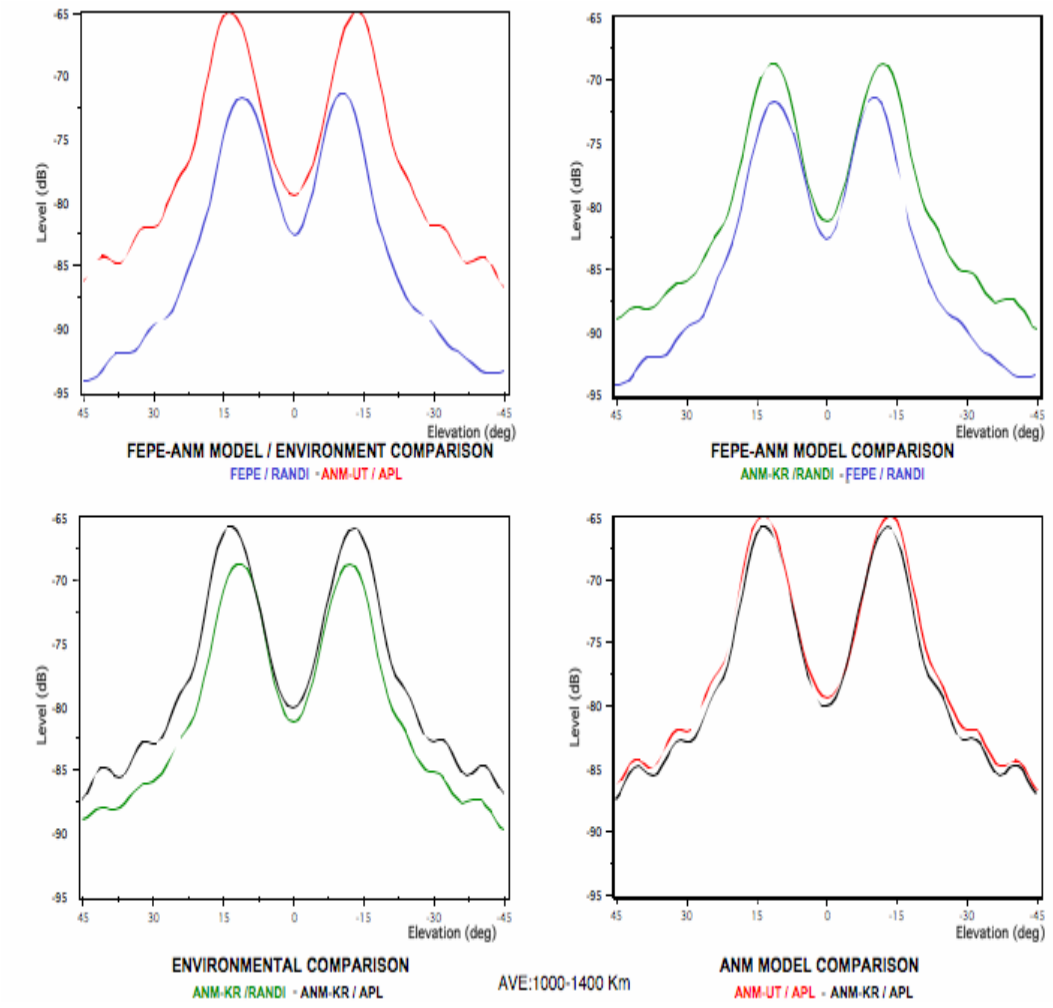

Fig. 43 — Range-averaged vertical-arrival structure for the Gulf of Alaska continental-shelf track for a 1000 km to 1400 km range interval: propagation/environment comparison (top left); propagation-only comparison (top right); environment-only comparison (bottom left); ANM model comparison (bottom right).

The arrival structure comparison plots for the slope region are shown in Fig. 44. The averaging interval (1620 to 1650 km) spans the shelf-break, which occurs at about 1630 km and extends about 20 km along the shelf, where the RANDI water depth varies between 224 m and 143 m. The arrival structure

plots show that the RANDI arrival structure has completely collapsed to the unimodal form, whereas the arrival structure for the APL model still exhibits remnants of the bimodal form. From the propagation-only plot, it is clear that this difference is due to differences in the FEPE and ANM models.

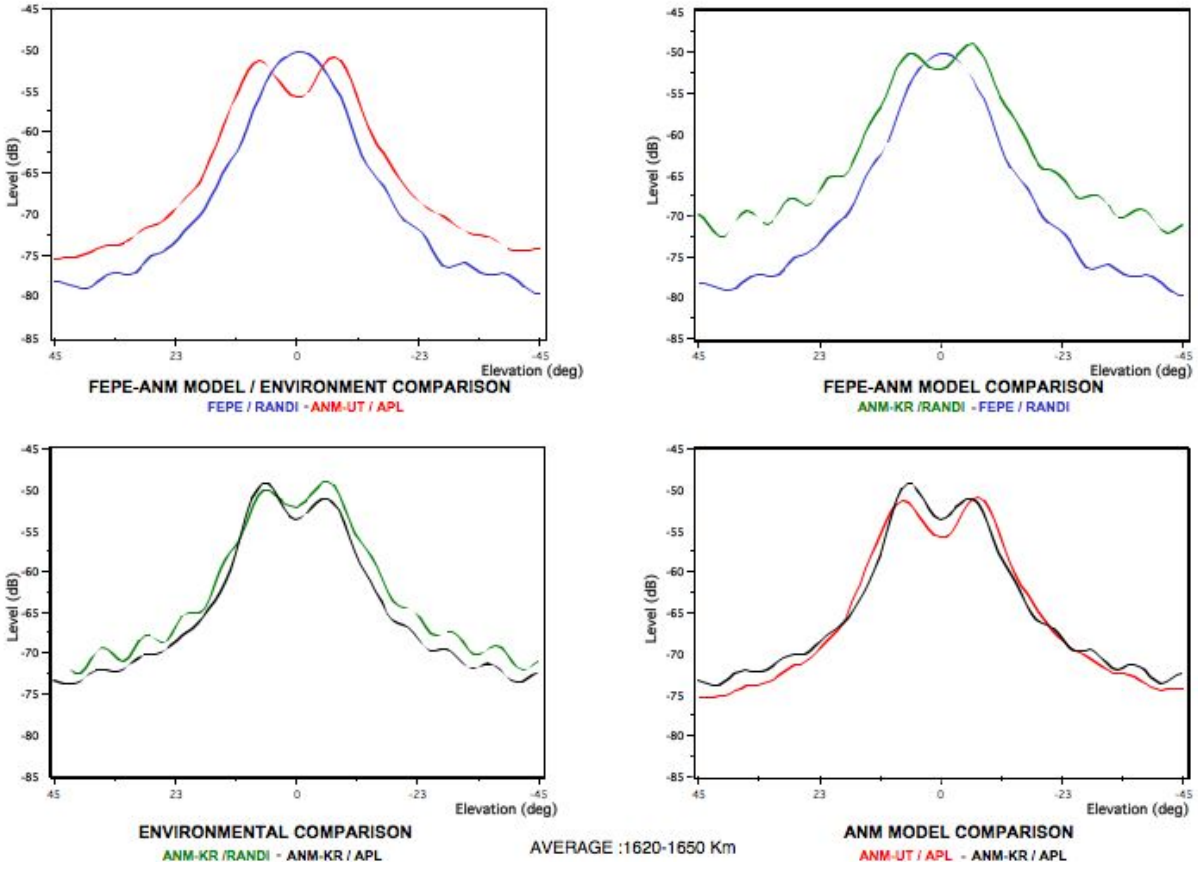

Fig. 44 — Range-averaged vertical-arrival structure for the Gulf of Alaska continental-shelf track for a 1620 km to 1650 km range interval: propagation/environment comparison (top left); propagation-only comparison (top right); environment-only comparison (bottom left); ANM model comparison (bottom right).

To interpret these results, we have plotted the ANM modal components for the two models in Fig. 45. As with the deep-water track, the array-mode functions, shown at the top of the figure, are the same as those for the range-independent track. Thus, the impact of the difference in the two environments on the propagation and the suitability of the adiabatic assumption for propagation from the slope and shelf is determined by the differences in the source-mode functions.

The source-mode functions are shown at the bottom of Fig. 45. An inspection of these plots indicates that the lower limits of the waterborne band (the leftmost blue curve) are approximately the same for both environments over the full range interval except for the seamount region between 850 and 900 km. The increase in these limits from about 24 at short ranges to the mid-thirties at almost 1600 km is largely due to the increasing water-column sound speed at the shallow source depths. The jumps in the lower limits for the RANDI environment are associated with the jumps in the sound speed profiles.

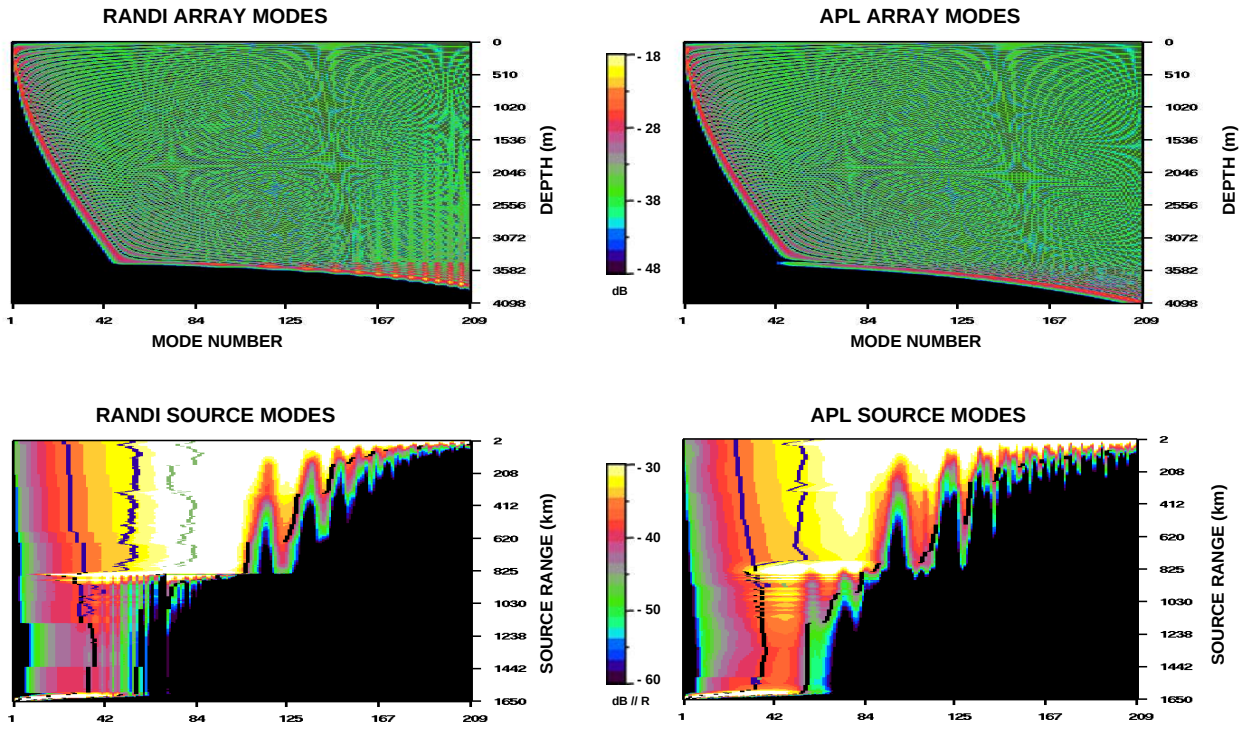

Fig. 45 — Mode function components for the RANDI and the APL Gulf of Alaska shelf track: (top panels) array-mode functions; (bottom panels) source-mode functions; (left panels) RANDI components; (right panels) APL components

Since the lower limits of the waterborne energy are similar for both environments, the difference in the propagation for the two environments is largely due to the difference in the upper limits for the waterborne energy and the sediment-interacting energy. We first consider these limits for the pre-seamount region (0 to 850 km) in which the environment-only plot of Fig. 42 shows significantly larger energy for the RANDI environment. For this region, the upper limits of the waterborne energy are also approximately the same for the two environments. These limits, which are primarily determined by the sound speed at the water depth, decrease with the bathymetry from around 50 near the site to around 40 at the approach to the seamount. For the RANDI environment, there is a total-reflection band that results from the unity excess of the sound-speed ratio (see Fig. 40). The upper limit in this band, shown by the green curve, is in the low eighties, except for ranges between about 150 km and 300 km, where the upper limit is somewhat smaller due to the slightly smaller sound-speed ratio. For the APL environment, the sound-speed ratio is less than unity (0.997) so that there is no total-reflection band and the upper limit of the waterborne band is the lower limit of the sediment refraction band. Now the width of the sediment refraction bands for the two environments is about the same. Thus, it is primarily the larger sound-speed ratio in the RANDI environment that gives rise to the total-reflection band that accounts for the larger energy in the RANDI propagation. We note in passing that the source-mode functions for both environments show localized increases at about 25 km and 340 km associated with the small seamounts that are present in both environments. These increases are the result of increases in the source-mode functions, $\varphi_m(z_s, r_s)$, rather than an increase in the modal attenuation, $\alpha_m(r_s)$, which is a non-decreasing function of source range.

We next consider the range interval that extends from the approach to the seamount out to the beginning of the slope/shelf region. In this interval, the environment-only plots of Fig. 42 indicate that the RANDI environment energy is larger in the seamount region, but as much as 5 dB smaller over most of the remaining interval. To interpret this result, note that both source-mode functions show a significant

increase in energy as the source passes over the seamount. This increase extends down to the low order modes with a lower limit that roughly follows the contour of the bathymetry. As the source range moves just beyond the seamount, the energy is sharply diminished due to the attenuation loss in the seamount sediment layer. This loss is larger for the RANDI environment since the seamounts extend further into the water column and hence, affects the modes down to smaller mode numbers.

We next consider the range interval that extends from the approach to the seamount out to the beginning of the slope/shelf region. In this interval, the environment-only plots of Fig. 42 indicate that the peak of the RANDI environment curve in the seamount region is larger than the APL curve, but that the energy is as much as 5 dB smaller over most of the remaining interval. To interpret this result, note that both source-mode functions show a significant increase in energy as the source passes over the seamount. This increase extends down to the low order modes with a lower limit that roughly follows the contour of the bathymetry. The increase is larger for the RANDI environment than for the APL environment since the seamounts extend further into the water column. As the source range moves just beyond the seamount, the energy in both source-mode functions is sharply reduced due to the attenuation loss in the seamount sediment layer. This loss is larger for the RANDI environment since the seamounts extend further into the water column and hence, affects the modes down to smaller mode numbers. Thus, it is primarily the difference in the depth of the seamounts that results in the difference in the environment-only propagation curves of Fig. 44 in the region following the seamounts as well as the seamount region itself.

Finally, we consider the slope region. In contradistinction to the Sargasso Sea, the energy in the ANM propagation curve does not cut off as the source moves towards the shelf-break. To see why this is the case, note that, as for the Sargasso Sea, the source-mode functions become negligible for the larger mode numbers as the source moves up the slope and the water depth decreases. In particular, there is an upper limit on the modes for which the source-mode function is significant; that limit decreases as the source range increases, and hence, the water depth decreases. This was also the case for the Sargasso Sea. However, unlike the Sargasso Sea, for most of the 50 m to 250 m depth interval subtended by the array, the array-mode function is significant for all modes. Thus, unlike the Sargasso Sea, where there is a non-degenerate lower limit imposed by the sampling of the array-mode functions at the array depths, the product of the array-mode function and the source-mode function is not negligible as the source moves up the slope and on to the shelf.

We conclude this section with an interpretation of the propagation-only curves in terms of the source-mode function for the FEPE field. This function, along with the ANM source-mode function, is shown in Fig. 46. As for the Sargasso Sea, both source-mode functions are computed for the RANDI environment. An inspection of the figure indicates that for source ranges on the near side of the seamount, the ANM source-mode function has more energy in the waterborne, the total-reflection, and the sediment-refraction bands than the FEPE function, but the FEPE function has significant energy at the higher modes outside these bands. Nevertheless, the overall energy in the FEPE function is less than the ANM function, as expected from the slightly smaller FEPE propagation curve seen in the propagation-only comparison of Fig. 42. Furthermore, as expected from Fig. 42, there is less energy in the FEPE function for source ranges on the far side of the seamount. For source ranges in the near-slope/on-slope region, the FEPE function shows energy extending out to larger mode numbers than the ANM function due to mode conversion in downslope propagation. However, since the array essentially samples the energy in all modes, it is the total energy in the band that is observed and the total energy in the ANM function is slightly larger than in the FEPE function.

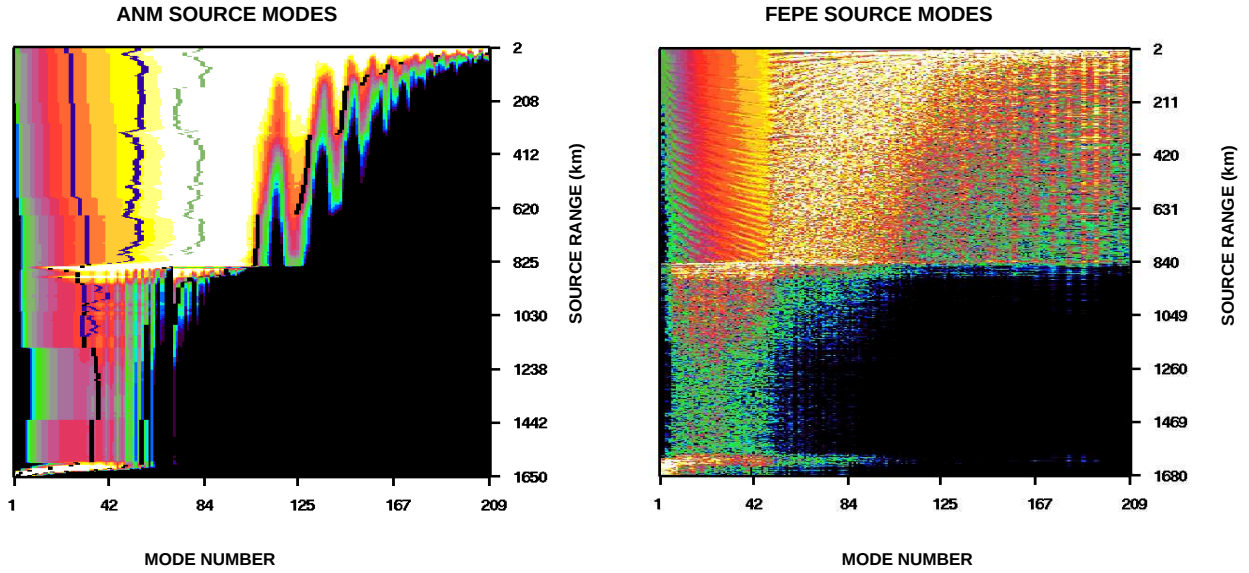

Fig. 46 — Source-mode functions for the Gulf of Alaska shelf track with the RANDI environment: ANM source-mode function (left); FEPE source-mode function (right)

6. SUMMARY AND DISCUSSION

This report has described bearing-elevation noise directionalities obtained from two ship-induced noise models, RANDI and APL, in two different areas — the Sargasso Sea and the Gulf of Alaska. The noise directionalities were computed using the same ship locations and ship source levels so that the only difference in the noise directionalities is due to differences in the propagation and the environmental components for the two noise models (RANDI: direct sampling of the environment and an FEPE propagation model; APL: "environmental partitioning" and an ANM propagation model). The differences in the noise directionalities were interpreted through an analysis of the acoustic propagation properties for selected tracks.

The Sargasso Sea noise directionalities for the two models were seen to be significantly different. The APL elevation-angle directionality showed deep noise notches for the shelf sector (6 dB) as well as the deep-water sector (12 dB) and the full-bearing sector (9 dB). In contrast, the RANDI directionality showed no vertical noise notch at all for the shelf sector and much smaller noise notches in the deep-water sector (6 dB) and the full-bearing sector (3 dB). Outside of the noise notch angles, the overall levels of the RANDI directionalities were about 2 dB larger than the levels of the APL directionalities. The peaks in the elevation-angle directionalities for both models occurred at about ± 13°.

For the RANDI model, the level-angle distribution indicated that it is largely the contributions from ships located near the shelf-break that fill in the noise notch in the shelf and the full-bearing sectors. These ship contributions arrive at the site at small horizontal angles because of the transfer of energy from high order modes to low order modes during downslope propagation. For the APL model, the level-angle distribution indicated that almost all of the ships that lie within the 200 m contour of the North American coast do not contribute significant energy to the APL directionality. The propagation analysis for the shelf track in Section 4 indicated that the lack of contributions from ships near the shelf-break in the APL model was a consequence of a fundamental "mode-set-disjunction" artifact of adiabatic-normal-mode propagation models.

In comparison to the Sargasso Sea, the Gulf of Alaska directionalities have significantly deeper noise notches and slightly larger peak separations. Furthermore, the directionalities for the two noise models are

more similar to one another than in the Sargasso Sea. The directionalities for both models show a noise notch for all three sectors. For the deep-water and the full-bearing sectors, the noise notch depths for the two models are comparable, about 14 dB in the deep-water sector and about 11 dB in the full-bearing sector. In the shelf sector, the noise notch depths are smaller than in the other sectors and differ somewhat from each other, 8 dB for the RANDI model, 5 dB for the APL model. The peaks in the elevation-angle directionalities for all sectors are only slightly larger for the APL model, $\pm 15°$ for the APL model, and $\pm 14°$ for the RANDI model. The noise directionalities for the two models differ somewhat in their overall levels, with the APL directionalities being as much as several dB larger than those for the RANDI directionalities at the smaller angles only.

The level-angle distributions indicated that the well-defined noise notches in the Gulf of Alaska directionalities are a consequence of the preponderance of large angle contributions for both noise models. In contrast to the Sargasso Sea, the level-angle distributions for neither noise model show a significant number of low angle contributions. This deficiency is largely due to the fact that there are only a small number of ships located near the shelf-break, which in turn is a consequence of the much smaller breadth of the continental shelf in the Northeast Pacific. The few ships located near the shelf do not fill in the RANDI noise notch more than the APL noise notch because the mode-set-disjunction limitation of the ANM propagation model does not apply at the Gulf of Alaska site.

The different noise model results were interpreted through a detailed analysis of the acoustic propagation at both sites.

The Sargasso Sea results are summarized as follows. For sources along the range-independent track, the RANDI field at the receiver exhibits significantly more energy than the APL field (7 dB at 500 km). The difference in the two fields is essentially due only to the differences in the geoacoustic properties. An analysis conducted by varying each of the three geoacoustic profiles, (compressional speed, density, and attenuation), indicated that among the geoacoustic parameters, the sound-speed ratio has a larger effect than the density and the interface attenuation, although all three parameters were important. The effect of the sound-speed ratio difference is to introduce a total-reflection band into the RANDI source-mode function, for which the mode attenuation is negligible.

For sources along the deep-water track, the RANDI field at the receiver again exhibits significantly more energy than the APL field (8 dB at 1500 km). As the source range increases over the first half of the 1500 km track, the APL energy falls off much more rapidly than the RANDI energy. This was attributed primarily to the differences in the geoacoustic parameters for the two environments based on the parameter substitution propagation curves from the range-independent track. For source ranges over the last half of the track, the fall-off rate in energy is comparable for the two models. This was attributed to the 400 m increase in the water depth that occurs near the midpoint of the track. This increase results in a redistribution of energy from sediment-refracted modes, which are highly attenuated, into the totally reflected and the waterborne modes, which are weakly attenuated. Accordingly, the propagation for source ranges in the last half of the track is less dependent on the geoacoustic parameters. Only a few dB of the difference in the propagation for the two models was attributed to the difference in the sound-speed fields and to the different propagation models.

The results for the deep-water track propagation suggest that the somewhat higher levels in the RANDI noise directionality are due in large part to differences between the geoacoustic parameters of the two environmental models. This is not surprising since for the shallow source depths relevant to ship-induced noise, the acoustic field for deep-water tracks in the Sargasso Sea is dominated by the sediment-interacting component. Accordingly, the sound speed in the water column, which controls the waterborne component of the acoustic field, plays a secondary role.

For the continental-shelf track, the energy in the RANDI field exceeds the APL energy by less than a few dB for source ranges out to nearly midway up the slope and by less than about 5 dB for ranges that extend further up the slope (about the 400 m depth point). At that range, the local maxima of the energy for the two models are essentially equal. The small difference in the energy between the two models in the first part of the track is due to environmental differences. It was seen that the high energy in the RANDI environment, which is largely due to the presence of a total-reflection band, is nearly achieved by the APL environment because of an unusually small amount of sediment attenuation. The larger difference in the energy between the two models as the source range approaches the slope break was attributed to deficiencies in the adiabatic-normal-mode model.

The most important difference for the shelf track occurs as the source range continues up the slope and extends out onto the shelf itself. At the onset of this range interval, the APL energy falls off over 35 dB within a few km; whereas, the RANDI energy remains significant for ranges well up onto the shelf. The analysis of the ANM source-mode functions indicated that the extremely sharp fall off in the APL energy results because the modes excited by the source with significant energy are not observed at the receiver. In particular, for the shallow depths associated with the near-shelf/on-shelf source ranges, only the lower order modes have significant energy at appreciable ranges. However, for the specific receiver depth assumed in the computations (150 m), which is not close to the sound speed minimum, there is a lower bound on the modes that the array observes. This lower bound exceeds the upper bound on the modes that are excited by the source with significant energy. We referred to this effect, which is an artifact of the adiabatic-normal-mode model, as mode-set-disjunction. It is because of this mode-set-disjunction that the APL model is unable to describe near-shelf/on-shelf source contributions. That mode-set-disjunction is not a limitation for the FEPE model was seen in the FEPE source-mode function, where the energy from sources at the near-shelf/on-shelf ranges extended into the band of modes observed by the receiver.

The Gulf of Alaska propagation results are summarized as follows. For sources along the range-independent track, the RANDI field has more energy at the receiver than the APL field, but the difference is less than the difference in the Atlantic (only a few dB at 500 km compared to 7 dB at 500 m). The comparison of the source-mode functions indicated that the waterborne modes account for a much larger fraction of the total mode band than in the Sargasso Sea.

For sources along the deep-water track, the energy in the APL field at the receiver is comparable to that of the RANDI model over the first half of the track and only a few dB larger over the last half of the track. Both models show decreases in energy with source range that are comparable to the large decreases observed for the APL model in the deep-water track of the Sargasso Sea. In the Sargasso Sea, this decrease was due to the attenuation of the sediment-refracted energy over the first half of the track. In the Gulf of Alaska, this decrease is due to an increase in the near surface sound speed as the latitude along the track decreases. The comparability of the two fields for the Gulf of Alaska deep-water track is due in part to the compensation of small differences in the energy due to environmental differences by small differences due to the propagation models.

The continental-shelf track has a group of seamounts located slightly more than midway along the track. For sources in the region prior to the seamounts, the APL energy is a few dB larger than the RANDI energy. This small difference is due to a small propagation-model difference effect partially compensating for a larger environmental difference effect. For sources in the vicinity of the seamounts, the peak in the received energy for the RANDI model is slightly larger than the peak in the energy for the APL model. This results from a large energy peak for the ANM propagation model more than compensating for a smaller energy peak for the APL environment. The small energy peak for the APL environment is due, in part, to the considerably smaller peaks in the APL bathymetry. For sources beyond the seamount, the received energy in the APL field is from 10 to 20 dB greater than the energy in the RANDI field. This is due to both a propagation-model difference and a environment difference.

For source ranges that are close to or on the shelf, the APL energy at the receiver is comparable to the RANDI energy. The mode-set-disjunction associated with the adiabatic approximation does not occur since the receiver is near the sound speed minimum, and hence, the lower limit on the modes observed by the array is less than the upper limit of the modes excited by the source. Thus, in the Gulf of Alaska, the APL model can describe near-shelf and on-shelf source contributions. Although, as noted above, the number of ships that are actually in the region is small because of the narrow breath of the shelf in the Northeast Pacific.

ACKNOWLEDGMENTS

The authors are grateful for the support of the Office of Naval Research base funding at the Naval Research Laboratory.

REFERENCES

1. J.E. Breeding, L.A. Pflug, M. Bradley, M. Hebert, and W. McBride, “RANDI 3.1 Physics Description,” Naval Research Laboratory Technical Report NRL/FR/7176--95-9628 (1996).

2. J.E. Breeding, L.A. Pflug, M. Bradley, M. Hebert, and M. Wooten, “RANDI 3.1 User's Guide,” Naval Research Laboratory Memorandum Report NRL/MR/7176--94-7552 (1994).

3. J.S. Perkins, W.A. Kuperman, F. Ingenito, L.T. Fialkowski, and J. Glattetre, “Modeling Ambient Noise in Three-dimensional Ocean Environments,” *J. Acoust. Soc. Am.* **92**, 739-752 (1993).

4. Naval Oceanographic Office, “Data Base Description for Historical Temporal Shipping 3.0,” OAML-DBD-43, Stennis Space Center, MS (1993).

5. M.D. Collins, “FEPE User's Guide,” NORDA Technical Note 365, Naval Research Laboratory, Stennis Space Center, MS (1988).

6. M.D. Collins, “Applications and Time-Domain Solution of Higher-Order Parabolic Equations in Underwater Acoustics,” *J. Acoust. Soc. Am.* **86**, 1097-1102 (1989).

7. S.J. Levinson, E.K. Westwood. R.A. Koch, S.K. Mitchell, and C.V. Sheppard, “An Efficient and Robust Method for Underwater Acoustic Normal-Mode Computations,” *J. Acoust. Soc. Am.* **97**(3), 1576-1585 (1995).

8. A.D. Pierce, “Extension of the Method of Normal Modes to Sound Propagation in an Almost-Stratified Medium,” *J. Acoust. Soc. Am.* **37**, 19-27 (1965).

9. F.B. Jensen, W.A. Kuperman, M.B. Porter, and H. Schmidt, *Computational Ocean Acoustics* (American Institute of Physics, Woodbury, NY, 1994), pp. 320-328.

10. W.A. Kuperman, M.B. Porter, and J.S. Perkins, “Rapid Computation of Acoustic Fields in Three-Dimensional Ocean Environments,” *J. Acoust. Soc. Am.* **89**(1), 125-133 (1990).

11. Naval Oceanographic Office, “Data Base Description for Digital Bathymetric Data Base Confidential (DBDBC),” OAML-DBD-17A, Stennis Space Center, MS (1987).

12. Naval Oceanographic Office, “Data Base Description for Master Generalized Digital Environmental Model (GDEM) Version 3.0,” OAML-DBD-19B, Stennis Space Center, MS (1990).

13. Naval Oceanographic Office, “Data Base Description for Low-Frequency Bottom Loss (LFBL),” OAML-DBD-12B, Stennis Space Center, MS 1990.

14. L.M. Brekhovskikh and Y.P. Lysanov, *Fundamentals of Ocean Acoustics*, Springer Series on Wave Phenomena, Springer-Verlag, 2nd edition, Chapter 6, 1991.

Appendix A
SARGASSO SEA

This appendix contains the range-independent environmental parameters, the reflection and transmission coefficients, and the sediment compressional speed and attenuation fields for the Sargasso Sea tracks. Figure A1 shows the reflection and transmission coefficients for the RANDI and APL environments. Figures A2 and A3 show the sediment compressional speed and attenuation fields for the deep-water track, while Figs. A4 and A5 show the same for the shelf track.

RANGE-INDEPENDENT ENVIRONMENTAL PARAMETERS

In Table A1, the critical depth is that depth where the sound speed has the same value as the sound speed at the surface. The depth excess is the difference between the water depth and the critical depth. The sound-speed ratio is the ratio of the compressional speed in the sediment to the sound speed in the water column, both determined at the water-sediment interface. The compressional speed gradient is also measured at the water-sediment interface.

The arrival angle limits determine a partition of arrival angles such that the propagation is waterborne-only for arrival angles between θ_w and θ_{sw} and sediment-interacting-only for angles between θ_{sw} and θ_b. For angles greater than θ_b, the energy interacts with the basement. The arrival angle limits shown in the table are computed for a depth of 150 m, which is the center of the array[3]. Note that the sediment properties and the water depth for the APL environment do not include the 1000 m extension[4].

REFLECTION / TRANSMISSION COEFFICIENTS

The reflection and transmission coefficients for the two environments are illustrated in Fig. A1. It is seen that for the larger grazing angles, fully 60% of the energy is reflected for the RANDI environment and only about 18% for the APL environment. However, much of the transmitted energy is refracted in the sediment layer and returns to the water column. In Fig. A1, we have neglected the loss in the computation of reflection and transmission coefficients.

[3] The arrival angle limits are computed from the sound speed profiles using Snell's Law. The angle θ_w is the arrival angle at the array center depth of 150 m for a zero degree departure angle at the surface. The angle θ_{sw} is the arrival angle for a zero degree departure angle at the water-sediment interface and the angle θ_b is the arrival angle for a zero degree departure angle at the sediment-basement interface.

[4] With this extension, the total depth is 7334 and the basement arrival angle limit is 60.04 degrees.

Table A1 — RANDI and APL Environmental Parameters for Sargasso Sea Site

	RANDI	**APL**
Water Column		
Conjugate Depth (5 m)	4886 m	4787 m
Conjugate Depth (150 m)	3885 m	3777m
Depth Excess	426 m	552 m
Water Depth	5309 m	5334 m
Sediment layer		
Sound-speed ratio	1.020	0.9960
Compressional Speed Gradient	1.1 m/s/m	1.3 m/s/m
Density	3.92 g/cm^3	1.42 g/cm^3
Sediment Thickness	1015 m	1000 m
Total Depth	**6324 m**	**6334 m**
Arrival Angle Limits (@150 m)		
Waterborne lower limit (θ_w)	8.5°	8.5°
Sediment lower limit (θ_{sw})	10.3°	10.7°
Basement limit (θ_b)	47.79°	50.8°

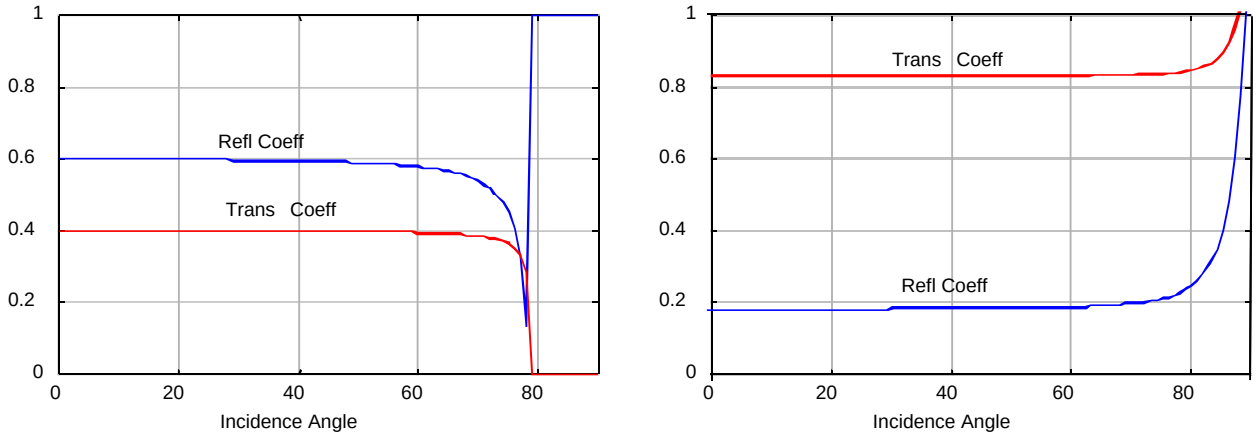

RANDI **APL**

Fig. A1 — Reflection and transmission coefficients at the Sargasso Sea site for the RANDI environment (left) and the APL environment (right)

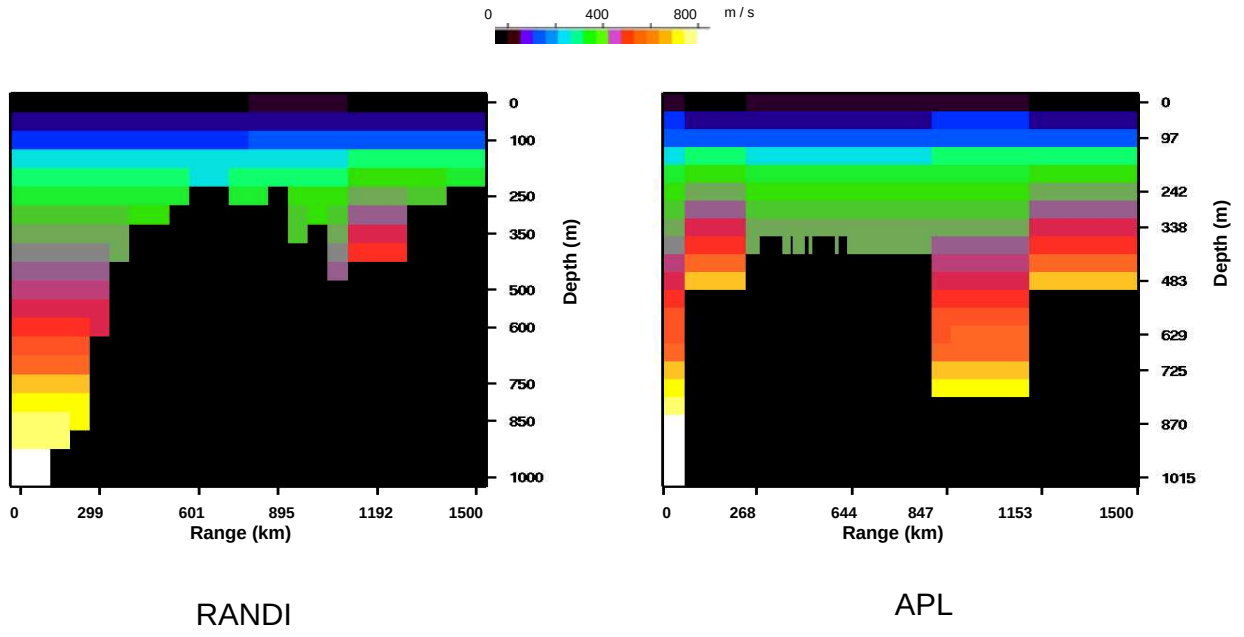

Fig. A2 — Sediment compressional speed fields for the deep-water track in the Sargasso Sea: RANDI environment (left) and the APL environment (right)

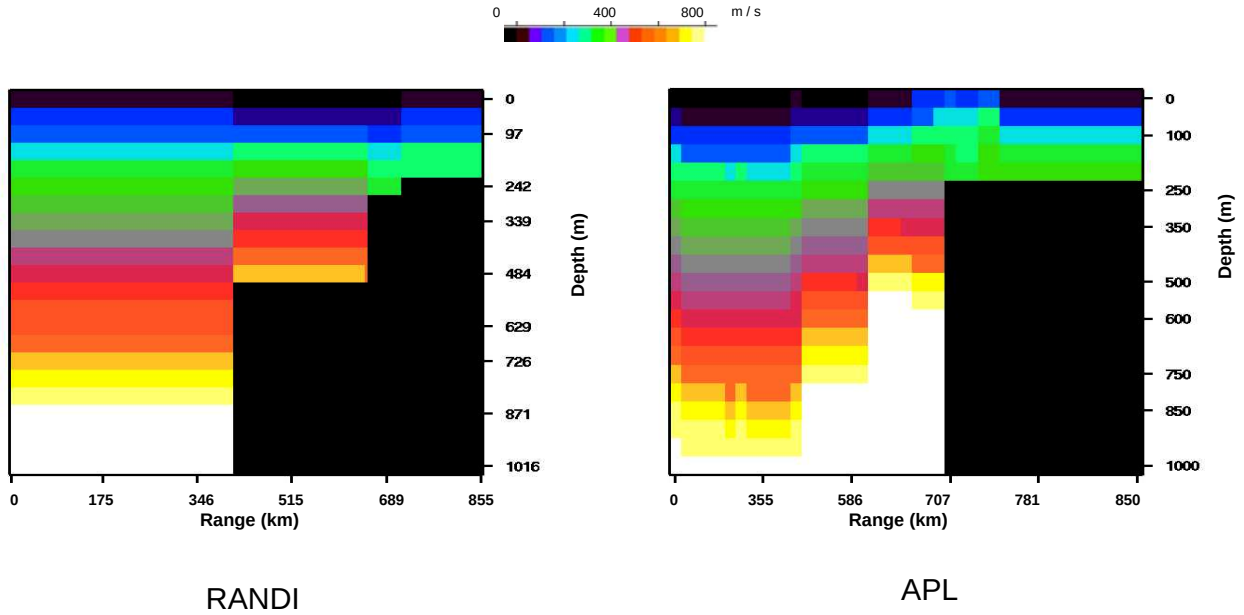

Fig. A3 — Sediment attenuation fields for the deep-water track in the Sargasso Sea: RANDI environment (left) and the APL environment (right)

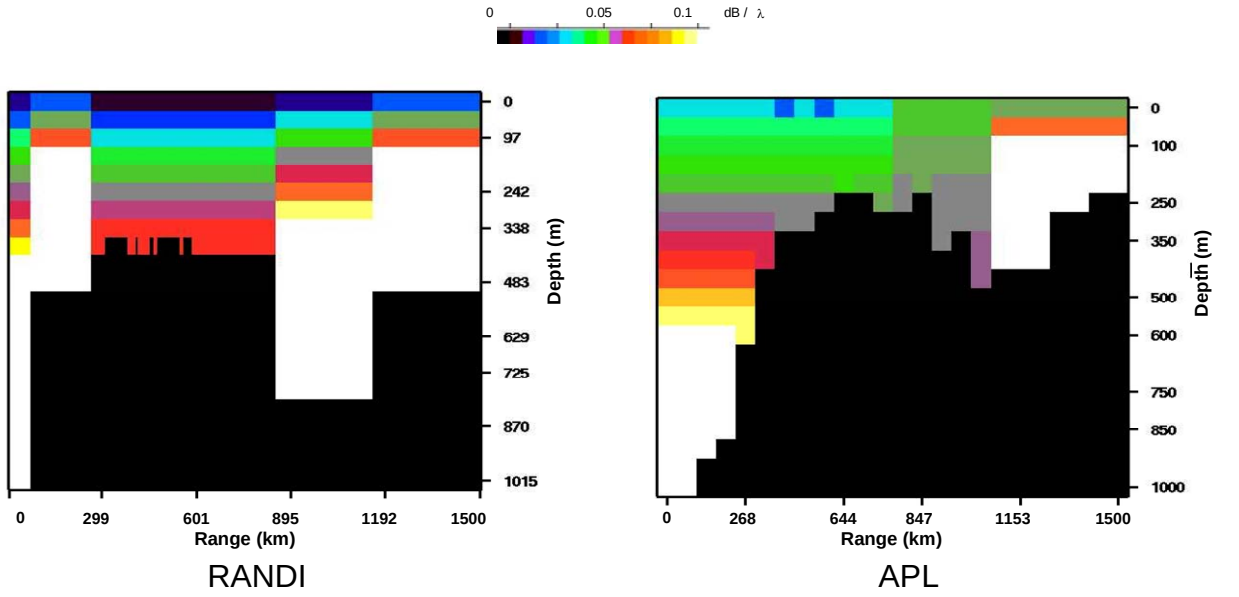

Fig. A4 — Sediment compressional speed fields for the shelf track in the Sargasso Sea: RANDI environment (left) and the APL environment (right)

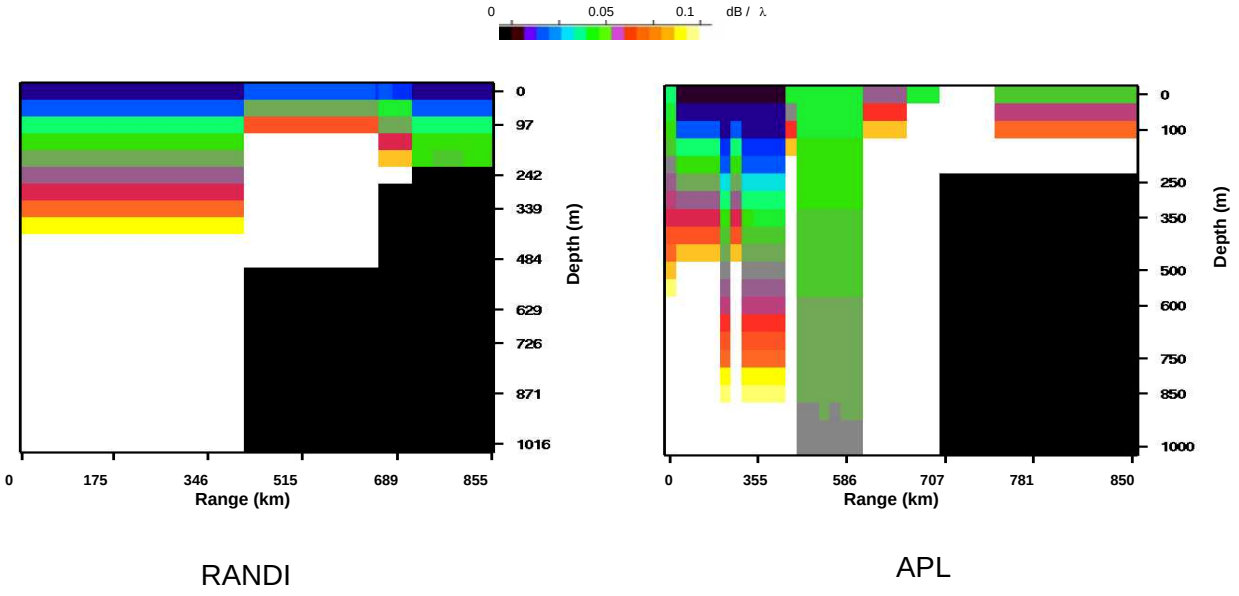

Fig. A5 — Sediment attenuation fields for the shelf track in the Sargasso Sea: RANDI environment (left) and the APL environment (right)

Appendix B
GULF OF ALASKA

This appendix contains the range-independent environmental parameters, the reflection and transmission coefficients, and the sediment compressional speed and attenuation fields for the Gulf of Alaska tracks. Figure B1 shows the reflection and transmission coefficients for the RANDI and APL environments. Figures B2 and B3 show the sediment compressional speed and attenuation fields for the deep-water track, while Figs. B4 and B5 show the same for the shelf track.

RANGE-INDEPENDENT ENVIRONMENTAL PARAMETERS

Parameters of the two environments are listed in Table B1. As seen in a comparison of Tables A1 and B1, the water depths for the Gulf of Alaska are considerably smaller than those for the Sargasso Sea, the depth excesses are considerably larger, and the waterborne and sediment lower limit angles are appreciable larger. Also note that the sediment thicknesses for the Gulf of Alaska are less than those for the Sargasso Sea, although, as in Table A1, the sediment parameters for the APL environment do not include the 1000 m extension.

Table B1 — RANDI and APL Environmental Parameters for Gulf of Alaska Site

	RANDI	**APL**
Water Column		
Conjugate Depth (5 m)	2261 m	2298 m
Conjugate Depth (150 m)	318 m	82 m
Depth Excess	1199 m	1161 m
Water Depth	3456 m	3456 m
Sediment layer		
Sound-speed ratio	0.9900	0.9760
Sound Speed Gradient	1.6 m/s/m	0.9 m/s/m
Density	2.20 g/cm^3	1.41 g/cm^3
Sediment Thickness	459 m	203 m
Total Depth	3915 m	3659 m
Arrival Angle Limits (@150 m)		
Waterborne lower limit (θ_w)	10.3°	10.6°
Sediment lower limit (θ_{sw})	13.8°	14.0°
Basement limit (θ_b)	47.9°	27.1°

REFLECTION / TRANSMISSION COEFFICIENTS

The reflection and transmission coefficients for the two environments are illustrated in Fig. B1. These plots indicate that for the larger grazing angles about 40 percent of the energy is reflected for the RANDI environment and only about 18 percent is reflected for the APL environment. This difference is primarily due to the larger density in the RANDI environment. In Fig. B1, we have neglected the loss in the computation of reflection and transmission coefficients.

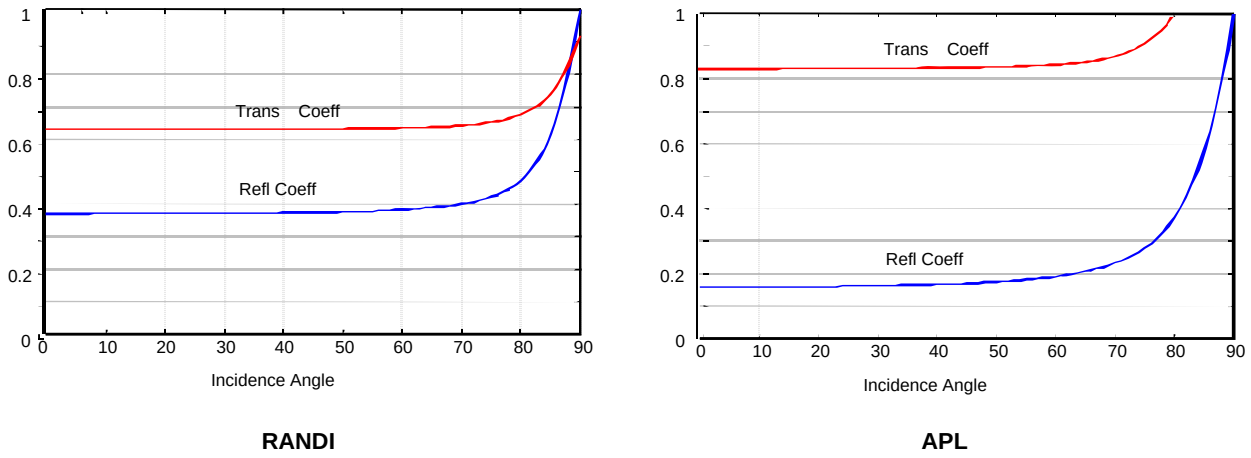

Fig. B1 — Reflection and transmission coefficients at the Gulf of Alaska site for the RANDI environment (left) and the APL environment (right)

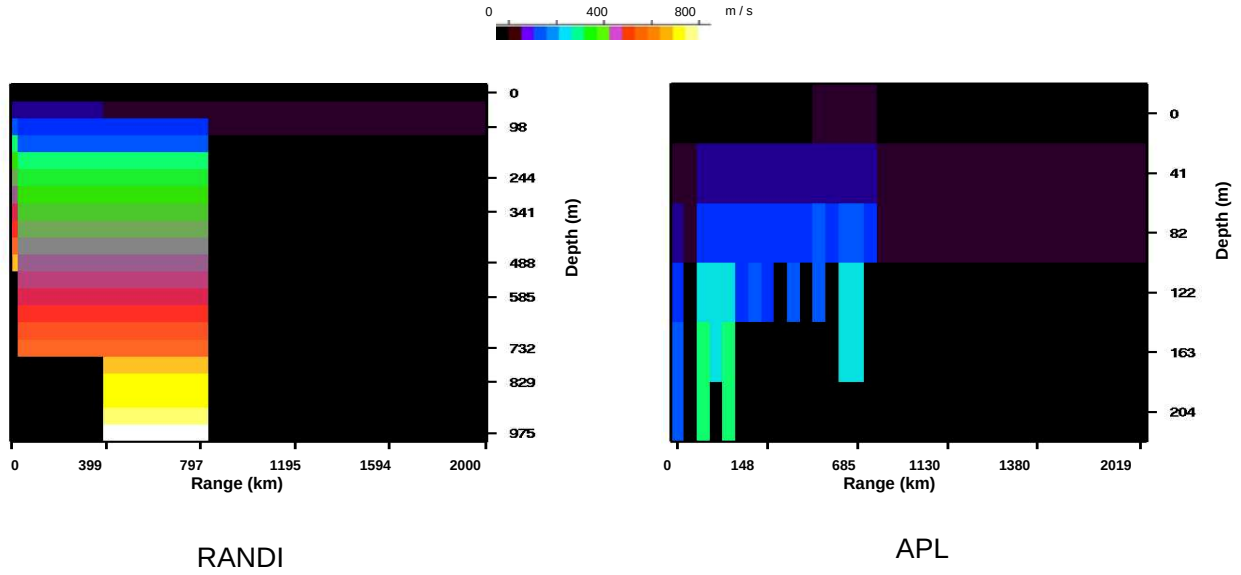

Fig. B2 — Sediment compressional speed fields for the deep-water track in the Gulf of Alaska: RANDI environment (left) and the APL environment (right)

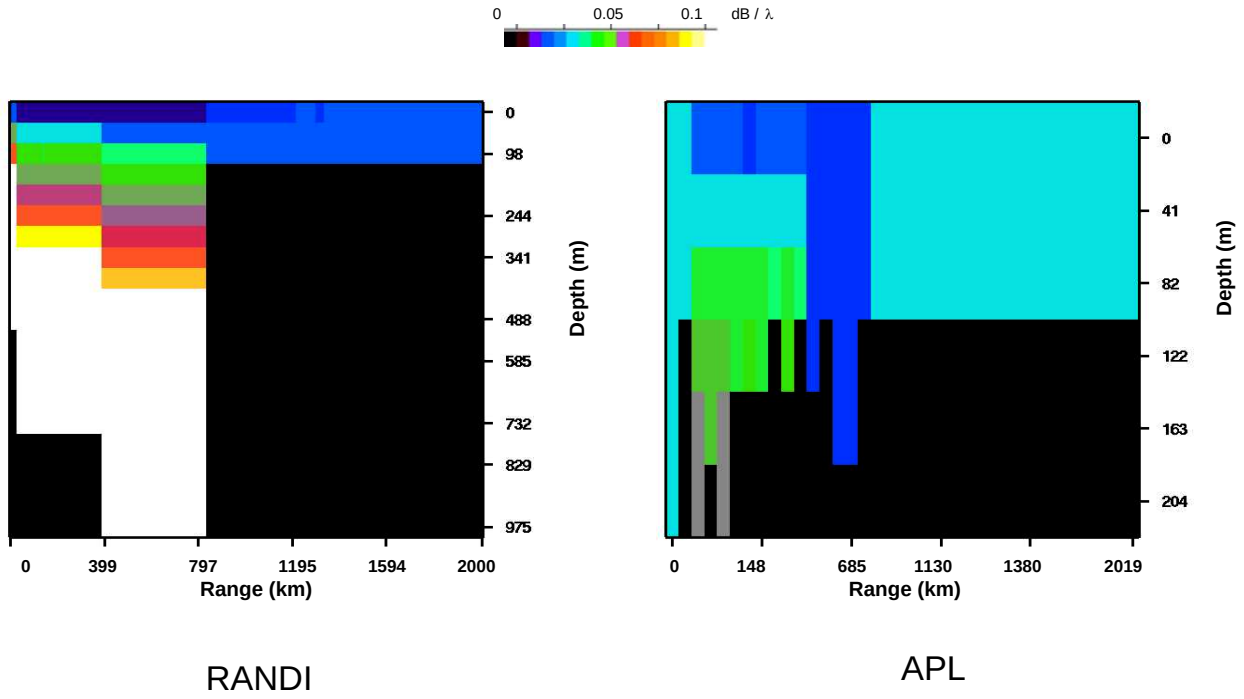

Fig. B3 — Sediment attenuation fields for the deep-water track in the Gulf of Alaska: RANDI environment (left) and the APL environment (right)

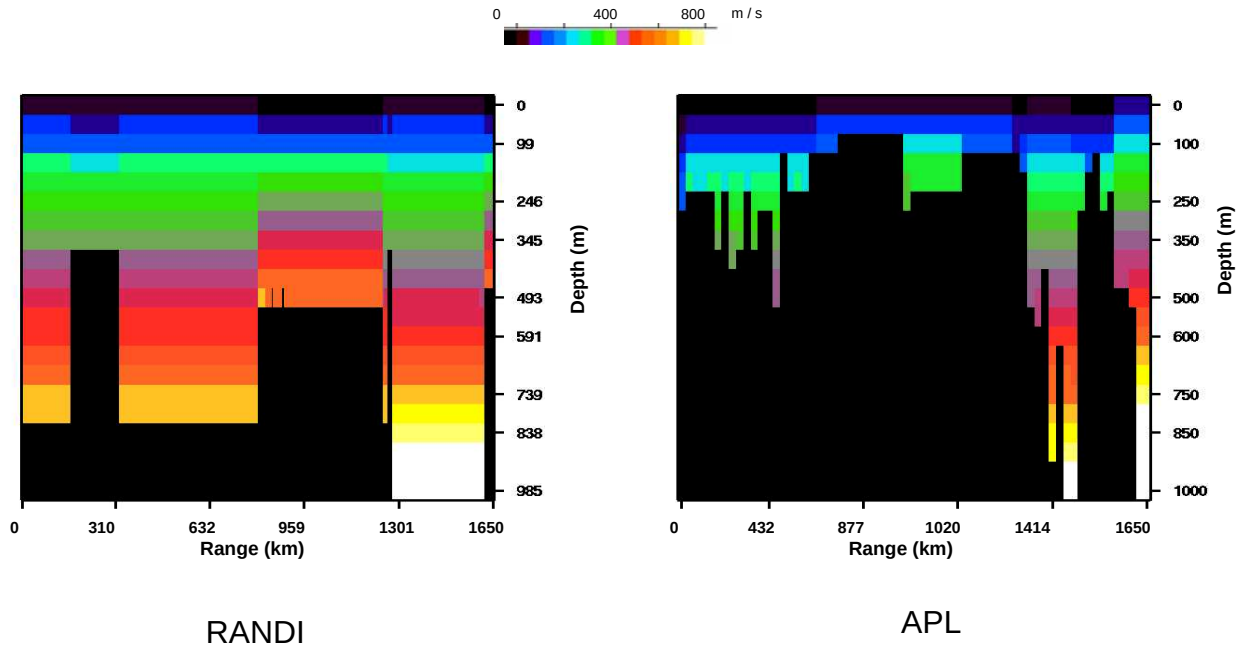

Fig. B4 — Sediment compressional speed fields for the shelf track in the Gulf of Alaska: RANDI environment (left) and the APL environment (right)

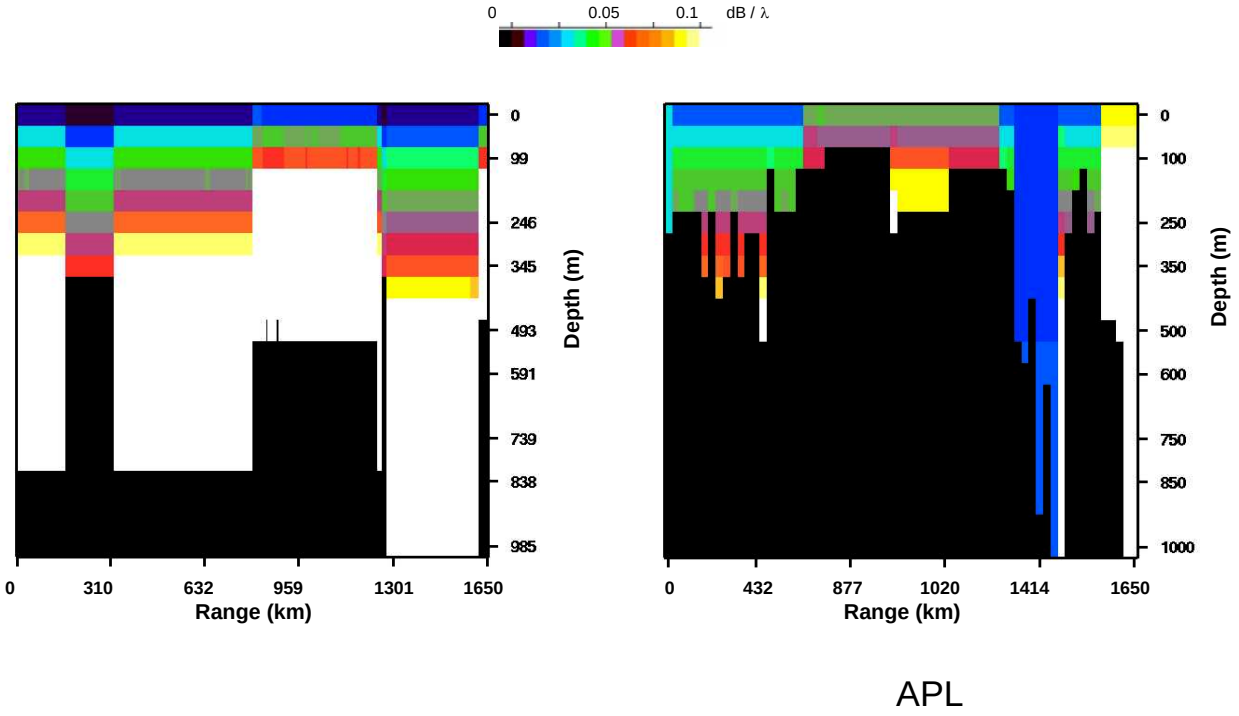

Fig. B5 — Sediment attenuation fields for the shelf track in the Gulf of Alaska: RANDI environment (left) and the APL environment (right)

Table B2 — RANDI and APL Environmental Parameters for Gulf of Alaska Site and 2 km Downrange on the Continental Slope Track

	RANDI		**APL**	
	site	0.5 km	site	6.4 km
Sound-speed ratio	0.9900	1.020	0.9760	0.997
Density ($g/cm^{3)}$)	2.18	3.06	1.41	3.57
Sediment Thickness (m)	459.4	760.9	203.4	187.1
Interface attenuation (10^{-2} dB/λ)	1.4994	0.269	2.218	1.519
Water depth (m)	3456	3456	3456	3954